Thermodynamics of Liquid Iron System Deoxidized with Aluminum

By

Kyoko Wasai

Department of Materials Science and Engineering,

Faculty of Engineering,

Kyushu Institute of Technology

Contents

List of Symbols

I. Chapter 2.

In this list, i and subscript i indicates monomer or associated compound (Fe_1, Al_1, O_1 and $Fe_pAl_qO_r$(a): p, q, r=0,1,2,3,----): j and subscript j indicates the component element (Fe, Al, O) in Fe-Al-O liquid alloy.

(a), (g), (l), (s): associated compound, gas, liquid and solid

a_i, a_j: activities of i and j with Raoultian standard state and molar fraction concentration unit.

$a^*_{Fe_pAl_qO_r}$: activity of associated oxide with Henrian standard state and molar fraction concentration unit.

a^*_O, $a^*_{O_1}$: activities of O and O_1 with Henrian standard state and at.% concentration unit.

$a^*_{Al,\%}$, $a^*_{O,\%}$: activities of O and Al with Henrian standard state and mass% concentration unit.

e_l^m: interaction coefficient (l, m indicate Al or O component)

f_j: activity coefficient of j with Henrian standard state and mass% concentration unit.

$\Delta G^\circ_{FeO}(a)$: the standard Gibbs free energy of formation.

$\Delta G^\circ_{[2.m]}$: the standard Gibbs free-energy change for the reaction of Eq. [2.m].

ΔG°_{sol}: the standard Gibbs free-energy change for dissolution of oxygen gas into liquid iron

K: deoxidation constant expressed by $= a_{Al}{}^2 a^*_O{}^3$.

K': deoxidation constant expressed by $= a^*_{Al,\%}{}^2 \cdot a^*_{O,\%}{}^3$.

$k_{Fe_pAl_qO_r}$: equilibrium constant of formation of associated compound.

$k_{[2.m]}$: equilibrium constant for the reaction of Eq. [2.m].

$k'_{[2.m]}$: quasi-equilibrium constant for the reaction of Eq. [2.m].

M_i, M_j: atomic weight of i and j.

M_T: molar weight of the liquid Fe-Al-O system expressed by Eq. [2.22].

μ_i°, μ_j°: standard chemical potentials of i and j the activity of which are expressed by a_i, a_j.

$\mu_{O_2}^\circ$: standard chemical potential of O_2(g).

$\mu_{Al_2O_3}^\circ$(s): standard chemical potential of solid α-alumina.

$\mu_{Fe_pAl_qO_r}^*$: standard chemical potential of associated oxide the activity of which is expressed by $a_{Fe_pAl_qO_r}^*$.

x_i: molar fraction of i.

X_j: molar fraction of component j.

II. Chapter 4

(1), (2), e: superscripts indicating the parent iron phases before nucleation, after nucleation, and in equilibrium with α-alumina, respectively.

a_{Al}, a_O, a_{Fe}: activities of aluminum, oxygen, and iron, respectively.

C_O^{cr}: critical point of nucleation.

Cp_{oxide}: molar heat capacity at constant pressure ($J \cdot K^{-1} \cdot mol^{-1}$).

ΔG: Gibbs free-energy change of one mole of the liquid Fe-O-Al system ($J \cdot mol^{-1}$).

ΔG_S: interfacial free energy of nuclei in one mole of the Fe-O-Al system (J/mol).

ΔG_A: Gibbs free-energy change of nuclei formation reaction.

($2\underline{Al}+3\underline{O} \rightarrow Al_2O_3$(s)) in one mole of the Fe-O-Al system ($J \cdot mol^{-1}$).

ΔG_B: Gibbs free-energy difference of parent liquid iron before and after nucleation ($J \cdot mol^{-1}$).

ΔG^*: critical Gibbs free energy of nucleation ($J \cdot mol^{-1}$).

ΔG_D: Gibbs free energy of activation for transporting a molecule across the interface ($J \cdot mol^{-1}$).

Δg_S: interfacial free energy of a nucleus ($J \cdot nucleus^{-1}$).

Δg_A: Gibbs free-energy change of an alumina nucleus formation ($J \cdot nucleus^{-1}$).

Δg_B: Gibbs free-energy difference of parent liquid iron before and after nucleation per nucleus ($J \cdot nucleus^{-1}$).

Γ: surface excess ($mol \cdot m^{-2}$).

h: Planck's constant.

H°_{oxide}: molar enthalpy of formation of oxide ($J \cdot mol^{-1}$).

$\Delta H^{\circ}_{oxide,at298K}$: molar enthalpy of formation of oxide at 298 K ($J \cdot mol^{-1}$).

I: rate of nucleation ($nucleus \cdot mol^{-1} \cdot s^{-1}$).

k: Boltzmann's constant.

m: $(4/3)\pi r^3 / V_A$.

M: molecular weight of alumina ($g \cdot mol^{-1}$).

n_0: total number of nuclei in one mole of the liquid Fe-O-Al system.

n^*: number of molecules on the surface of critical nucleus.

n: number of molecules of one mole of the parent phase, which, in the present study, is assumed to be one third of the oxygen atoms in the liquid iron.

N: Avogadro's number.

r: radius of nucleus (m).

r^*: critical radius of nucleus (m).

R: gas constant.

ρ: density of α-alumina (=3.987x10^{6}g·m^{-3}).

S: degree of supersaturation, $S = \left\{(a_{Al})^2(a_O)^3\right\} / \left\{(a_{Al}^{(e)})^2(a_O^{(e)})^3\right\}$.

S°: critical degree of supersaturation.

σ: interfacial free energy (N·m^{-1}).

$\sigma^*_{metals-oxide}$: interfacial free energy between various metals and oxides per mol as expressed by Eq. [4-4] (J·mol^{-1}).

$\sigma_{metals-oxide}$: interfacial free energy between various metals and oxides (N·m^{-1}).

σ_o: interfacial free energy of an alumina nucleus with radius r (N·m^{-1}).

T: temperature (K).

V_A: molar volume of alumina (m^3·mol^{-1}).

V_{oxide}: molar volume of oxide (m^3·mol^{-1}).

v: volume per molecule of the critical nucleus (m^3).

x_{Al}, x_O, x_{Fe}: initial molar fractions of aluminum, oxygen, and iron, respectively.

III. Chapter 6

(1), (2), e: superscripts indicating the parent iron phases before nucleation, after nucleation, and in equilibrium with α-alumina, respectively.

i: subscript indicating various aluminas (i: δ, γ, κ, and α-alumina).

$a_{a.s.}^{s.s.}$: activity of alumina-associated compound in a supersaturated state.

$a_{a.s.}^{e}$: activity of alumina-associated compound in equilibrium with α-alumina.

D: interfacial free-energy difference between α-alumina and other alumina. polymorphs at 1873K.

ΔG: Gibbs free-energy change of one mole of the liquid Fe-O-Al system (J·mol^{-1}).

ΔG_S: interfacial free energy of nuclei in one mole of the Fe-O-Al system (J/mol).

ΔG_A: Gibbs free-energy change of nuclei formation reaction ($2\underline{Al}+3\underline{O} \rightarrow Al_2O_3(s)$) in one mole of the Fe-O-Al system ($J \cdot mol^{-1}$).

ΔG_B: Gibbs free-energy difference of parent liquid iron before and after nucleation ($J \cdot mol^{-1}$).

Δg: is the Gibbs free-energy change for the formation of a nucleus ($J \cdot nucleus^{-1}$).

Δg^*: critical Gibbs free energy of nucleation per nucleus ($J \cdot nucleus^{-1}$).

Δg_D: Gibbs free energy of activation for transporting a molecule across the interface of a nucleus ($J \cdot nucleus^{-1}$).

Γ: surface excess ($mol \cdot m^{-2}$).

h: Planck's constant.

H_i°: molar enthalpy of formation of various alumina ($J \cdot mol^{-1}$).

$\Delta H_{i,\text{at } 298K}^\circ$: : molar enthalpy of formation of various alumina at 298 K ($J \cdot mol^{-1}$).

I: rate of nucleation ($nucleus \cdot mol^{-1} \cdot s^{-1}$).

m: $(4/3)\pi r^3 / V_i$.

n_i^*: number of molecules on the surface of i's critical nucleus (i: δ, γ, κ, and α-alumina).

ρ_i: density of various alumina.

ρ_l: density of liquid alumina.

$S_{a.s.}$: degree of supersaturation of alumina-associated compound, $S_{a.s.} = a_{a.s.}^{s.s.} / a_{a.s.}^{e}$

σ_{Fe-i}: interfacial free energy between various alumina and liquid iron.

σ_{Fe-i}^*: interfacial free energy between various alumina and liquid iron per mol as expressed by Eq. [6-13] ($J \cdot mol^{-1}$).

$\sigma_{Fe-\alpha}$: interfacial free energy between α-alumina and liquid iron.

$\mu^{s.s.}$: sum of the chemical potential of aluminum and oxygen in a supersaturated state, $\mu^{s.s.} = 2\mu_{Al}^{s.s.} + 3\mu_{O}^{s.s.}$.

$\mu_{Al}^{s.s.}$: chemical potential of aluminum in a super saturated state.

$\mu_{O}^{s.s.}$: chemical potential of oxygen in a super saturated state.

μ_{α}°: chemical potential of solid α-alumina.

$\mu_{a.s.}^{s.s.}$: chemical potential of alumina-associated compound in a super saturated state.

$\mu_{a.s.}^{e}$: chemical potential of alumina-associated compound in the equilibrium state.

μ_{i}°: chemical potential of various alumina.

μ_{ℓ}°: chemical potential of liquid alumina.

V_i: molar volume of various alumina ($m^3 \cdot mol^{-1}$).

v_i: volume per molecule of i's critical nucleus (i: δ, γ, κ, and α-alumina) (m^3).

IV. Chapter 7

$\mu_{quar.}^{\circ}$: standard chemical potential of quarts.

$\mu_{cri.}^{\circ}$: standard chemical potential of cristobalite.

$\mu_{liq.}^{\circ}$: standard chemical potential of liquid silica.

μ_{Si}°: standard chemical potential of silicon in liquid copper.

μ_{O}°: standard chemical potential of oxygen in liquid copper.

a_{Si}^{e}: activity of silicon in liquid copper in the equilibrium state.

a_{O}^{e}: activity of oxygen in liquid copper in the equilibrium state.

$\mu_{Si}^{s.s.}$: chemical potential of silicon in liquid copper in the supersaturated state.

$\mu_{O}^{s.s.}$: chemical potential of oxygen in liquid copper in the supersaturated state.

$\mu^{s.s.}$: sum of the chemical potential of silicon and oxygen in the supersaturated state(=$\mu_{Si}^{s.s.} + \mu_{O}^{s.s.}$).

$a_{\mathrm{Si}}^{s.s.}$: activity of silicon in liquid copper in the supersaturated state.

$a_{\mathrm{O}}^{s.s.}$: activity of oxygen in liquid copper in the supersaturated state.

M_i: atomiv weight of i.

Chapter 1 Preface

I Background

The steelmakers now face an important target, that of producing an ultra high clean steel by eliminating all inclusions. In contrast, several research studies have focused recently on utilizing inclusions positively.[1-5] This technology is referred to as 'oxide metallurgy' and the inclusions are intended to be the nucleation sites for the iron matrix in desirable form and structure. In order to accomplish these objectives, deep understanding of the mechanism of inclusion formation would be helpful, especially details concerning the first stage of nucleation, the influential factors in nucleation and the process of the growth of the nuclei. The knowledge offers an effective way of eliminating inclusions or controlling its morphology and distribution. Furthermore, the mechanism of nucleation is closely related to the thermodynamical properties of the steel. Thus, a deep knowledge of the thermodynamical properties will also aid the understanding of the mechanism.

Among the inclusion, alumina is the most notorious and the removal of the alumina cluster from the steel is a shared goal for all the steelmakers. Further, thermodynamical properties of Al-deoxidized steel are not fully clarified.

II Various Problems Associated with Alumina Inclusions and Thermodynamics for Al-deoxidized Iron

Various problems, associated with alumina inclusions and thermodynamics for Al-deoxidized iron, still await settlement and need to be clarified.

(1) There are various discrepancies in experimental reports for the Fe-Al-O liquid system in equilibrium with solid α-alumina (Al_2O_3(s)). For instance,

values of deoxidation constant K' or interaction parameters (e_{Al}^{O} , e_{O}^{Al} , etc.) measured by various investigators are different each other considerably.

(2) The position of the equilibrium point in the phase diagram (coexisting point), where the liquid Fe-Al-O system is in equilibrium with both of hercynite ($FeO \cdot Al_2O_3$(s)) and Al_2O_3(s), has not yet been established. The [%O] (mass%) of the point measured by various investigators are in the same order. However, the [%Al] (mass%) of the point measured by Novokhatskiy et al.[6] is two orders of magnitude larger than the aluminum activity and [%Al] calculated from the [%O], K' and interaction parameters (e_{Al}^{O} , e_{O}^{Al} , etc.).

(3) Deoxidation of liquid iron to the level such that the oxygen contained in the liquid iron is in equilibrium with the solid α-alumina is generally difficult. Thus, the oxygen content in the iron often exceeds the equilibrium level. Although reports concerning excess oxygen have been published, a persuasive explanation for the presence of excess oxygen beyond the equilibrium value has not yet been reported.

(4) In steel, there are two types of oxide inclusions, i.e., primary and secondary inclusions; the former forms after addition of the deoxidizer, whereas the latter forms during cooling or solidification. There are no methods which provide unequivocal, distinctive classification of the two (primary and secondary) types of inclusions.

(5) The presence of γ, δ, θ and κ-alumina inclusions has been reported in iron solidified immediately after aluminum-deoxidation. The γ, δ, θ and κ-alumina are unstable at steelmaking temperatures, whereas the α-alumina is a stable crystal phase. The reason why and how these aluminas form at steelmaking temperatures is unclear. Also, it is not known whether the unstable aluminas exist as secondary inclusions because the γ, δ, θ and κ-alumina phases have

been reported to be primary inclusions.

(6) The presence of amorphous silica inclusion in solidified iron has also been reported. It is well known that the amorphous silica is easily formed through the solidification of liquid silica. However, the melting point of silica is 1966 K and liquid silica would not be formed in iron in an ordinary manner at steelmaking temperatures. Why and how the amorphous silica is formed is the question.

III. Overview of the Present Study

The article from (1) to (6) mentioned in Section II are the essential problems for considering thermodynamics of Al-deoxidized iron and mechanism of alumina nucleation in the iron. The aim of the present study is to clarify the problems and provide a basis for developing a new way for eliminating or utilizing inclusions positively. In order to clarify the problems, three pieces of investigation by computer simulation (Chapter 2, 4 and 6) and three experiments (Chapter 3, 5 and 7) were performed. The results are summarized briefly as follows.

Chapter 2 Thermodynamic Analysis of Fe-Al-O Liquid Alloy Equilibrated with α-alumina by an Associated Solution Model.

Thermodynamic properties of Fe-Al-O dilute liquid alloy system in equilibrium with α-alumina were analyzed by an associated solution model assuming associated compounds (Al_2O_3(a), FeO(a), $FeO{\cdot}Al_2O_3$(a), Al_2O(a), Fe_3Al(a), FeAl(a) and $FeAl_3$(a)). The various discrepancies of the reported values by various investigators are explained reasonably on the basis of the model.

Chapter 3 Thermodynamic Study on Liquid Iron in Equilibrium with α-Alumina and Hercynite

The [%Al] and [%O] at 1873K of the coexisting point, at which the liquid Fe-Al-O system was in equilibrium with both of $FeO \cdot Al_2O_3$ and α-Al_2O_3, was investigated and measured. The [%Al] of this point is two orders of magnitude larger than the activity of aluminum but agrees fairly well with the [%Al] predicted by an associated solution model and that measured by Novokhatskiy et al. This discrepancy between the activity of aluminum and measured [%Al] is discussed.

Chapter 4 Thermodynamic Investigation on Nucleation and Supersaturation for the Aluminum-deoxidation Reaction in Liquid Iron

The nucleation process of alumina in Al-deoxidized liquid iron was investigated by computer simulation, in which the Gibbs free-energy change of the parent liquid iron, the dependence of interfacial free energy between liquid iron and α-alumina on oxygen content, and the dependence of the interfacial free energy on the curvature of a nucleus were considered. The simulation made clear the mechanism which posed the excess oxygen in aluminum-deoxidized liquid iron.

Chapter 5 Observation of Inclusion in Aluminum-deoxidized Iron

Aluminum-deoxidized iron alloy was solidified in 3 different cooling rate. Investigation on the morphology and sizes of alumina inclusions in the iron proved that differentiation between primary and secondary inclusion should be possible from the shape and size of the inclusion. Electronic diffraction analyses showed that many of the secondary alumina inclusions observed in the iron were secondary unstable (γ and δ-alumina) inclusions. The amorphous spherical silica inclusion was also observed in the iron.

Chapter 6 Thermodynamic Analysis on Metastable Alumina Formation in Aluminum-deoxidized Iron Based on Ostwald's Step Rule and Classical

Homogeneous Nucleation Theories

A mechanism for the formation of unstable alumina (δ, γ, and κ-alumina) in Al-deoxidized iron has been investigated on the basis of Ostwald's Step Rule and two homogeneous nucleation theories. Comparison of the chemical potential of various aluminas from the standpoint of the Ostwald's Step Rule showed that the unstable alumina could form from the liquid iron alloy supersaturated with oxygen. Moreover, the rule revealed a possibility of liquid alumina formation. The two homogeneous nucleation theories also proved the possibility of the formation of unstable and liquid alumina. A mechanism of the network-like or coral-like inclusion formation by taking into consideration of the liquid alumina formation was proposed.

Chapter 7 Mechanism of Formation of Amorphous Silica Inclusion in Silicon-Deoxidized Copper

In order to confirm the presence of secondary, amorphous silica inclusion in iron and copper, a silicon-deoxidation experiment of copper at 1423K was performed. Consequently, the secondary amorphous silica was observed in the copper, which should be strong evidence for the formation of liquid silica during cooling. Consideration based on Ostwald's Step Rule proved that liquid silica should be formed from the copper supersaturated with oxygen during cooling. The results would support the formation of secondary liquid alumina in the iron alloy.

Chapter 8 Summary

The summary of the present study was described in this chapter. The characteristic feature of this system made apparent from the present study was discussed briefly.

IV Conclusion

The details of the present experiments and computer simulations are described in the following Chapter 2 to 8 in this thesis. The investigation is unable to show a direct route to accomplishing to eliminate inclusions and control the morphology of inclusions, but provide the basic concept for searching the route to the objectives. Furthermore, the present investigation have developed by a light of new methods (associated solution model and modified classical nucleation theory). The methods were successful for describing the thermodynamics of this system and have clarified many problems and uncertainties in the system. I hope that the present results will be helpful for advanced progress of iron metallurgy and the new method would be useful for breaking through other metallurgical problems still await for settlement.

Reference

1. K.Oikawa, K.Ishida and T.Nishizawa: ISIJ Int., **37**(1997), 332.
2. H.Goto, K.Miyazawa and H.Honma: ISIJ Int., **36**(1996), 537.
3. H.Goto, K.Miyazawa and T.Kadoya: ISIJ Int., **35**(1995), 1477.
4. K.Oikawa, H.Ohtani, K.Ishida and T.Nishizawa: ISIJ Int., **35**(1995), 402.
5. J.H.Shim, Y.W.Cho, S.H.Chung, J.D.Shim and D.N.Lee: Acta. Mater., **47**(1999), 2751
6. I.A.Novokhatskiy and B.F.Belov: Russian Metallurgy, Nr.1(1966),12.

Chapter 2 Thermodynamic Analysis of Fe-Al-O Liquid Alloy Equilibrated with α-alumina by an Associated Solution Model.

I. Introduction

Aluminum is a most popular and widely-used deoxidizer of steel. Through a deoxidation reaction between aluminum and oxygen in the steel, solid α-alumina (Al_2O_3(s))* is formed . The liquid iron containing aluminum and oxygen in equilibrium with Al_2O_3(s) has been discussed in detail by the 19th Committee for Steelmaking belonging to Japan Society for the Promotion of Science (JSPS). The committee reported the recommended equilibrium values[1] for the liquid Fe-Al-O system on the basis of data measured by Rohde et al.[2] However, there are various discrepancies in experimental reports for the Fe-Al-O liquid system in equilibrium with Al_2O_3(s). The state in equilibrium with Al_2O_3(s) is hereafter referred to as the equilibrium state.

The discrepancies of the various experimental data of Fe-Al-O system in the equilibrium state are summarized as follows.

(1) The reported values of deoxidation constant, K' ($= a^*_{Al,\%}{}^2 \cdot a^*_{O,\%}{}^3$), at 1873K are divided in two groups: one is a group[3-7] in which K' ranges from 10^{-9} to 10^{-10}: in the other group[2,7-15], K' ranges from 10^{-13} to 10^{-14}.

The K' in the former group would have been obtained under the experimental

---

*Hereafter, α-alumina is reffered to as Al_2O_3(s).

condition of atmosphere that was somewhat contaminated with air, and thus, it is regarded as nonequilibrium value, which is discussed in Chapter 4. The latter K' values have been measured under the cautious atmosphere condition and the experiments have been performed maintaining constant high temperature for a long time in order to attain the equilibrium with Al_2O_3(s). However, The K' values in the latter group measured at 1873K and at higher temperatures show significant inconsistency.

(2) The interaction parameters (e_O^{Al} and e_{Al}^{O}) measured in the equilibrium state by various investigators are different each other significantly. As regards e_O^{Al}, the values from -1 to -12 at 1873K have been reported.

(3) The recommended values of e_O^{Al} and e_{Al}^{O} by JSPS[1] are nearly the upper limit (-1.17 and -1.98 respectively) in the reported values. Using the recommended values of K', e_O^{Al}, e_{Al}^{O}, e_O^{Al}, and e_O^{O} by JSPS, a calculated curve showing a relation between aluminum and oxygen contents ([%Al] and [%O])* in steel in the equilibrium state (Fig. 2.1), does not represent the trend of measured data. Such curve which shows a relation between [%Al] and [%O] in the equilibrium state is hereafter referred to as equilibrium curve or E.C. Another equilibrium curve shown in Fig. 2.1 calculated using the smallest interaction parameters measured by Gokcen[8] and assuming that e_O^{Al}, and e_O^{O} equal zero, also does not agree with the measured trend.

(4) Kim and McLean measured [%O] at an equilibrium point in the phase diagram, at which the liquid Fe-Al-O system was in equilibrium with both of

---

*In this Chapter 1, aluminum and oxygen contents in iron alloy in mass% unit are expressed as [%Al] and [%O], respectively.

hercynite ($FeO \cdot Al_2O_3(s)$) and $Al_2O_3(s)$.[18] This point is hereafter referred to as the coexisting point. Novokhatskiy and Belov also measured the [%Al] and [%O] of the point.[19] Both [%O] measured by Kim et al.[18], and by Novokhatskiy et al.[19] are in the same order. However, [%Al] measured by Novokhatskiy et al.[19] is two orders of magnitude larger than the aluminum activity or [%Al] calculated using the [%O] measured by Kim et al.[18], K' and interaction parameters (e_{Al}^{O}, e_{O}^{Al}, etc.).

(5) The Fe-Al-O alloy solidified after deoxidation contains aluminum insoluble in acid. The origin of the insoluble aluminum is now regarded as inclusion of $Al_2O_3(s)$ in the alloy which is the deoxidation product or the secondary inclusion formed during cooling . However, the origin of it is unclear.

(6) The data in Fig.2.1 at 1853K-2139K reported by various investigators, and the data in Fig. 2.2-(a) measured by d'Entremont et al.[15] at 2013K and 2183K, indicate various discrepancies. (i) The locations of the minimum of [%O] by various investigators around the region for $1>[\%Al]>0.1$ and the increasing tendencies of [%O] at the higher aluminum region from the minimums are different each other. (ii) The data by Schenck et al.[7] at 1873K in the region for $[\%Al]<0.003$ locate at higher oxygen position than the data by Janke and Fischer,[14] and Rohde et al.[2] Thus, the K' ($\approx[\%Al]^2[\%O]^3=3.3\times 10^{-12}$) value of the Schenck's data[7] is two orders of magnitude larger than the values by Janke and Fischer,[14] and Rohde et al.[2] (iii) The values of [%O] measured by d'Entremont et al.[15] are lower than those by other investigators.

The above article from (1) to (6) are significant for considering the thermodynamics of this system. In this chapter, the discrepancies are investigated by an associated solution model.

Alumina is known as one of the stable oxide. A large negative interaction parameter in steel (recommended as e_O^{Al}=-1.17 at 1873K by JSPS) expresses the strong interaction between aluminum and oxygen. The excess chemical potential of -420 J·mol^{-1} for oxygen in iron containing 0.01 mass%Al was calculated from the e_O^{Al}. The excess chemical potential value indicates the large stabilizing power of Fe-O alloy by addition of aluminum. However, the atom ratio of aluminum and oxygen to iron in the iron alloy (0.01 mass% Al and 0.001 mass% O) yields the presence of one oxygen and six aluminum atoms in 30000 iron atoms. Thus, the random distribution of oxygen and aluminum results in oxygen location apart from aluminum, which indicates that the oxygen and aluminum do not interact each other. Therefore, the oxygen and aluminum should locate in closer position at which the interaction is considerably effective. The present author consider that the two aluminum atoms and three oxygen atoms should be placed in adjacent position and move as a group as an alumina molecule. Thus, the associated solution model[20-22] would be applicable to the Fe-Al-O system.

II. Associated Solution Model for Fe-Al-O Alloy System

In the Fe-Al-O alloy system, the associated compounds, namely, Al_2O_3(a), FeO(a), FeO·Al_2O_3(a), Al_2O(a), Fe_3Al(a), FeAl(a) and $FeAl_3$(a) are assumed to be present. Iron and aluminum monomers (Fe_1 and Al_1) also exist in the liquid iron, but the content of oxygen monomer (O_1) is negligible, which have become clear by the consideration for the thermodynamics of metal-oxygen binary alloys.[22,23] The associated compounds are selected from the compounds found in the phase diagram of Fe-Al, Fe-O, and Fe-Al-O systems.

As regards the x_i, X_{Al} and X_O, namely, the molar fractions of i species (associated compounds and monomers), mole fraction of total aluminum and

that of total oxygen, respectively, following equations are written.

$$x_{Fe_1} + x_{Al_1} + \sum_i x_{Fe_pAl_qO_r} = 1, \quad [2.1]$$

$$X_{Al} = (x_{Al_1} + \sum_i q\, x_{Fe_pAl_qO_r})/(1 + \sum_i (p+q+r-1)\, x_{Fe_pAl_qO_r}), \quad [2.2]$$

$$X_O = (\sum_i r\, x_{Fe_pAl_qO_r})/(1 + \sum_i (p+q+r-1)\, x_{Fe_pAl_qO_r}), \quad [2.3]$$

where, $x_{Al_2O_3}$ has constant value, because Al_2O_3(a) is in equilibrium with solid alumina and thus, the system is saturated with Al_2O_3(a).

The behavior of activities of aluminum and iron in Fe-Al liquid system could be described by an ideal associated solution model.[20, 21] The following equations for iron and aluminum monomers and associated compounds (Fe_3Al(a), FeAl(a) and $FeAl_3$(a)) are written,

$$x_{Fe_1} = a_{Fe_1} = a_{Fe}, \quad x_{Al_1} = a_{Al_1} = a_{Al}, \quad [2.4]$$

$$x_{Fe_pAl_q} = a_{Fe_pAl_q} = k_{Fe_pAl_q} a_{Fe}{}^p a_{Al}{}^q, \quad [2.5]$$

$$-RT \ln k_{Fe_pAl_q} = \mu^\circ_{Fe_pAl_q} - p\mu^\circ_{Fe} - q\mu^\circ_{Al}. \quad [2.6]$$

Here, a_{Fe_1}, a_{Al_1}, a_{Fe} and a_{Al} are raoultian activities expressed by molar fraction concentration unit.

The contents of associated oxides, namely, Al_2O_3(a), FeO(a), $FeO{\cdot}Al_2O_3$(a), Al_2O(a), are very dilute. Therefore, Henrian activities were used for the associated oxides. The molar fractions and activities can be expressed as follows.

$$x_{Fe_pAl_qO_r} = a^*_{Fe_pAl_qO_r} = k_{Fe_pAl_qO_r} (a_{Fe})^p (a_{Al})^q (a^*_O)^r, \quad [2.7]$$

$$-RT \ln k_{Fe_pAl_qO_r} = \mu^*_{Fe_pAl_qO_r} - p\mu^\circ_{Fe} - q\mu^\circ_{Al} - r\mu^*_O, \quad [2.8]$$

where, a_{Al} is a raoultian (molar fraction unit) and superscript * indicates Henrian value. The standard state of Henrian activity of oxygen (a^*_O), is the dilute solution of Fe-O system . The concentration unit of the a^*_O is at % for

convenience's sake (a_{Fe} and a_{Al} are molar fraction unit). The a_O^* is not equal to the activity of oxygen monomer ($a_{O_1}^*$) which is also Henrian and expressed by atomic %. Since the chemical potentials of oxygen are equal to that of oxygen monomer,

$$a_{O_1}^* = 100x_{O_1} = a_O^* \cdot \exp((\mu_O^* - \mu_{O_1}^*)/RT). \quad [2.9]$$

The consideration with regard to oxygen activity in metal-oxygen systems proves that $a_{O_1}^*$ should be negligible small.[22,23] Thus,

$$a_O^* >> a_{O_1}^* \approx 0. \quad [2.10]$$

Substituting Eqs. [2.4], [2.5] and [2.7] into Eqs. [2.1], [2.2] and [2.3] yields,

$$a_{Fe} + a_{Al} + \sum_i k_{Fe_pAl_qO_r} a_{Fe}{}^p a_{Al}{}^q a_O^{*r} = 1, \quad [2.11]$$

$$X_{Al} = \frac{a_{Al} + \sum_i q k_{Fe_pAl_qO_r} a_{Fe}{}^p a_{Al}{}^q a_O^{*r}}{1 + \sum_i (p+q+r-1)\, k_{Fe_pAl_qO_r} a_{Fe}{}^p a_{Al}{}^q a_O^{*r}}, \quad [2.12]$$

$$X_O = \frac{\sum_i r k_{Fe_pAl_qO_r} a_{Fe}{}^p a_{Al}{}^q a_O^{*r}}{1 + \sum_i (p+q+r-1)\, k_{Fe_pAl_qO_r} a_{Fe}{}^p a_{Al}{}^q a_O^{*r}}. \quad [2.13]$$

Substituting arbitrary continuous values of a_{Al} into the known deoxidation constant K ($= a_{Al}{}^2 a_O^{*\,3}$), and Eqs. [2.11]. [2.12], [2.13] gives the continuous solutions for the unknown X_{Al}, X_O, a_{Fe}, and a_O^*, which could describe the E.C. and changes of activities accompanied to the E.C. The a_{Al} and a_O^* can be transformed into Henrian activities ($a_{Al,\%}^*$, $a_{O,\%}^*$) whose concentration units are mass %.

$$a_{Al,\%}^* = f_{Al}[\%Al] = 100(M_{Al}/M_{Fe}) \cdot (a_{Al}/r_{Al}^\circ) \quad [2.14]$$

$$a_{O,\%}^* = f_O[\%O] = (M_O/M_{Fe}) \cdot a_O^* \quad [2.15]$$

$$r_{Al}^{\circ} = 1/(k_{Fe_3Al} + k_{FeAl}) \quad [2.16]$$

In the calculation, the values of a_{Fe}, a_{Al}, and a_O^* was used, but the discussion and expression in the present study was performed by using the value of $a_{Al,\%}^*$ and $a_{O,\%}^*$ and mass% because the expression using mass % have been usual trend for this system. Next equations, which were transformed into mass% from Eqs [2.2] and [2.3], would be useful.

$$[\%O] = [\%O]_{FeO} + 4[\%O]_{FeO\cdot Al_2O_3} + 3[\%O]_{Al_2O_3} + [\%O]_{Al_2O}, \quad [2.17]$$

$$[\%Al] = [\%Al]_{Al} + [\%Al]_{Fe_3Al} + [\%Al]_{FeAl} + 3[\%Al]_{FeAl_3} + 2[\%Al]_{FeO\cdot Al_2O_3} + 2[\%Al]_{Al_2O_3} + 2[\%Al]_{Al_2O}, \quad [2.18]$$

where,

$$[\%O]_{Fe_pAl_qO_r} = (x_{Fe_pAl_qO_r}/B)\cdot(100M_O/M_T), \quad [2.19]$$

$$[\%Al]_{Fe_pAl_qO_r} = (x_{Fe_pAl_qO_r}/B)\cdot(100M_{Al}/M_T), \quad [2.20]$$

$$B = 1 + 3x_{Fe_3Al} + x_{FeAl} + 3x_{FeAl_3} + x_{FeO} + 6x_{FeO\cdot Al_2O_3} + 4x_{Al_2O_3} + 2x_{Al_2O}, \quad [2.21]$$

$$M_T = X_{Fe}M_{Fe} + X_{Al}M_{Al} + X_OM_O, \quad [2.22]$$

III. Calculated Results

A. Preliminary Calculation and Consideration

(1) Deoxidation Constant

Deoxidation constant, K, were calculated from standard Gibb's free-energy change for a next formation reaction of Al_2O_3(s).

$$2\,Al\,(l) + 3\,\underline{O}\,(at\%) = Al_2O_3\,(s) \quad [2.23]$$

$$\Delta G_{[2.23]}^{\circ} = \mu_{Al_2O_3}^{\circ}(s) = RT\ln K \quad [2.24]$$

$$K = a_{Al}^{\ 2}a_O^{*\ 3} \quad [2.25]$$

The standard Gibb's free energy of Al_2O_3 (s) formation reaction reported by

"JANAF Thermochemical Tables"[17], and the standard Gibb's free-energy change for dissolution of oxygen gas into liquid iron (ΔG°_{sol})[24] are as follows.

$2Al\ (l) + 3/2\ O_2\ (g) = Al_2O_3\ (s)$, [2.26]

$\Delta G^{\circ}_{[2.26]} = -1680500 + 323.40T$ J·mol^{-1}. [2.27]

$1/2O_2\ (g) = \underline{O}\ (at\%)$, [2.28]

$\Delta G^{\circ}_{sol} = \mu^{*}_{O} - 1/2\mu^{\circ}_{O_2} = -115580 - 14.410T$ J·mol^{-1}. [2.29]

Therefore, K can be written as,

$$\ln K = 44.096 - 160420/T.$$ [2.30]

Transforming the K into K' ($= a^{*}_{Al,\%}{}^{2} \cdot a^{*}_{O,\%}{}^{3}$) using Eqs. [2.14]-[2.16],

$$\log K' = 19.872 - 63251/T \quad (K' = 1.27\times10^{-14} \text{ at } 1873K).$$ [2.31]

(2) Outline of E.C. and Associated Compounds

The denominator of Eq. [2.3] (B in Eq. [2.21]) approximately equals 1, because of dilute concentration of associated compounds in low aluminum region. Thus, using Eqs. [2.7] and [2.14], following equation can be written.

$$X_O \approx x_{FeO} + 3x_{Al_2O_3} + 4x_{FeO\cdot Al_2O_3} + x_{Al_2O}$$
$$= k_{Fe0}a_{Fe}a^{*}_{O} + x_{Al_2O_3} + k_{Fe0\cdot Al_2O_3}Ka_{Fe}a^{*}_{O} + k_{Al_2O}K/a^{*}_{O}{}^{2}.$$ [2.32]

Therefore, x_{FeO} and $x_{FeO\cdot Al_2O_3}$ decrease with increase of aluminum content and conversely x_{Al_2O} increase because of the decrease of a_{Fe}, a^{*}_{O}. The decrease of $a^{*}_{O,\%}$ with increase of aluminum content is shown in Fig. 2.1. The decrease of oxygen content to the minimum ($[\%O]_{min}$) of E.C at 1873K in Fig. 2.1 reflects the decrease of x_{FeO} and $x_{FeO\cdot Al_2O_3}$. Subsequent increase of oxygen at the higher aluminum region from the minimum ($[\%Al]>0.8$), should be attributed to the increase of x_{Al_2O}. Therefore, the data in the low aluminum region for $[\%Al]<0.08$ at 1853-2139 K shown in Fig. 2.1 could be analyzed assuming

associated compounds excluding Al_2O(a).

On the other hand, from Eqs. [2.7], [2.15], and [2.19],

$$\log[\%O]_{Al_2O} = -2\log a^*_{O,\%} - \log(B \cdot M_T) + \log(100 k_{Al_2O} K M_O{}^3 / M_{Fe}{}^2). \quad [2.33]$$

The third term of the right side is a constant. At the region for [%Al]<0.5, the term, $B \cdot M_T$, nearly equals M_{Fe}. Even at the content that [%Al]=10, it equals about $1.3M_{Fe}$. Thus, the change of second term value could be ignored. Consequently, in the region that [%O] nearly equals to $[\%O]_{Al_2O}$, the increasing gradient of $[\%O]_{Al_2O}$ versus [%Al] is minus two times of the decreasing gradient of $\log a^*_{O,\%}$ versus [%Al]. Besides, the magnitude of k_{Al_2O} does not affect the increasing gradient of $[\%O]_{Al_2O}$, but affect the [%Al] of the minimum of E.C.

Regression analysis for the data of oxygen and aluminum contents of E.C. in Fig. 2.1 at 1853K-2139K yields a next equation.

$$\log X_O = 0.41434(\log X_{Al})^2 - 462.35(\log X_{Al})^2 / T + 0.61582(\log X_{Al}) + 368.31(\log X_{Al}) / T + 2.0360 - 10901 / T. \quad [2.34]$$

Relations between [%O] and [%Al] at various temperatures obtained by transforming the X_O and X_{Al} into mass% are shown by the solid lines in Fig. 2.1.

(3). Determination of $k_{Fe_pAl_q}$ and k_{FeO}

The equilibrium constants of formation of associated compounds in Fe-Al liquid system ($k_{Fe_pAl_q}$) were calculated using the activity values by Hultgren et al.[25] and mixing enthalpy values by Wooly and Elliott ($X_{Al} = 0.1 - 0.35$)[26] on the basis of ideal associated solution model.

$$-RT\ln k_{Fe_3Al} = -70955 + 20.879T, \quad [2.35]$$

$$-RT\ln k_{FeAl} = --61782 + 16.475T, \quad [2.36]$$

$$-RT\ln k_{FeAl_3} = -14630 + 43.279T. \quad [2.37]$$

As regards the chemical potential of FeO(a) (μ^*_{FeO}), a next equation can be written.[20]

$$\mu^*_{FeO} - 1/2\mu^\circ_{O_2} - \mu^\circ_{Fe} = \Delta G^\circ_{sol} + RT\ln 100. \quad [2.38]$$

From Eq. [2.29] and [2.38], the standard Gibb's free energy of formation ($\Delta G^\circ_{FeO}(a)$) can be derived as,

$$\Delta G^\circ_{FeO}(a) = \mu^*_{FeO} - \mu^*_O - \mu^\circ_{Fe} = -RT\ln 0.01 = -RT\ln k_{FeO}, \quad [2.39]$$

where, k_{FeO}, the equilibrium constant of formation of FeO(a), is 0.01 and does not depend on temperature.

(4) Approximate Activities

The a^*_O for the arbitrary a_{Al} can be calculated from *K*. Using the a^*_O and a_{Al}, and assuming the presence of Fe_3Al(a), FeAl(a) and FeO(a), approximate values of X_{Al} and a_{Fe} can be derived from the next equations.

$$a_{Fe} + a_{Al} + k_{Fe_3Al}a_{Fe}{}^3a_{Al} + k_{FeAl}a_{Fe}a_{Al} + k_{FeO}a_{Fe}a^*_O \approx 1, \quad [2.40]$$

$$X_{Al} \approx \frac{a_{Al} + k_{Fe_3Al}a_{Fe}{}^3a_{Al} + k_{FeAl}a_{Fe}a_{Al}}{1 + 3k_{Fe_3Al}a_{Fe}{}^3a_{Al} + k_{FeAl}a_{Fe}a_{Al} + k_{FeO}a_{Fe}a^*_O}. \quad [2.41]$$

The X_O corresponding to the X_{Al} can be derived from Eq. [2.34]. Therefore, a group of approximate values of X_{Al}, X_O, a_{Fe} and a^*_O for an arbitrary value of a_{Al} could be obtained.

B. Determination of $k_{FeO\cdot Al_2O_3}$ and $k_{Al_2O_3}$

The $k_{FeO\cdot Al_2O_3}$ and $x_{Al_2O_3}$ could be determined by regression analysis of the next equation, using over ten groups of estimated X_{Al}, X_O, a_{Fe}, a^*_O and a_{Al}.

$$X_O(1+3k_{Fe_3Al}a_{Fe}{}^3a_{Al}+k_{FeAl}a_{Fe}a_{Al}+3k_{FeAl_3}a_{Fe}a_{Al}{}^3)+(X_O-1)k_{FeO}a_{Fe}a_O^*$$
$$=(3-4X_O)x_{Al_2O_3}+(4-6X_O)k_{FeO\cdot Al_2O_3}a_{Fe}a_{Al}{}^2a_O^{*\,4}. \qquad [2.42]$$

The analysis was performed for the range, 0.005<[%Al]<0.08, where the content of Al_2O(a) can be neglected. The results for each temperature can be summarized as follows.

$$-RT\ln x_{Al_2O_3}=RT\ln k_{Al_2O_3}-RT\ln K$$
$$=\mu^*_{Al_2O_3}(a)-\mu^\circ_{Al_2O_3}(s)=199710-4.000T,\ \text{J·mol}^{-1}. \qquad [2.43]$$

$$RT\ln k_{Al_2O_3}=-1134000+362.62T,\ \text{J·mol}^{-1}. \qquad [2.44]$$

$$RT\ln k_{FeO\cdot Al_2O_3}=-1255500+393.87T,\ \text{J·mol}^{-1}. \qquad [2.45]$$

C. Determination of k_{Al_2O}

As regards the data by Rohde et al.[2], Janke et al.[14], Swicher et al.[10] and d'Entremont et al.[15] in the range for [%Al]>0.8, the [%0] increases from $[\%O]_{min}$. The increase is due to the increase of Al_2O(a). Therefore, k_{Al_2O} should be determined from analysis of the data in this range.

(1) Method of Oxygen Analysis by d'Entremont et al.

D'Entremont et al.[15] considered that all the oxygen in liquid Fe-Al-O system should be transformed into alumina during cooling and solidification. They obtained the oxygen content from residue of filtration for the acid solution of solidified sample. The residue which was insoluble in acid was heated (1373K) and cooled twice and was weighed (w_1 g) and melted with potassium disulfate, by which the residue became soluble in acid; acid and distilled water were added and the solution was divided into two equal solutions and the two solutions were

analyzed respectively by the following two methods. (1) Colorimetric Analysis; aluminum in the solution was analyzed by colorimetric analysis and the aluminum quantity was converted to [%O] from the stoichiometry of Al_2O_3 ($[\%O]_{colori}$). (2) Gravimetric analysis; iron in the solution was analyzed; on the basis of the consideration that the iron had been included in the residue in the form Fe_2O_3 (w_2 g) and thus, ($w_1 - w_2$) g corresponded to the weight of Al_2O_3, [%O] was determined by the weight ($[\%O]_{gravi}$). As shown in Fig. 2.2-(a), the $[\%O]_{colori}$ and $[\%O]_{gravi}$ do not agree with each other. Further, the $[\%O]_{colori}$ and $[\%O]_{gravi}$ are smaller than the [%O] of E.C. in the region for [%Al]<0.8 (solid lines in Fig. 2.2-(a)) that was calculated assuming $x_{Al_2O} = 0$ and using Eqs.[2.43] and [2.45].

(2) Oxides Insoluble in Acid and Associated Compounds

The solid compounds Fe_3Al (s), FeAl (s), $FeAl_3$ (s) and FeO (s) are soluble in acid, but Al_2O_3 (s) and $FeO{\cdot}Al_2O_3$ (s) are insoluble in acid[27]. Solidified associated oxides, Al_2O_3 (s), $FeO{\cdot}Al_2O_3$ (s) and FeO (s) should be present in the solidified Fe-Al-O alloy which is quenched rapidly. The solidified associated oxide Al_2O(s) would be present also in the solidified iron alloy sample[28], because the [%O] by d'Entremont et al.[15] in the range for [%Al]>0.8 increases. This indicates further that the Al_2O(s) is insoluble in acid. The residue of the filtration is possibly composed of the solidified associated oxides insoluble in acid, namely, Al_2O_3(s), $FeO{\cdot}Al_2O_3$(s) and Al_2O(s). Consequently, the values of [%O] by d'Entremont et al.[15] would be lower than the real value by oxygen quantity due to FeO (s), because the iron quantity dissolved from the FeO (s) in the acid solution was not counted in their analysis. Also, the [%O] would accompany the error due to the disregard of $FeO{\cdot}Al_2O_3$ (s) and Al_2O (s).

(3) Revision of $[\%O]_{colori}$ and $[\%O]_{gravi}$.

By twice heating at 1373K in the analyzing process by d'Entremont et al.[15], Al_2O(s) should be oxidized into Al_2O_3(s), thus,

$$[\%O]_{colori} = 3[\%O]_{Al_2O_3} + 3[\%O]_{FeO\cdot Al_2O_3} + 3[\%O]_{Al_2O}. \quad [2.46]$$

The iron in the residue that d'Entremont et al. considered to come from Fe_2O_3[15] would be the iron from $FeO\cdot Al_2O_3$(s), therefore,

$$[\%O]_{gravi} = 3[\%O]_{Al_2O_3} + 3[\%O]_{Al_2O} + 3[\%O]_{FeO\cdot Al_2O_3}\cdot(M_{FeO\cdot Al_2O_3} - \frac{1}{2}M_{Fe_2O_3})/M_{Al_2O_3}. \quad [2.47]$$

From Eqs.[2.17], [2.46], and [2.47],

$$[\%O]-[\%O]_{colori} = [\%O]_{FeO} + [\%O]_{FeO\cdot Al_2O_3} + 2[\%O]_{Al_2O}, \quad [2.48]$$

$$[\%O]-[\%O]_{gravi} = [\%O]_{FeO} - 2[\%O]_{Al_2O} + [\%O]_{FeO\cdot Al_2O_3}\cdot\{4 - 3(M_{FeO\cdot Al_2O_3} - \frac{1}{2}M_{Fe_2O_3})/M_{Al_2O_3}\}. \quad [2.49]$$

Therefore, through adding the value of Eq.[2.48] to $[\%O]_{colori}$ and that of [2.49] to $[\%O]_{gravi}$, the real values of [%O] can be evaluated. For the evaluation, the values of $[\%O]_{FeO}$, $[\%O]_{Al_2O_3}$, and $[\%O]_{FeO\cdot Al_2O_3}$ are necessary.

The content of Al_2O_3(a), $FeO\cdot Al_2O_3$(a) and Al_2O(a) do not affect the value of [%Al] in the region of the data by d'Entremont et al. Therefore, with regard to the data by d'Entremont et al, good approximate activities of iron, aluminum and oxygen could be obtained by solving Eqs. [2.11], [2.12] and $K = a_{Al}{}^2 a_O^{*\,3}$ assuming associated compounds except Al_2O(a). Thus, $[\%O]_{FeO}$, $[\%O]_{Al_2O_3}$, and $[\%O]_{FeO\cdot Al_2O_3}$ in the Eqs. [2.47]-[2.51] could be obtained. In the evaluation of [%O], $[\%O]_{Al_2O}$ was regarded as zero in the

region for [%Al]<0.8, but in the region for [%Al]>0.8, $[\%O]_{Al_2O}$ was derived from the following equations.

For the colorimetric data,

$$[\%O]_{Al_2O} = \frac{1}{3}[\%O]_{colori} - [\%O]_{Al_2O_3} - [\%O]_{FeO\cdot Al_2O_3}, \qquad [2.50]$$

for the gravimetric data,

$$[\%O]_{Al_2O} = \frac{1}{3}[\%O]_{gravi} - [\%O]_{Al_2O_3} - [\%O]_{FeO\cdot Al_2O_3}(M_{FeO\cdot Al_2O_3} - \frac{1}{2}M_{Fe_2O_3})/M_{Al_2O_3}. \qquad [2.51]$$

By adding the value of Eq. [2.48] to $[\%O]_{colori}$ and the value of Eq. [2.49] to $[\%O]_{gravi}$, obtained revised values of [%O] are shown in Fig. 2.2-(b). The revised data in Fig. 2.2-(b) agrees well with E.C. calculated using all the k_i including k_{Al_2O} which is described in the next Section. The revised data for the colorimetric and gravimetrict analyses are consistent with each other.

(4) Calculation of k_{Al_2O}

The [%O] of the data by Rode et al.[2], Janke et al.[14], and Swischer et al.[10], and the revised [%O] of d'Entremont et al.[15] increase from $[\%O]_{min}$ in the region for [%Al]>0.8. The [%Al] measured by Fruehan[12] at the oxygen minimum of E.C. ($[\%O]_{min}$) is about 0.2 mass %Al. It is lower than any other values. As shown previously, the increasing gradient of $[\%O]_{Al_2O}$ should be minus two times of gradient of $\log a^*_{O,\%}$ at the region for [%Al]>0.8. With this respect, the increasing gradient of the data by Rohde et al.[2] is larger. Therefore, the data by Janke et al.[14] and Swischer et al.[10], and the revised data of d'Entremont et al.[15] for [%Al]>0.8, excluding the data by Rohde et al.[2] and Freuehan[12], were used for the derivation of k_{Al_2O}. The Least Square Method

of a next equation led to the $\ln k_{Al_2O}$ as a form of $a+b/T$.

$$\ln k_{Al_2O} = a + b/T = \ln Y - \ln\{a_{Al}{}^2 a_O^* (1-2X_O)\} \quad [2.52]$$

$$Y = X_O + (6X_O - 4)k_{FeO\cdot Al_2O_3} a_{Fe} a_{Al}{}^2 a_O^{*4} + (4X_O - 3)x_{Al_2O_3} + (X_O - 1)x_{FeO}$$

$$+X_O(3k_{Fe_3Al} a_{Fe}{}^3 a_{Al} + k_{FeAl} a_{Fe} a_{Al} + k_{FeAl_3} a_{Fe} a_{Al}{}^3) \quad [2.53]$$

$$\ln k_{Al_2O} = -4.7928 + 26770/T \quad [2.54]$$

(5) Calculation of Activities and E.C

From Eqs. [2.11]-[2.13], using all the equilibrium constants of associated compounds, the calculated E.C. at 1873K-2073K are shown in Fig. 2.2-(a) and Fig. 2.3. As clear in the figures, the E.C. well agreed with the data in the wide region of 0.0003<[%Al]<12. The distinctive features in E.C., which are concave curves to the lower aluminum side and a minimum in [%Al] ($[\%Al]_{min}$) are observed. At 1873-2183K, $[\%Al]_{min}$ located in the region for [%O]=0.007-0.045, and $[\%O]_{min}$ located in the region for [%Al]=0.5-0.8. Besides, the revised data of [%O] by d'Entremont et al.[15] at 2013K in high aluminum region increases from $[\%O]_{min}$ but inversely decreases from the data exceeding about 2 mass%Al. The data at 2183K seems not to increase. This is due to the increase of vapour pressure of Al_2O(a) with increase of temperature. However, the positions of $[\%O]_{min}$ are well agreed with E.C. calculated as shown in Fig. 2.2-(b) and 2.3. When reliable data are obtained in the region for [%Al]>0.8, re-investigation should be necessary.

IV Discussion

A. Relation between Feature of E.C. and Associated Compounds

The change of $r[\%O]_{Fe_pAl_qO_r}$ versus [%Al] and the change of $q[\%Al]_{Fe_pAl_qO_r}$

versus [%O] were plotted in Figs. 2.4 and 2.5, respectively. As shown in Eq. [2.17] and Fig. 2.4, [%O] decreases with $[\%O]_{FeO}$ in the low aluminum region, reaches $[\%O]_{min}$ which is approximately equal to $3[\%O]_{Al_2O_3}$, subsequently increases accompanied with the increase of $[\%O]_{Al_2O}$. Figure 2.4 shows that the $[\%O]_{FeO\cdot Al_2O_3}$ has influence to E.C. only in the low aluminum region ([%Al]=0.001-0.002). Figure 2.4 also proves that the $[\%O]_{FeO}$ is nearly equal to $a^*_{O,\%}$ but $a^*_{O,\%}$ is not equal to [%O]. As shown in Fig.2. 5, in the region for 0.01< [%Al] <1, [%Al] is nearly equal to $[\%Al]_{Al}+[\%Al]_{Fe_3Al}+[\%Al]_{FeAl}$, but in the low aluminum region, the [%Al] is influenced by $[\%Al]_{FeO\cdot Al_2O_3}$ to reach $[\%Al]_{min}$ and increase with further increase of [%O]. From Eqs. [2.14], [2.16] and [2.20], when $a_{Fe}\cong 1$, $M_T \approx M_{Fe}$, and $B\approx 1$, a next equation can be written.

$$a^*_{Al,\%} \approx [\%Al]_{Al}+[\%Al]_{Fe_3Al}+[\%Al]_{FeAl}. \qquad [2.55]$$

In the region of 0.01<[%Al]<1, the left side term of $a^*_{Al,\%}$ is nearly equal to [%Al].

Similar relations at higher temperatures than 1873K between the feature of E.C. and contents of the associated compounds are observed.

B. Aluminum Insoluble in Acid

When sample is quenched rapidly and, thus, change of contents of associated compounds during cooling is negligible, aluminum insoluble in acid in the sample (*Insol Al*) is written as follows,

$$Insol\ Al = 2[\%Al]_{FeO\cdot Al_2O_3}+2[\%Al]_{Al_2O_3}+2[\%Al]_{Al_2O}. \qquad [2.56]$$

Therefore, the aluminum contents in the colorimetric analysis by d'Entremont et al.[15] corresponds to the *Insol Al*. The value of *Insol Al* by d'Entremont et

al.[15] can be derived from $[\%O]_{colori}$ using a next equation.

$$Insol\ Al = (2/3)[\%O]_{colori} M_{Al} / M_O. \qquad [2.57]$$

The *Insol Al* in the region of [%Al]<0.8 derived from Eq. [2.57] and *Insol Al* calculated from Eq. [2.56] based on associated solution model using all the k_i values obtained in the present study are compared in Fig. 2.6. Both values of *Insol Al* coincide each other.

Gokcen et al.[8] reported that the values of *Insol Al* measured in iron alloy of various contents of aluminum and oxygen were almost constant at each temperature (1968K, 2033K, and 2139K) and the average values at 1968K, 2033K, and 2139K were 25, 30, 55 mass ppm, respectively. Fujisawa et al.[29] reported that *Insol Al* observed in Fe-Al-Si alloy at 1873K, 1843K and 1823K, which were equilibrated with mulite ($3Al_2O_3 \cdot SiO_2$) saturated with Al_2O_3(s), were all 3 mass ppm.

In the region of [%Al]<0.8, *Insol Al* is gradually increases with decrease of [%Al] because of increase of $[\%Al]_{FeO \cdot Al_2O_3}$. However, $2[\%Al]_{Al_2O_3}$ is dominant in *Insol Al* and $[\%Al]_{FeO \cdot Al_2O_3}$ is lower than $2[\%Al]_{Al_2O_3}$ Only in very low aluminum region, $[\%Al]_{FeO \cdot Al_2O_3}$ exceeds $2[\%Al]_{Al_2O_3}$. The data of Gokcen et al.[8] and Fujisawa et al.[29] are in the region that $2[\%Al]_{Al_2O_3}$ is dominant in *Insol Al*. Therefore, the data of Gokcen et al. are almost constant at each temperature. The $[\%Al]_{FeO \cdot Al_2O_3}$ and $2[\%Al]_{Al_2O_3}$ become larger at higher temperature, thus, *Insol Al* increases with increase of temperature. The *Insol Al* values by d'Entremont[15] and Gokcen et al.[8] support this. However, the change of $2[\%Al]_{Al_2O_3}$ by the change of temperature becomes smaller in the lower temperatures. The measured temperatures of Fujisawa et al.[29] are lower

than 1873K, thus, the *Insol Al* shows almost constant value.

The values of *Insol Al* measured by Gokcen et al.[8] and Fujisawa et al.[29] are agreed with *Insol Al* derived from Eq. [2.56]. The result mentioned in this section strongly support that *Insol Al* is originated in associated compounds which are insoluble in acid.

C. The Coexisting Point of Liquid Iron, Alumina and Hercynite

The coexisting point should locate on a end of E.C. at low aluminum region. The coexisting point at the end of the E.C. calculated in the present study was determined as the [%O] for the coexisting point agreed with the [%O] of the point measured by Kim et al.[18] The coexisting points determined are shown in Fig. 2.3 (1873,1973K) and Fig. 2.7 (1823,1873,1923,1973K), whose locations are consistent with those measured by Novokhatskiy et al.[19] Also, the $a^*_{Al,\%}$ (6.5×10^{-6} at 1873K) at the coexisting point well agrees with the activity calculated from the [%O] by Kim et al.[18] Therefore, disagreement between the data by Kim et al.[18] and Novokhatskiy et al.[19], which is mentioned in Section I (Introduction), poses from the concave curve of E.C. in low aluminum region, namely, activity, $a^*_{Al,\%}$, is not equal to [%Al] and can not be described in the region by the reported interaction coefficients.

The standard Gibbs free energy of formation of $FeO\cdot Al_2O_3(s)$ derived in the present study from the activities of iron and oxygen at the coexisting points is shown in the following equation, which is well agreed with that reported by Kim et al.[18]

$$Fe(l) + \underline{O}(mass\%) + Al_2O_3(s) = FeO\cdot Al_2O_3(s) \qquad [2.58]$$

$$\Delta G^\circ_{[2-58]} = -176910 + 71.935T \quad J\cdot mol^{-1} \qquad [2.59]$$

D. Concave Curve and $[\%O]_{colori}$ in Low Aluminum Region

It is shown by the concave curve of E.C. in Figs. 2.4 and 2.5 that the data of Schenck et al.[7] and Novokhatskiy et al.[19] are consistent with the data by Rohde et al.[2], Janke et al.[14] and Kim et al.[18] All the data are explained by the E.C. calculated based on associated solution model. In the Cu-Ni-O[30] and Cu-Co-O[31] systems, similar concave curves of E.C. are observed experimentally.

E. Interaction Parameters

From Fig. 2.4, it is clear that $a^*_{O,\%}$ deviates negatively and $f_O << 1$. Also, from Fig. 2.5, aluminum activity, $a^*_{Al,\%}$, in low aluminum region deviates negatively.

The interaction parameters e_O^{Al}, e_{Al}^{O}, e_{Al}^{Al}, and e_O^{O} have been defined as follows by JSPS.[1]

$$e_m^n = \lim_{[\%Fe]\to 100} (\partial \log f_m / \partial [\%n]) \quad (m, n = O, Al) \qquad [2.60]$$

(1) e_O^{Al}

Gokcen et al., McLean et al., and Kobayashi et al. determined e_O^{Al} by measuring oxygen and aluminum contents in the Fe-Al-O liquids in equilibrium with Al_2O_3(s) under the various H_2-H_2O gas atmosphere. The equilibrium constant ($k_{[2.61]}$) and quasi-equilibrium constant ($k'_{[2.61]}$) of a following reaction in the measuring system, are expressed as follows.

$$H_2(g) + \underline{O}\ (\text{mass}\%) = H_2O(g), \qquad [2.61]$$

$$\Delta G^\circ_{[2.61]} = -134800 + 61.77T, \quad \text{J·mol}^{-1} \qquad [2.62]$$

$$\log k'_{[2.61]} = \log\{P_{H_2O} / (P_{H_2} \cdot [\%O]\} = \log f_O + \log k_{[2.61]}. \qquad [2.63]$$

In Fig. 2.8, values of $\log k'_{[2.61]}$ versus [%Al] derived from the data by various investigators are shown. The $\log k'_{[2.61]}$ should approach $\log k_{[2.61]}$ as [%Al] approaches zero because the Fe-Al-O system approaches Fe-O binary system and thus, f_O becomes nearly equal to 1. The $\log k_{[2.61]}$ at 2073K and 1973K calculated from Eq. [2.62] are shown on the vertical axis in Fig. 2.8. It is clear that the values of $\log k'_{[2.61]}$ by various investigators approach the calculated value of $\log k_{[2.61]}$ at low aluminum region. In Fig. 2.8, relations between [%Al] and $\log k'_{[2.61]}$ at 2073K and 1973K, which are calculated using $\log k_{[2.61]}$ and $\log f_O$ on E.C. based on associated solution model, are shown by two solid curves. Each curve is consistent with the data, but shows concave curve and thus, it does not meet the vertical axis. The data also have tendency to incline steeply at low aluminum region. However, Gokcen et al., McLean et al., and Kobayashi et al. derived e_O^{Al} from Eq. [2.65] assuming that the relations between $\log k'_{[2.61]}$ and [%Al] in Fig. 2.8 are straight lines and neglecting e_O^O and [%O] in Eq. [2.64] because of the small values of them .

$$\log f_O = e_O^O[\%O] + e_O^{Al}[\%Al] \approx e_O^{Al}[\%Al], \qquad [2.64]$$

$$e_O^{Al} = d\log f_O / d[\%Al] = d\log k'_{[1\text{-}61]} / d[\%Al]. \qquad [2.65]$$

The each e_O^{Al} derived by different investigators are different according to the range of [%Al] for the data used in the calculation. Rohde et al. and Janke et al also determined e_O^{Al} in similar ways.

(2) e_{Al}^O

$$Al_2O_3(s) + 3H_2(g) = 2\underline{Al}(mass\%) + 3H_2O(g), \qquad [2.66]$$

$$\log k'_{[2.66]} = \log k_{[2.66]} - 2\log f_{Al}. \qquad [2.67]$$

Equation [2.67] can be written by the equilibrium constant ($\log k_{[2.66]}$) and quasi-equilibrium constant ($\log k'_{[2.66]}$) for the reaction of Eq. [2.66]. The values of $\log k_{[2.66]}$ at 2073K and 1973K are shown on vertical axis in Fig. 2.9, which can be calculated from the standard Gibbs free energy of formation of Al_2O_3(s) and H_2O(g), and Eq. [2.14]. The $\log k'_{[2.66]}$ derived from the data by Gokcen et al., McLean et al., and Kobayashi et al. are shown in Fig. 2.9. The $\log k'_{[2.66]}$ calculated using the $\log k_{[2.66]}$ and f_{Al} on E.C. based on associated solution model are also shown in Fig. 2.9 in solid lines. The solid lines are well agreed with the $\log k'_{[2.66]}$ derived from the measured data, especially the $\log k'_{[2.66]}$ from the data by Kobayashi et al. Kobayashi et al. ignored e_{Al}^{Al} and [%Al] and calculated e_{Al}^{O} from Eq. [2.69] assuming the linear relation between $\log k'_{[2.66]}$ and [%O].

$$\log f_{Al} = e_{Al}^{O}[\%O] + e_{Al}^{Al}[\%Al] \approx e_{Al}^{O}[\%O], \qquad [2.68]$$

$$e_{Al}^{O} = d\log f_{Al} / d[\%O] = d\log k'_{[2.66]} / d[\%O]. \qquad [2.69]$$

Although the relation between $\log k'_{[2.66]}$ and [%O] in Fig. 2.9 seems roughly linear, the values of $d\log k'_{[2.66]} / d[\%O]$ derived at any points on each solid line are different largely ; at 1973K, the $d\log k'_{[2.66]} / d[\%O]$ changes from -18 to -59 at the range of 0.002-0.008 mass%$\underline{O}$. Further, the intercepts calculated by Kobayashi et al. are smaller than $\log k_{[2.66]}$ shown in Fig. 2.9. On the other hand, Gokcen et al. and McLean et al. derived e_{Al}^{O} using the next equation.

$$e_{Al}^{O} = (M_{Al} / M_O) e_O^{Al}. \qquad [2.70]$$

However, Eq. [2.70] would not be hold for the values of e_O^{Al} and e_{Al}^{O} derived assuming linear relations between $\log f_O$ and [%Al], and $\log f_{Al}$ and [%O]. The solid curves in Figs. 2.8 and 2.9 indicate that the relations between $\log f_O$

and [%Al], and $\log f_{Al}$ and [%O] are not linear.

(3) Deoxidation Constant K'

Gokcen et al. and McLean et al. derived K' from Eq. [2.71].

$$\log K' = \log([\%Al]^2[\%O]^3) + 3e_O^{Al}[\%Al] + 2e_{Al}^{O}[\%Al] \quad [2.71]$$

However, K' cannot be expressed by Eq. [2.71] because the relations between $\log f_O$ and [%Al], and $\log f_{Al}$ and [%O] are not linear, namely, $\log f_O$ and $\log f_{Al}$ cannot be expressed by the equations, $\log f_O = e_O^{Al}[\%Al]$ and $\log f_{Al} = e_{Al}^{O}[\%O]$. Rohde et al. derived $\log K'$ as intercept of linear line expressed by the next Eq.[2.72], and Kobayashi et al also derived $\log K'$ similarly from Eq.[2.73]. However $\log K'$ cannot be calculated from the equations. Therefore the reported values by various investigators are not consistent each other and all the values are larger than the values shown in Eq. [2.31].

$$\log([\%Al]^2[\%O]^3) = \log K' - (2e_{Al}^{Al} + 3e_O^{Al})[\%Al] \quad [2.72]$$

$$\log([\%Al]^2[\%O]^3) = \log K' - 3e_O^{Al}[\%Al] + \frac{2}{3}(M_{Al}/M_O)[\%O] \quad [2.73]$$

(4) Approximate Expression of $\log f_O$ and $\log f_{Al}$, and Interaction Coefficients

In the region [%Al]<0.1, following approximation can be done.

$$a_{O,\%}^{*} \approx [\%O]_{FeO},\ a_{Fe} \approx 1,\ M_T \approx M_{Fe},\ B \approx 1. \quad [2.74]$$

Therefore, from Eqs. [2.7], [2.17], and [2.19],

$$\log f_O \approx -\log\{1 + (400k_{FeO\cdot Al_2O_3} + 300k_{Al_2O_3}/a_O^{*})\, a_{Al}{}^2 a_O^{*3}\}, \quad [2.75]$$

and from Eqs. [2.7], [2.18], [2.20] and [2.55],

$$\log f_{Al} \approx -\log\{1 + (2k_{FeO\cdot Al_2O_3} + 2k_{Al_2O_3}) r^{\circ}_{Al} a_{Al} a^{*3}_{O}. \quad [2.76]$$

For any liquid Fe-Al-O alloy with negligible content of Al_2O(a) to which the approximation of Eq. [2.74] can be applied, including the alloy whose constitution is not on E.C., Eqs. [2.75] and [2.76] should hold.

The interaction coefficients at constant activity, $(\partial \log f_O / \partial[\%Al])_{a^*_{O,\%}}$ and $(\partial \log f_{Al} / \partial[\%O])_{a^*_{O,\%}}$, and the interaction coefficients at constant content, $(\partial \log f_O / \partial[\%Al])_{[\%Al]}$ and $(\partial \log f_{Al} / \partial[\%O])_{a^*_{O,\%}}$, derived in the present study based on associated solution model are not constant near or on the concentration region of E.C. Their values depend on aluminum and oxygen content and the values at any point of constitution do not coincide each other. On the contrary, the definition of interaction coefficient of Eq. [2.60] assumes tacitly that the partial differential calculus of logarithm of activity coefficient is constant and does not depend on the approaching way of [%Fe] to zero . However, in the present system, the definition of Eq. [2.16] should not be applied because the interaction between aluminum and oxygen is very large even in the extremely low aluminum and oxygen contents as the concentration region on and near E.C. Therefore, [2.64], [2.68], and [2.70]-[2.73] do not hold on E.C. of the present system. This is the main reason that the E.C. in Fig. 2.1 calculated from interaction coefficient does not agree with observed data.

V. Conclusion

Thermodynamic properties of Fe-Al-O dilute liquid alloy system in equilibrium with α-alumina was analyzed by an associated solution model assuming associated compounds (Al_2O_3(a), FeO(a), $FeO\cdot Al_2O_3$(a), Al_2O(a), Fe_3Al(a), FeAl(a) and $FeAl_3$(a)). The calculated equilibrium curves (E.C.) at 1873-

2183K, that is, the relations between log[%O] and log[%Al] of the liquid alloy at 1873-2183K, describes well the experimental data measured by various investigators. Following results were obtained by the present analyses.

(1) The E.C. at 1873-2183K, have minimum value of [%O] at 0.5-0.8 mass% Al, and minimum value of [%Al] at 0.007-0.045mass%O.

(2) The shape of the E.C. characterized by the minimums is caused by the concentration changes of the associated compounds.

(3) Calculated [%Al] of the liquid alloy in equilibrium with both of α-alumina and hercinite is 100 times larger than the aluminum activity, $a^{*}_{Al,\%}$, at 1873K.

(4) Aluminum contents insoluble in acid (*inslo Al*) in the liquid alloy were calculated by the assumption that it is consisted of solidified associated oxides (Al_2O_3(a), $FeO{\cdot}Al_2O_3$(a), Al_2O(a)). The calculated values of *inslo Al* are agreed with the observed data.

(5) The relationships between $\log f_O$ and [%Al], and $\log f_{Al}$ and [%O], are not linear but show curves. The discrepancies of the reported values of e_O^{Al}, e_{Al}^{O} and K' by various investigators are attributed to the treatments assuming that the relations are linear

Reference

1. Recommended Equilibrium Values for Reactions at Steel Making , revision and supplements, The 19th committee for Steelmaking, Japan Society for the Promotion of Science

2. L.E.Rohde, A.Choudhury and M.Wahlstar:Arch. Eisenhuttenw., **42**(1971), 165.

3. H.Wentrup and G.Hieber: ibid.,**13**(1939), 15.

4. D.C.Hilty and W.Crafts: Trans AIME, **188**(1950), 414.

5. O.Repetyro,M.Olette and P.Kozakevitch: J.Metals, May(1967),45.

6. Z.Buzek and A.Hulta: Freiberg.Forsch. -H., Reihe B, **117**(1969), 59.

7. H.Schenck, E.Steinmetz and K.K.Mehta: Arch. Eisenhuttenw., **41**(1970), 131.

8. N.A.Gokcen and J.Chipman:Trans. AIME, 197(1953), 173.

9. A.McLean and H.B.Bell: J.Iron Steel Inst., **203**(1953), 123.

10. J.H.Swischer: Trans Met. Soc. AIME, **239**(1967), 123.

11. K.Kobayashi, Y.Omori, K.Sanbongi: Tetsu-to-hagane, **53**(1967), 323

12. R.J.Fruehan: Metall. Trans., **1**(1970), 3403.

13. C.gatelleir and M.Olette: C. R. Akad.Sc. Paris, **277**(1973), 271.

14. D.Janke and W.A.Fischer: Arch. Eisenhuttenw., **47**(1976), 195.

15.J.C.d'Entremont, D.L.Guernsey and J.Chipman, Trans. Met. Soc.AIME, **227**(1963), 14.

16. G.R.Fitterer: Proc. Am. Inst. Min. Metall Pet. Ing. Natl., Open Hearth Basic Oxygen Steel Conf., **59**(1976), 212.

17. JANAF Thermochemical Tables, 1974,1975 and 1978 Supplements, Ed. by

M.W.Chase et al., Horikoshi Laboratory,Tokyo(1980),

18. C.K.Kim and A.McLean: Proc. Int. Symp. Met. Slag Gas React. Processes, Electrochemical Society, (1975), 284.
19. I.A.Novokhatskiy and B.F.Belov: Russian Metallurgy, Nr.1(1966),12.
20. K.Wasai and K.Mukai: J.Japan Inst.Metals, **49**(1985), 134.
21. K.Wasai and K.Mukai: J.Japan Inst.Metals, **45**(1981), 593.
22. K.Wasai and K.Mukai: J.Japan Inst.Metals, **46**(1982), 266.
23. K.Wasai and K.Mukai: J.Japan Inst.Metals, **52**(1988), 1088.
24. S.Otuka and Z.Kozuka: Trans.JIM, **22**(1981), 558.
25. R.Hultgren, P.D.Desai, D.H.Hawkins, M.Gleisen and K.K.Kelley:Selected Values of the Thermodynamic Prperties of Binary Alloys, American Society for Metals, (1973).
26. F.Woolley and J.F.Elliott: Trans.Met. Soc.AIME, **239**(1967), 1872.
27. K.Narita:Tetu-to-Hagane, **60**(1974), 1820.
28. M.Hansen and K.Anderko: Constitution of Binary Alloys, McGraw-Hill Book Co.,(1958).
29. T.Fujisawa, M.Suzuki, Y.Wanibe and H.Sakao:Tetu-to-Hagane, **72**(1968), 218.
30. U.Kuxmann and I.Rieche: Erzmetall, **25**(1972), 395.
31. U.Kuxmann and K.Geissler: Erzmetall, **30**(1977), 317.

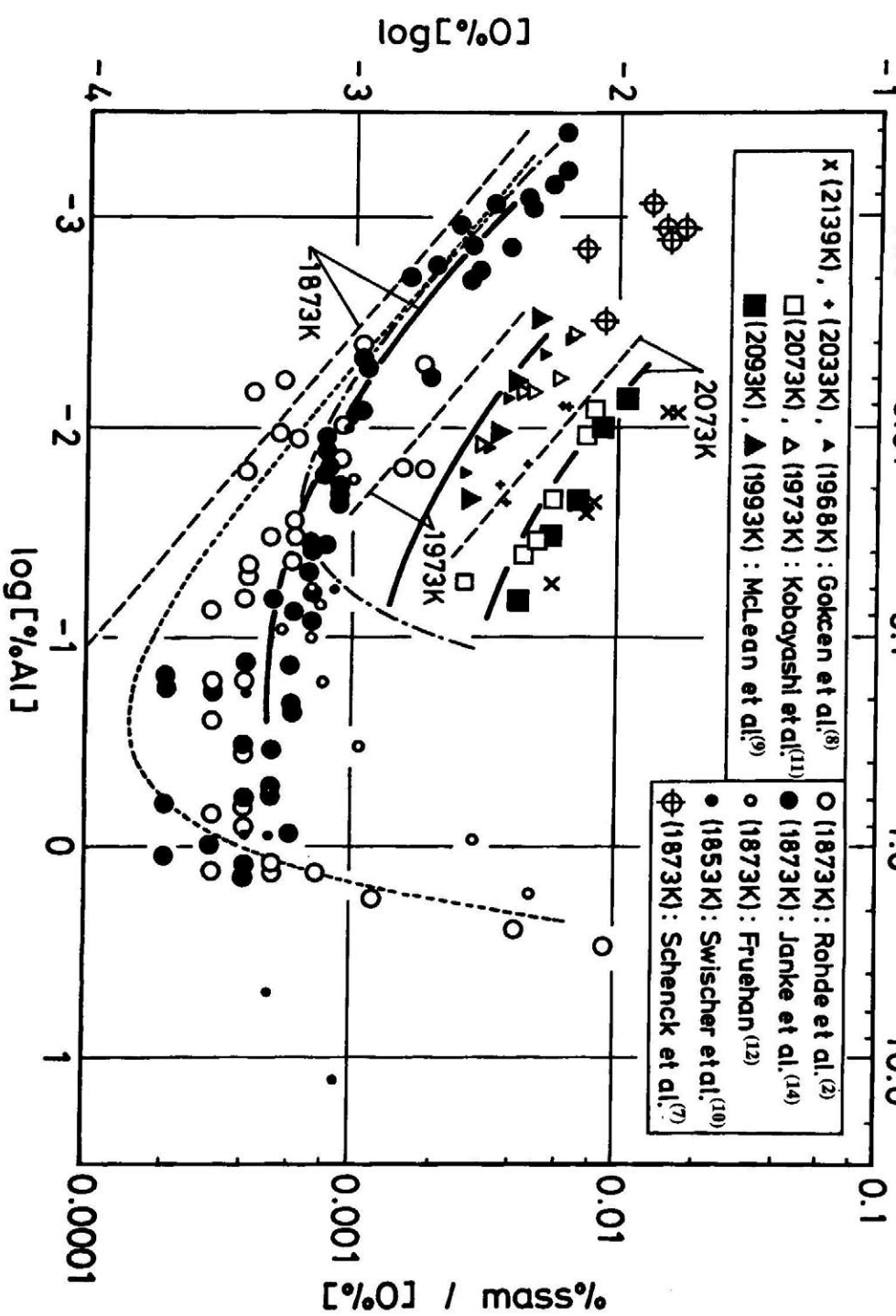

Fig. 2.1 Relations between log[%O] and log[%Al] obtained experimentally by various investigators and their regression curves (solid lines).
---; E.C. at 1873 K calculated from the recommended values of e_O^{Al}, e_{Al}^{O}, e_O^{O}, e_{Al}^{Al} and K'[1].
—·—; E.C. at 1873 K calculated from the values of e_O^{Al}, e_{Al}^{O} and K', reported by Gokcen *et al.*[8]
– – –; a_O^*,% calculated approximately from Eqs. [2.15], [2.30], [2.40] and [2.41]

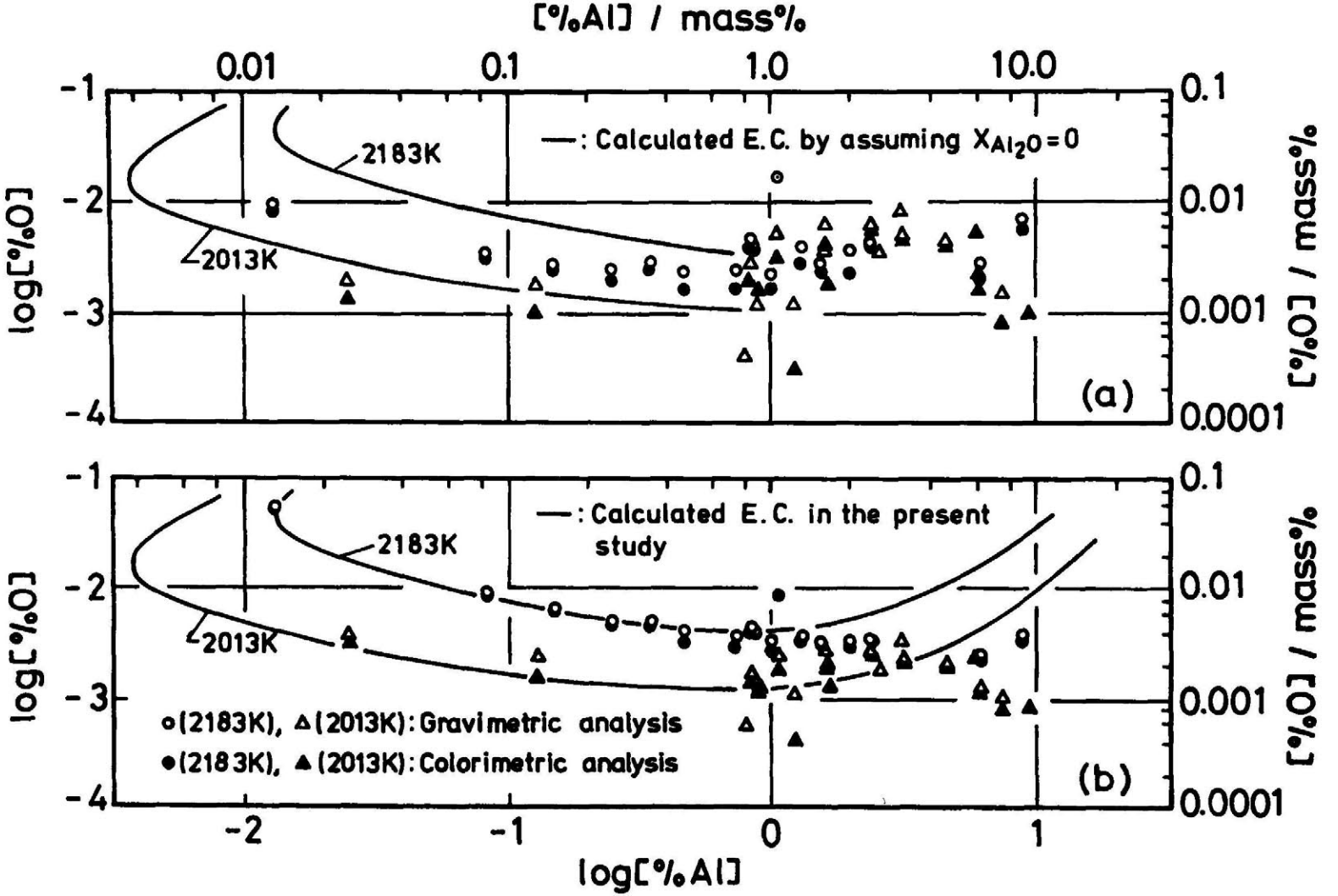

Fig. 2.2 (a) Relations between log[%O] and log[%Al] determined by d'Entremont *et al.*[15]
(b) Relations between logarithm of corrected [%O] and [%Al].

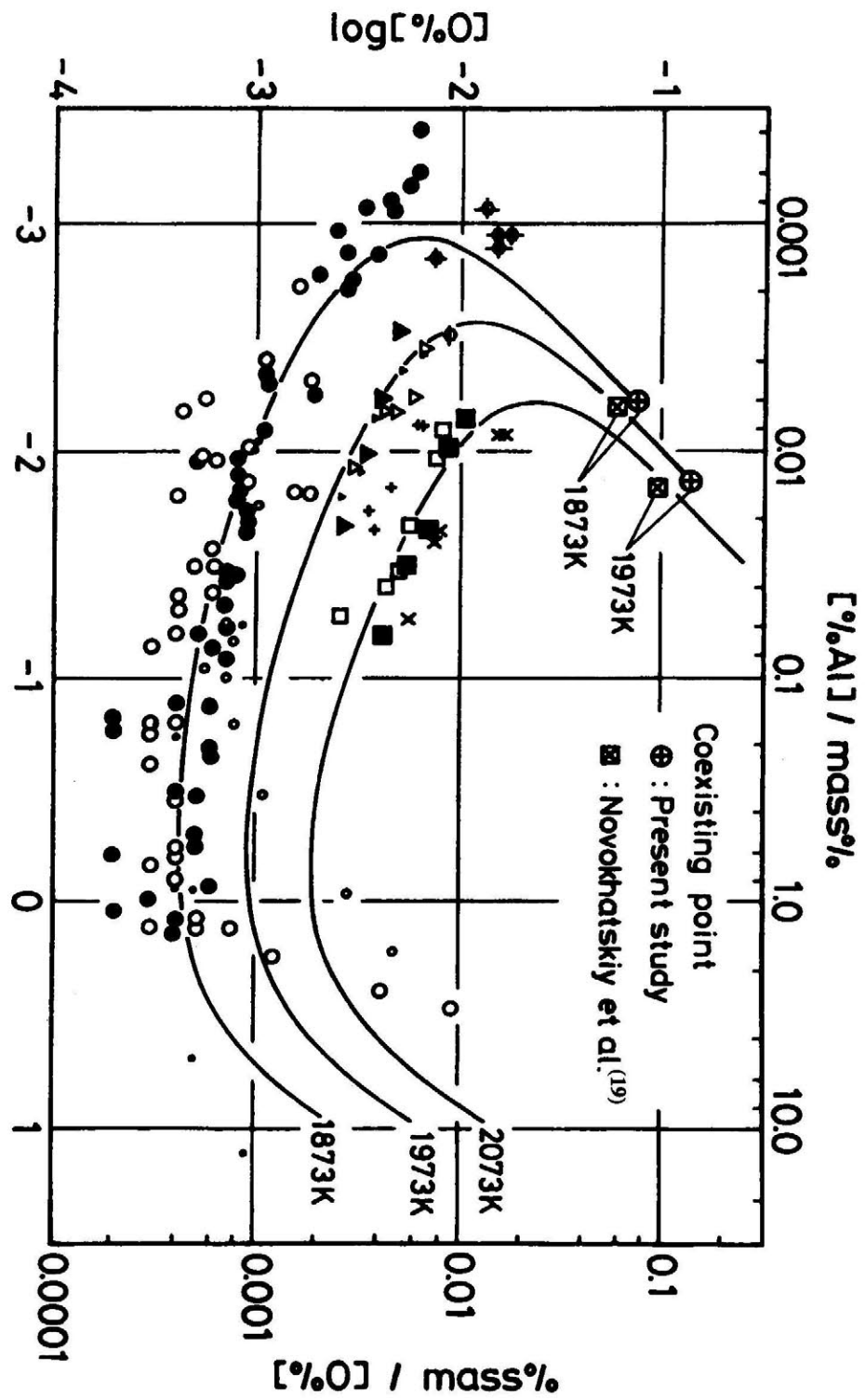

Fig. 2.3 E.C. (solid line) calculated in the present study. Other symbols except for ⊕ and ⊠ are the same as those of Fig.1-1.

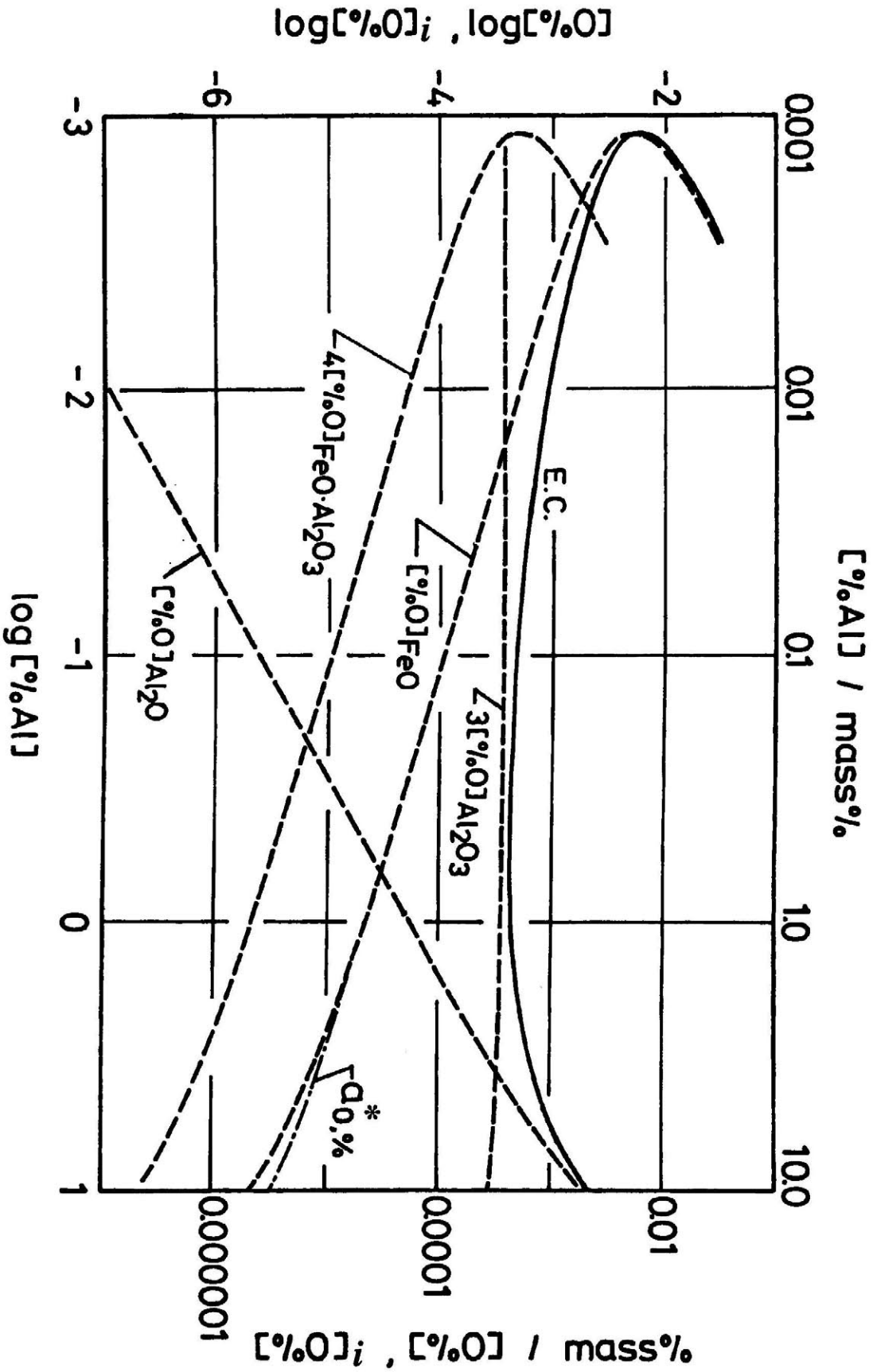

Fig. 2.4 Relation between r[%O]Fe$_p$ Al$_q$ O$_r$ and [%Al] at 1873K.

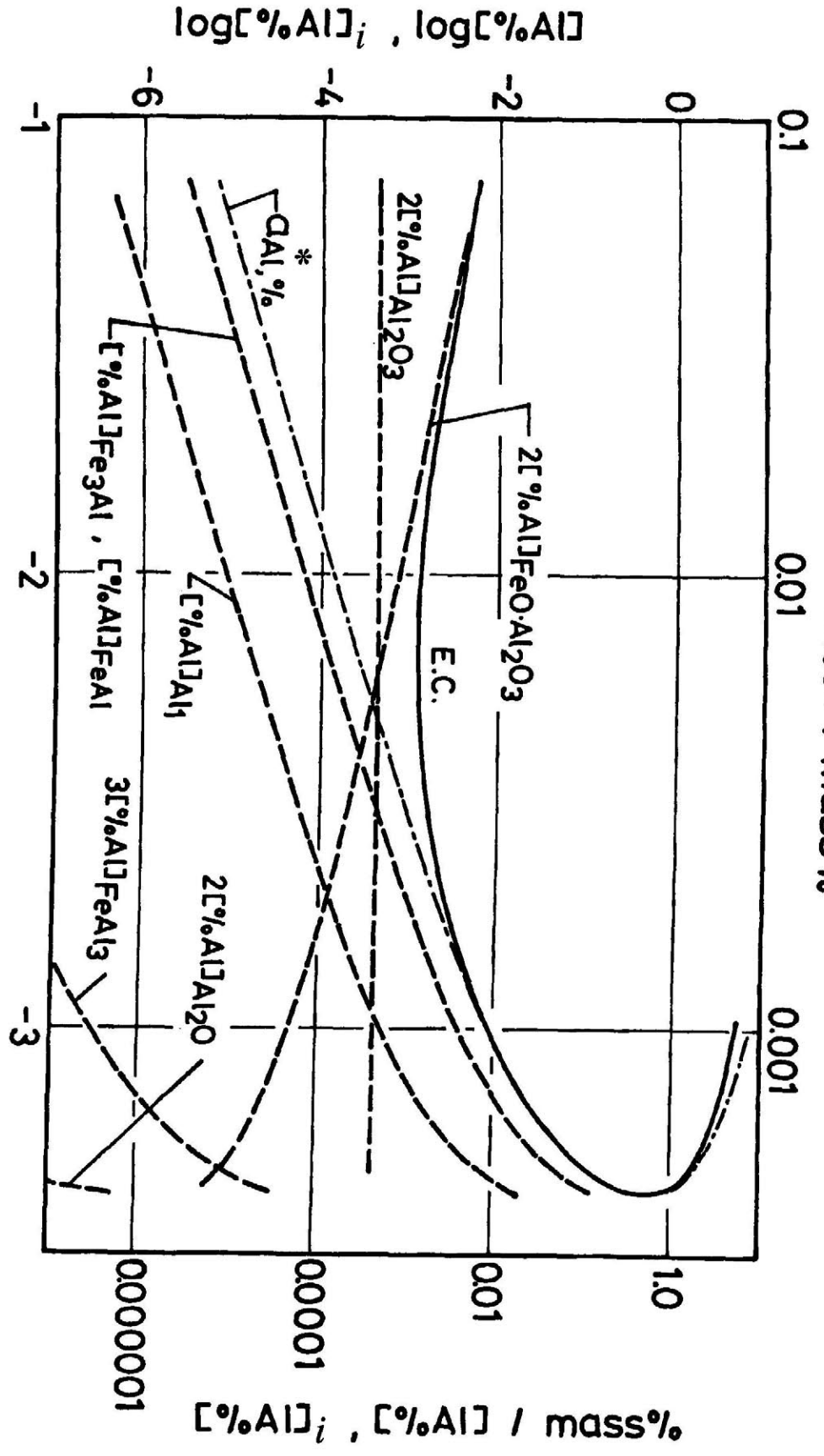

Fig. 2.5 Relation between r[%O]$_{Fe_p}$ Al$_q$ O$_r$ and [%Al] at 1873K.

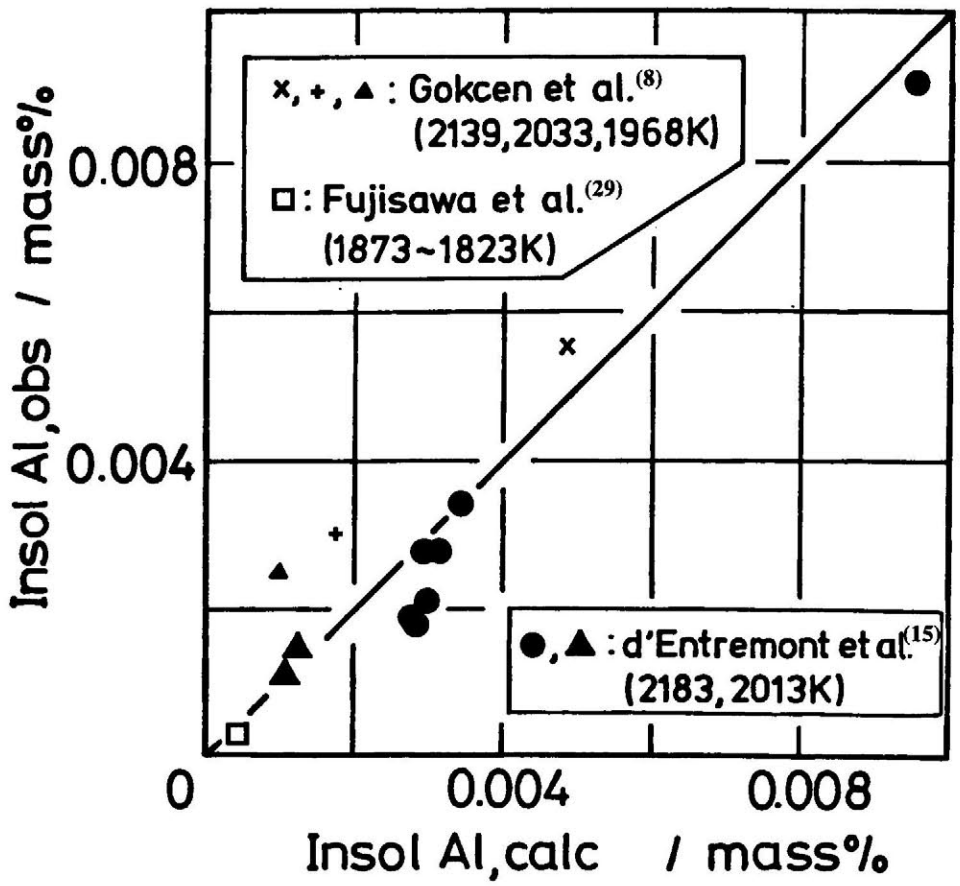

Fig. 2.6 Comparison between calculated and observed contents of *Insol Al.*

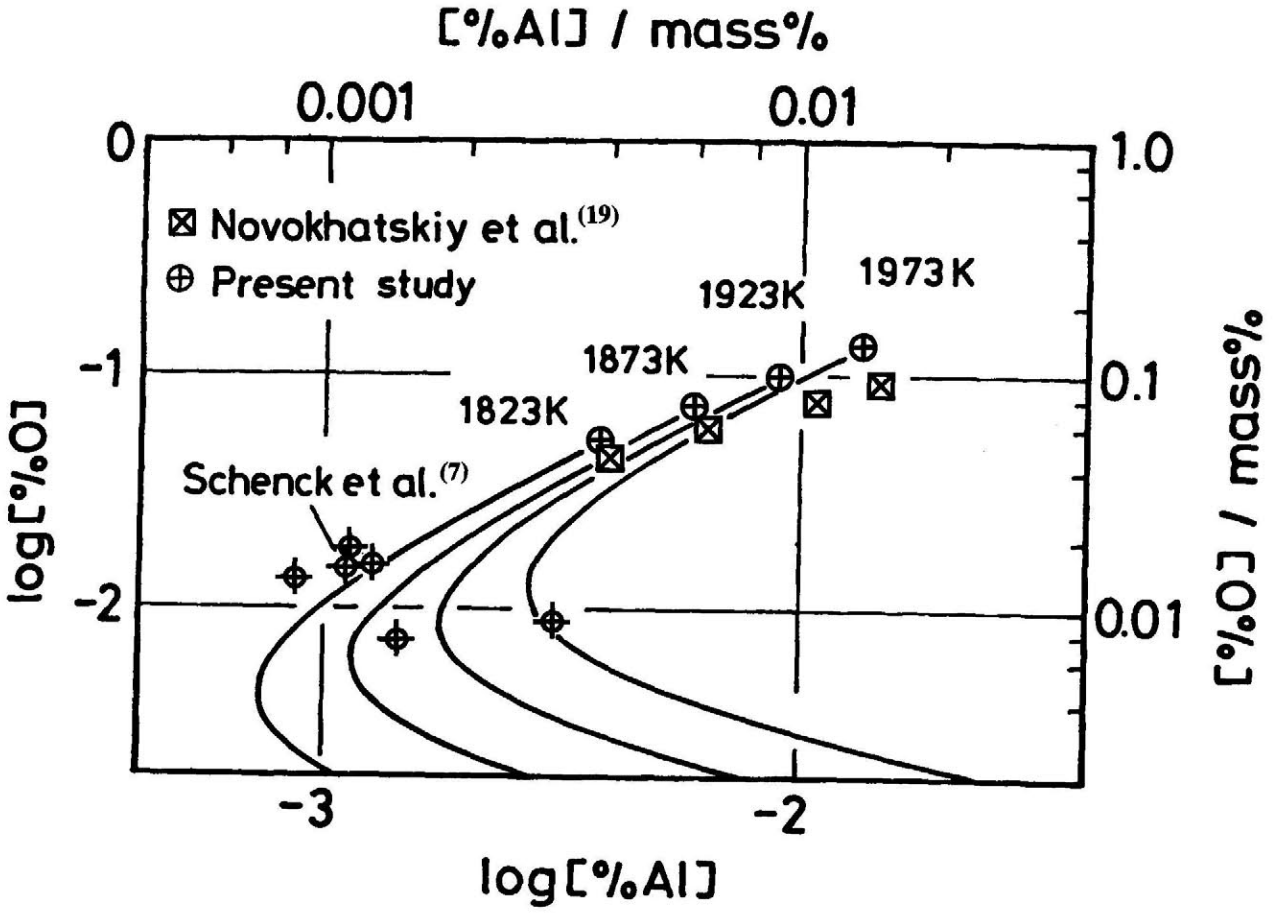

Fig. 2.7 Coexisting points on E.C. at 1823-1973K.

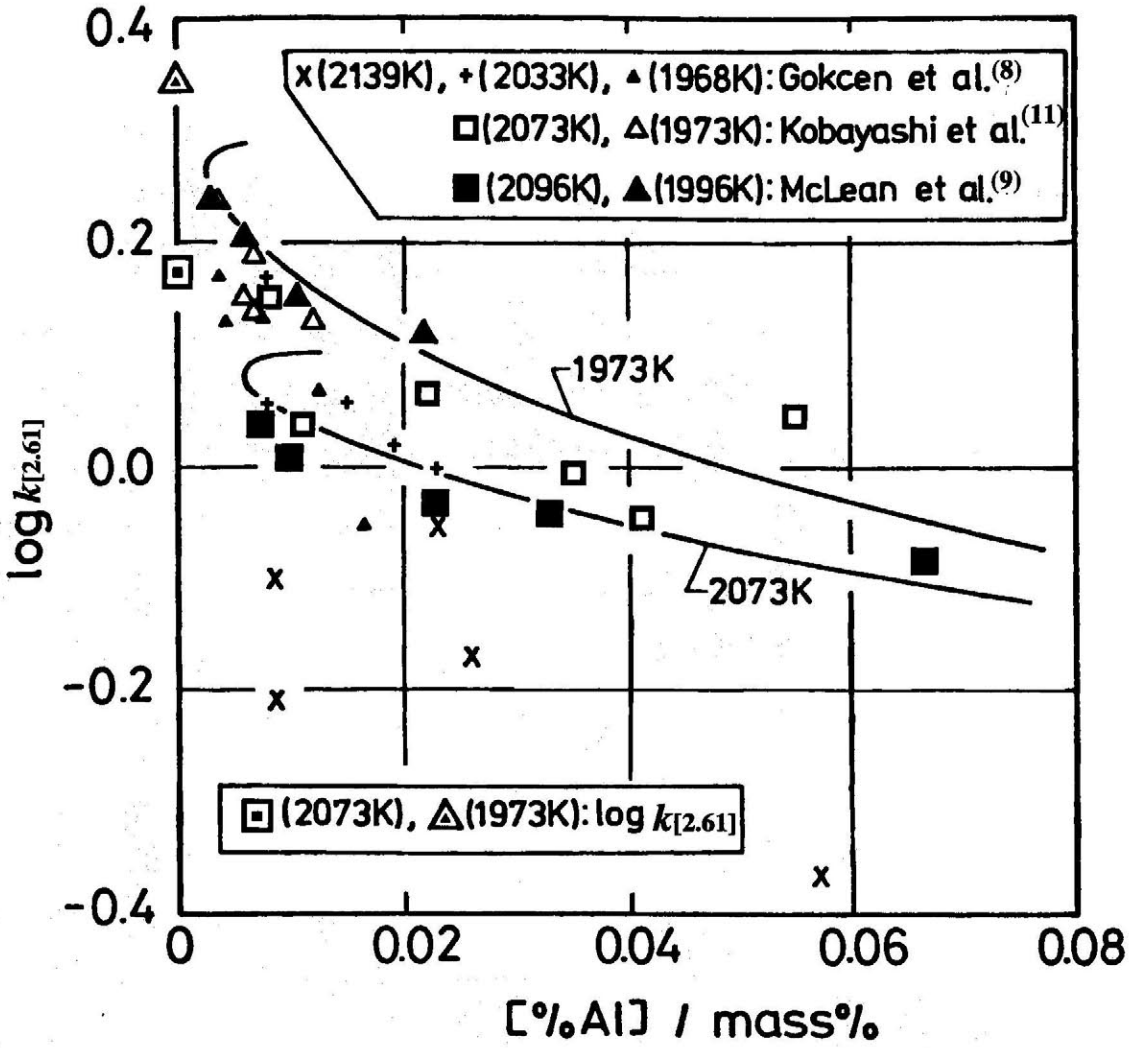

Fig. 2.8 Relation between $\log k'_{[2.61]}$ and [%O].

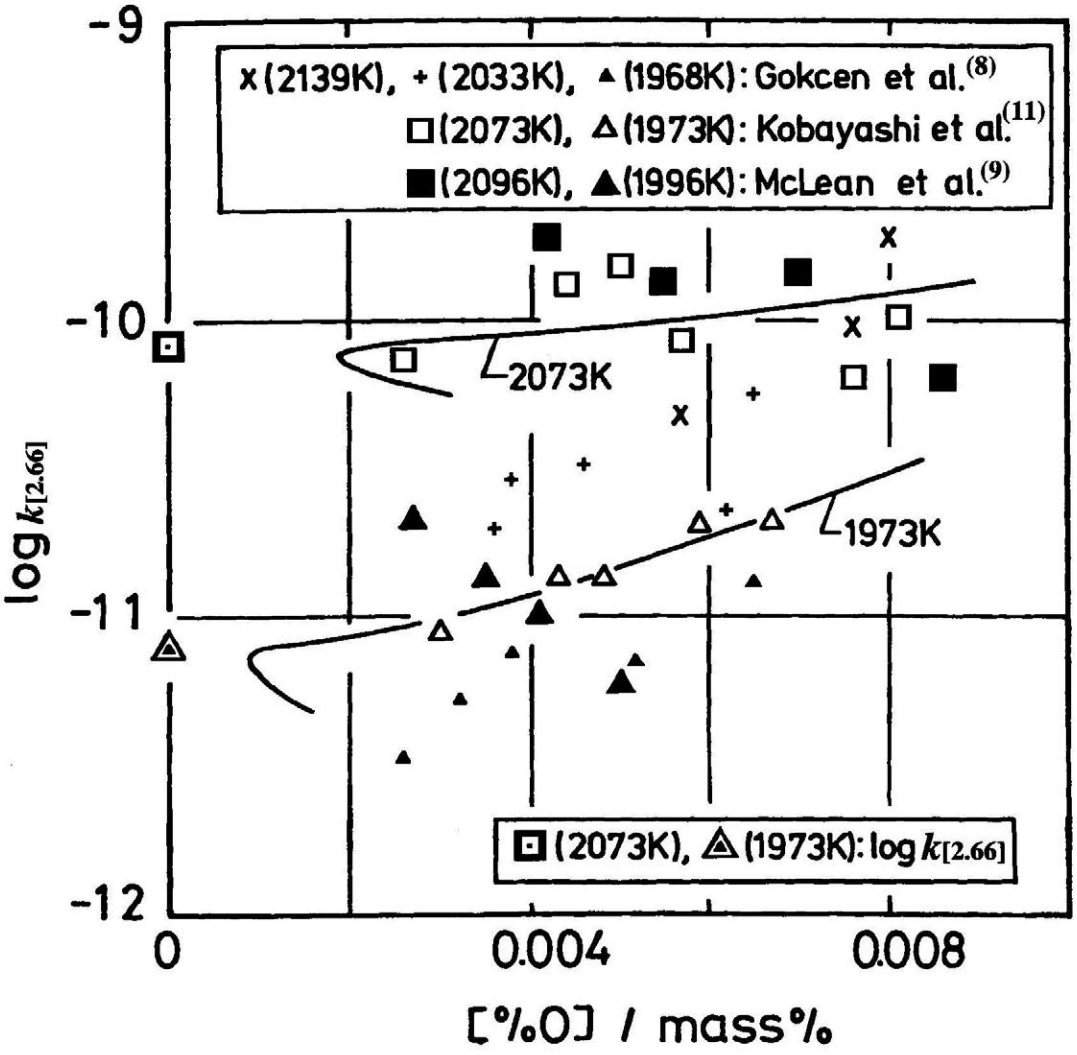

Fig. 2.9 Relation between log $k'_{[2.66]}$ and [%O].

Chapter 3 Thermodynamic Study on Liquid Iron in Equilibrium with α-Alumina and Hercynite

I. Introduction

When aluminum is used as a deoxidizer, alumina (Al_2O_3) is formed as a deoxidation product in liquid steel. If the oxygen content is high, hercynite ($FeO \cdot Al_2O_3$) is observed because liquid iron in equilibrium with α-alumina*[1] approaches the equilibrium of the three phases, liquid iron, solid hercynite and α-alumina.[1] At the equilibrium of these three phases, the system contains three components (Fe, Al, O) and three phases (liquid iron, solid hercynite and α-alumina). Therefore, the degree of freedom is zero if the pressure and temperature of the system are constant. Thus, this equilibrium occurs at only one point in the phase diagram under constant pressure and temperature.

If the oxygen content is higher than that at this point, the liquid iron equilibrates with solid hercynite. This point is hereafter referred to as the coexisting point.

The oxygen content of the liquid iron at this point at 1873K, has been reported by Kim et al.[2], Pillay et al.[3], McLean et al.[4], and Novokhatskiy et al.[5] (Table 3.I). In addition, Chan et al.[6] calculated the oxygen content from measurements performed using an oxygen sensor made from solid electrolyte, and Phelke et al.[7] reported in a study on nitrogen solubility into liquid iron that hercynite formed on the interface between liquid iron and solid alumina at over

*[1] In the present chapter, α-alumina is sometimes abbreviated as alumina.

0.07 mass%O. The respective oxygen contents reported in the above mentioned studies are in the range of 0.057-0.079 mass%O. The discrepancies between these findings are not so large considering the experimental difficulty associated with these studies. Only Novokhatskiy et al.[5] have measured the aluminum content of the coexisting point at 1873K. They reported the aluminum content of the coexisting point to be 0.007 mass%Al. Pillay et al.[7] reported that aluminum content of the coexisting point at 1973K is less than 0.0005 mass%, but the details of their analysis were not reported. However, according to a report by d'Entremont and Chipman[8], the coauthors of the Pillay study[7], published just after the pillay study[3], the aluminum content was analyzed on the assumption that aluminum content is equal to the acid insoluble aluminum (insol-Al) in liquid iron. However, aluminum content is not always equal to insol-Al. Hilty et al.[9] reported that the existence of a point (0.08 mass%O, 0.002 mass%Al) called the end point, which was reached either by melting oxidized electrolytic iron in alumina crucible or by adding wüstite (FeO) to a melt initially containing aluminum. Isn't this end point actually as any critical point in the phase diagram? We suppose it to be the coexisting point. However, the aluminum content of this end point (0.002 mass%Al) and the coexisting point measured by Novokhatskiy et al. (0.007 mass%Al)[5] are two orders of magnitude larger than the aluminum activity (8.2×10^{-6}) or the aluminum content (1.1×10^{-5} mass%) calculated for the oxygen content measured by Kim et al.[2] from the deoxidation constant K ($= a_{Al}^2 a_O^3$) and interaction parameters, e_{Al}^{O} , e_{O}^{Al} , etc.[10] Table 3.I shows the aluminum activity and aluminum content calculated using the oxygen content measured in the above mentioned studies. Generally, concentration is regarded as a good approximation of activity in dilute solution. In this case, the activity

coefficient calculated from the interaction parameter, e_{Al}^{O} [10], at the point measured by Kim et al. (0.074 mass%O)[2] is about 0.7. Thus, the aluminum contents measured by Novokhatskiy et al.[5] and Hilty et al.[9] are extraordinarily large.

In the previous chapter, the thermodynamic properties of liquid iron in equilibrium with α-alumina was analyzed on the basis of an associated solution model.[11] The results of the analysis showed that the aluminum and oxygen concentrations in liquid iron in equilibrium with α-alumina should produce a concave curve at the low aluminum region, as shown in Fig. 3.1*[2]. The coexisting point (solid circle) on this equilibrium curve (E.C.), which was determined so as to coincide to the oxygen content measured by Kim et al[2], is near the point reported by Novokhatskiy et al.[5] and Hilty et al.[9] Moreover, the data reported by Schenck et al.[14] lie near and along the concave part of this curve. Furthermore, similar concave equilibrium curves were reported experimentally in Cu-Ni-O [12] and Cu-Co-O[13] systems. In contrast, the E.C., which is calculated using the deoxidation constant K and interaction parameters[10], is almost linear, as shown in Fig. 3.1. This curve is also described in the book " Recommended Values of Equilibrium Constant for Steelmaking Reaction" in the old edition by the Japan Society Promotion of Science.[15] The aluminum contents calculated using K and interaction parameters at the coexisting point measured by Kim et al.[2] and Mclean et al.[4] lie along this curve, whereas the data reported by Schenck et al.[14],

*[2] The curve which gives the relationship between aluminum and oxygen in liquid iron in equilibrium with α-alumina is hereafter reffered to as the E.C. (equilibrium curve).

Novokhatskiy[5] and Hilty et al.[9] deviate from this curve. If this almost linear curve is the E.C., the aluminum contents calculated at the oxygen contents measured by Kim et al.[2] and Mclean et al.[4] are appropriate. In contrast, if the concave curve is the E.C., the coexisting point measured by Novokhatskiy et al.[5] would be appropriate, and therefore the interaction parameters used in the calculation of E.C. would be inappropriate in the concave curve region. This would have serious repercussion because the interaction parameters are used for estimating the activities of aluminum and oxygen in several fields of research. Therefore, not only for the purpose of investigating the inconsistency between aluminum activity and aluminum content, but also to clarify the thermodynamics of the liquid iron, an investigation of this coexisting point is essential.

II. Experimental Procedure

A. Experiment and Apparatus

The apparatus used in the present experiments is equipped with a vertical $LaCrO_3$ resistance furnace and a quenching vessel and is shown in Fig. 3.2. The Fe-O alloy and synthetic hercynite were dropped from the upper unit of the apparatus into a long crucible constructed of high grade alumina (13 x 9 x 1000mm 99.5 mass%). The bottom of the crucible was maintained at 1873K. After placement, the sample was maintained at 1873K for 1-14 hours. A series of five experiments were performed. The conditions of these experiments are as follows:

Experiment 1: 15g of Fe-O alloy (0.04-0.05 mass%$\underline{O}$) and 1g of hercynite were maintained at 1873K for 0-6 hours.

Experiment 2: 10g of Fe-O alloy (0.04-0.05 mass%$\underline{O}$) and 1g of hercynite

were maintained at 1873K for 6-10 hours.

Experiment 3: 5g of Fe-O alloy (0.04-0.05 mass%O) and 0.3g or 1g of hercynite were maintained at 1873K for 6-10 hours. After 4 or 7 hours, a bit of α-alumina was added.

Experiment 4: 5g of Fe-O alloy (0.083 mass%O) was maintained at 1873K for 0-10 hours.

Experiment 5: 5g of Fe-O alloy (0.039 mass%O) was maintained at 1873K for 0-14 hours.

At the final step of each of the experiments, the vessel used for quenching that was connected under the furnace was filled with water and the crucible was placed into the water to quench the sample. The Fe-O alloys (0.04-0.05 mass%O, 0.083 mass%O, 0.039 mass%O) were prepared by melting electrolytic iron and a chemical reagent of wüstite in a magnesia crucible using an induction furnace. The aluminum content of this Fe-O alloy was 0-0.0007 mass% and the Mg content was below 0.0001 mass%. The electrolytic iron used in the experiments contains 0.0014 mass%C, <0.0009 mass%S, <0.0010 mass%P, <0.0005 mass%Si, 0.0001 mass%Mn, 0.0001 mass%Cu and 0.0003 mass%N. All of the experiments were performed in an Ar atmosphere. The flow rate of the Ar gas was 50 ml/min.

B. Synthesis of Hercynite

A chemical reagent of Fe_tO powder, pure grade (1-t)Fe (99.99%) and α-Al_2O_3 powder (99.98%) were mixed by ball mill at a molar ratio of FeO/Al_2O_3=1/1.5 and then pressed into tablets and sealed in a quartz capsule evacuated to 10^{-6} Pa. This capsule was heated for three days in order to sinter the tablets. The sintered tablets were identified as $FeO{\cdot}Al_2O_3$(s) and Al_2O_3(s) by X-ray analysis.

Of the sintered tablets, 0.79 mass% Fe was soluble in HCl solution, indicating non-reacted iron, however no residual was dissolved into the acid.

C. Chemical Analysis

Each solidified iron sample had a diameter of approximately 9 mm. The height of solidified Samples 4 and 5 was about 12-13 mm. The rounded portion at the top and bottom of Samples 4 and 5 (about 2-3 mm in length) were removed. The remaining cylindrical samples were divided into two cylindrical pieces and each of these pieces were then divided lengthwise. These sets of the upper and lower sections of Samples 4 and 5 were used for oxygen and aluminum determination. The top portions into which hercynite immersed and the bottom portions (2-3mm in length), were removed from Samples 1 and 2. The uppermost and lowermost 1 g portions of the remaining iron samples were used for the oxygen analysis. Since Sample 3 was small and the hercynite and alumina were immersed into the iron somewhat deeply, only the lowest portion of the sample was analyzed.

The oxygen content of the samples was determined by inert-gas fusion-infrared absorptiometry (LECO, TC-136). The iron was dissolved in HCl solution, and the solution was filtered using a polycarbonate filter, the pores of which are 0.1 μm in diameter. The filtrate was analyzed for acid soluble aluminum content (sol-Al) by inductively coupled plasma emission spectrometry (ICP). The residue on the filter was fused with potassium disulfate in a Pt crucible and then dissolved in a dilute HCl solution. Acid insoluble aluminum (insol-Al) in this solution was analyzed by ICP.

Since the aluminum content of coexisting point is very low, the analysis should have high accuracy. The chemical analysis of "Japanese Iron and Steel

Certified Reference Material for Aluminum Determination" was performed seven times. The certified sol-Al value of this reference material is 0.0045±0.00045 mass% and the total aluminum is 0.0057±0.00048 mass%. The results of the analyses are shown in Fig. 3.3. Though the difference between the maximum and minimum values of the total aluminum contents in Fig. 3.3 is about 0.0015 mass%, all of the present results are in the range of 0.0057±0.0006 mass%, except for a minimum value. They are also in the scattering range of the values tested by the "Japanese Iron and Steel Institute", as reported in the papers that were included with the reference material.

III. Results of the Experiment

A. Change in Oxygen Content with respect to Time

The changes in oxygen contents in liquid iron with respect to time of Samples 1-3 are shown in Fig. 3.4 and the changes in oxygen contents for Samples 4 and 5 are shown in Fig. 3.5. The oxygen contents for Samples 1 and 2 appear to follow a similar pattern, and differences from 0.003 to 0.008 mass%O are observed between the oxygen content values for the upper and lower portions of each sample, which is somewhat larger than the analytical error. The differences between the upper and lower portions of Samples 4 and 5 are in the range of 0.001 mass%-0.003 mass%, which is regarded as appropriate within the analytical error. For Sample 1, no formation of hercynite was observed on the wall of the alumina crucible after 4 hours. After 6 hours, the greenish gray hercynite was observed on the wall of the crucible. After 8 hours, the oxygen contents of Samples 1-3 approached 0.072 mass%O and the walls of the crucibles were covered with hercynite. Thus, these samples probably reached equilibrium after 8 hours. Nevertheless, the oxygen contents of Samples 2 and 3 increased even after 8 hours. In contrast, the oxygen

content of Sample 4 decreased from the initial value (0.083 mass%O) until reaching 0.073 mass%O after 4 hours, after that, the oxygen value remained at about 0.072 mass%O for an additional 6 hours. The oxygen content of Sample 5 increased gradually and approached 0.072 mass%O after 12-14 hours. Therefore, Samples 4 and 5 are considered to have reached equilibrium after 4 and 12 hours, respectively. The mean oxygen content of these Samples 4 and 5 maintained at 1873K for 4-10 hours and for 12-14 hours, respectively, is 0.072mass%O.

B. Change in Aluminum Content with respect to Time

The changes in total aluminum contents in liquid iron with respect to time is shown in Fig. 3.6. In Fig. 3.6, the error bars show the scattering, ±0.0006 mass%, of the analyzed aluminum in the present experiment. Samples 1-3 show somewhat scattered values of aluminum. Figure 3.6 shows the average aluminum contents of the upper and lower portions of Samples 4 and 5. A few of the data represent the aluminum content for either the upper or lower portion due to failed analyses. The analyzed aluminum contents of the upper and lower portions of Samples 4 and 5 agree within the respective errors of analysis. The aluminum content increased from the initial aluminum content, and the mean aluminum content of Samples 4 and 5 maintained at 1873K for 4-10 hours and for 12-14 hours, respectively, is 0.0018mass%Al.

C. Formation of Hercynite and X-ray Analysis

Hercynite was observed to form over entire interface between the crucible and iron for Sample 4 maintained at 1873K for over 4 hours. For Sample 5 maintained at 6 and 8 hours, traces of hercynite were observed on the crucible wall, and when maintained for over 10 hours, hercynite was observed to have

formed over the entire interface. Hercynite is often observed to be attached to the side surface of solidified iron after quenching. Figure 3.7 shows an EPMA image of hercynite attached to the side of the solidified iron Sample 4 maintained at 1873K for 8 hours. Figure 3.7 reveals that the hercynite attached to the iron is constituted of several grains and does not penetrate into the iron. Between the grains of hercynite, grains of alumina are observable. Wüstite would be absorbed into alumina through these grain boundaries and reacts to form hercynite. Figure 3.7 shows the hercynite and α-alumina attaching to the solidified iron . Furthermore, X-ray analyses of the inner wall of the crucible of Sample 4 after 10 hours and that of Sample 5 after 14 hours revealed that both hercynite and α-alumina were present on the wall.

IV. Discussion

A. Equilibrium Condition

(1) Heterogeneous Distribution of Oxygen Content

The oxygen heterogeneity for the upper and lower portions of the iron sample was observed even in Sample 2 when maintained for 10 hours, and the oxygen content for Samples 2 and 3 increased after reaching equilibrium. In contrast, the oxygen content for Samples 4 and 5 level out after reaching 0.072 mass%O. If both of alumina and hercynite exist after equilibrium is reached, the condition of equilibrium should continue. Hercynite was added to Samples 1, 2, and 3, but not to Samples 4 and 5. The hercynite floated on the liquid iron, and the bottom of the hercynite was immersed in the iron. If the initial oxygen is lower than equilibrium, the hercynite might decompose to wüstite (FeO) and alumina The decomposed wüstite*[3] might dissolve into the upper liquid iron and diffuse

*[3] From the standpoint of the associated solution model, oxygen in

into the lower liquid iron. Still, the hercynite could not decompose once the system reached equilibrium. Furthermore, the oxygen content of Sample 5, to which no hercynite was added, also increased with time. Accordingly, oxygen sources other than hercynite should exist in these Samples from 1 to 5 and the wüstite from the hercynite would play only a slight role in the increase in oxygen content of Samples 1, 2, and 3.

The argon gas used in the present experiment is the ultra high grade material and has a 99.999 volume% purity, and the O_2 content of this gas is below 0.0002 volume%. For instance, the 0.00005 volume%$\underline{O}$ in the gas phase corresponds to a partial pressure of O_2 about $5x10^{-7}$ atm. This is certainly larger than the partial pressure of O_2 in equilibrium with the liquid iron at coexisting point ($8x10^{-10}$ atm[2]). Therefore, the O_2 gas in the Ar gas would be a main source of oxygen and it dissolve into liquid iron until the iron reaches equilibrium.

As mentioned above, the phenomenon of excess dissolution of oxygen beyond the equilibrium value occurs only when synthetic hercynite is floating on the liquid iron. According to a report by Ficher et al.[16], Fe_3O_4 is soluble in hercynite and the wüstite contains Fe^{+++} to some extent, even in the highest grade of chemical reagent of wüstite. This chemical reagent of wüstite is one of the material used to synthesize hercynite in this experiment Therefore, the following process might occur: the surface of the liquid iron is saturated with wüstite due to a reaction with O_2 gas; this wüstite content is in excess of the bulk content and a part of it diffuses to the bulk; another part of it reacts with $iron^{+++}$ in hercynite and Fe_3O_4 is formed; thus, oxygen is absorbed into hercynite at the interface of the three-phase region (hercynite, liquid iron and gas), which could

liquid iron exists as a type of associated compound FeO(a).

occur under the condition at which the oxygen potential in the gas phase is larger than the equilibrium value of the coexisting point; finally the oxygen absorbed as Fe_3O_4 is transported to the lower part of the hercynite and dissolves into the liquid iron because the oxygen potential in the bulk iron is smaller than that at the upper surface. This process would cause the increase of oxygen content at the upper part of the iron. Furthermore, the reaction continues even after equilibrium is reached as long as the oxygen potential difference exists between the three phase interface and the lower part of the hercynite. Kim et al. and McLean et al. also added synthetic hercynite to the liquid iron, but they compacted it to the bottom of the alumina crucible. Thus, the synthetic hercynite did not float up on liquid iron in their experiment, and the liquid iron was able to reach equilibrium.

After the hercynite forms on the inner surface of the crucible, as is the case for Samples 4 and 5, another new three-phase interface appears between this newly formed hercynite, the liquid iron and the gas phase. However, no excess dissolution of oxygen was observed for Samples 4 and 5. Although this seems to be a contradiction, this may be due to the fact that the pure hercynite on the crucible contains no $iron^{+++}$.

(2) The Mechanism of Oxygen Dissolution

As stated above, the direct oxygen dissolution from the gas phase should occur at the top surface, and the wüstite dissolution through hercynite should also occur at the interface between liquid iron and floating hercynite. The latter should cause the excess dissolution of oxygen. But the upper interface areas of these two dissolution reactions would be almost the same for Samples 1 to 3. Thus, if only these two reactions at the top of the sample occurred, the oxygen dissolution speed, which is equal to the slope of the oxygen change in

Fig. 3.4, should decrease as the sample weight increases. However, from Fig. 3.4, the oxygen contents of these three samples appear to increase with time in similar manner. Consequently, some kind of dissolution of oxygen may occur at the interface between liquid iron and alumina. If so, the slope of the oxygen change in Fig. 3.4 is well explained because this interface area between liquid iron and alumina would change roughly in proportion to the weight of the sample. For example, the wüstite absorbed into the grain boundaries of alumina at the upper surface might be carried to the lower part of the alumina crucible and dissolve into liquid iron or form hercynite. Furthermore, the dissociation of alumina or another kind of unknown reaction might occur. However, further discussion of the mechanism of oxygen dissolution is not possible due to a lack of information.

(3) Formation of Hercynite

Another unclear heterogeneity remains to be discussed: the heterogeneous formation of hercynite before attaining equilibrium, as observed in Sample 5 at 6 hours, although trace formations were observed on the crucible. This could be explained by the fact that partial equilibrium occurred at the wall of the crucible. The liquid iron located directly next to the alumina crucible would reach equilibrium locally after a few hours, and hercynite would start to form on the wall of the crucible. However, the iron apart from this location does not yet attain equilibrium. This heterogeneous formation of hercynite should remain until the entire iron sample reaches equilibrium and hercynite is formed over the entire inner surface of the crucible. The oxygen content of Sample 3 after 8 hours is slightly lower than that of the lower portion of Sample 2. This is probably a result of the consumption of oxygen due to the formation of hercynite on the alumina added at 4 or 7 hours. However, Fig. 3.7 shows that

the surface was covered not only with hercynite but also with alumina, which was in contact with liquid iron for hours after reaching equilibrium.

(4) Coexisting Point

Based on the above considerations, the coexisting point obtained in the present study is 0.072 mass%O and 0.0018 mass%Al. Although the overall equilibrium, including gas phase, was not obtained, restricting the system to the three phases of hercynite, alumina and liquid iron, allowed the coexisting point to be determined as close as possible to equilibrium. Furthermore, the obtained values are fairly precise because the curves in Fig. 3.5 approach each other, and the oxygen content are maintained almost constant for 4 to 6 hours after reaching equilibrium. The aluminum content also increased from the initial aluminum content level and approached the coexisting point. Although the scattering of aluminum is somewhat large due to the difficulty of analysis, the aluminum content is clearly about 0.0018 mass% and is not of the degree of magnitude of $1x10^{-5}$.

B. Comparison with Results by Other Investigators

Table 3.I shows that the oxygen content of the coexisting point observed in the present work agrees approximately with the measured values by Kim et al.[2], Pillay et al.[3] and Chan et al.[6] The data of McLean et al.[4] and Novokhatskiy et al.[5] are smaller than the data reported in these studies. This discrepancy may be due to slight error in temperature measurement or to the effects of impurities. The effects of Mn, Si or Cr were reported by Kim et al.[2] In addition, Kim et al.[17] reported that Mn impurity in iron causes oxygen content to decrease. The iron used in the present experiment is electrolytic iron, the purity of which is better than that in other measurements. The temperature

measurement by McLean et al.[4] was performed using a two-color radiation pyrometer that would have caused slight error in temperature measurement. With the exception of Chan et al.[6], all other studies measured temperature using an optical pyrometer, although the detailed experimental conditions used by Novokhatskiy et al.[5] and Pillay et al.[3] are not known. In the present study, temperature was measured using a 20-40%Rh/Pt thermocouple having an error within ±3K, which is more precise than the optical pyrometer.

Although the aluminum content of the coexisting point is somewhat smaller than that of Novokhatskiy et al.[5], the result of the present study agrees very well with that reported by Hilty et al.[9]

C. Equilibrium Curve and Associated Solution Model

The present experiment revealed that the location of the coexisting point is higher in the aluminum region than many researchers believe. Thus, an approximation as $a_{Al} \approx$ [mass%$\underline{Al}$] is not appropriate for the high oxygen region. Thereforer, the E.C. is not linear but rather a concave curve, the end of which is the coexisting point, as shown in Fig. 3.1. Thus, the e_{Al}^{O} and e_{O}^{Al} values used for the calculation of this curve are inappropriate in this region. The reported values of e_{Al}^{O} and e_{O}^{Al} [10] are the measured values in the $\underline{O}$ region lower than 0.01 mass% $\underline{O}$; however, these values have been used often, even in the higher $\underline{O}$ region. Thus, extreme care and deliberation are required for the effective concentration limit of the interaction parameters, and the reexamination of the interaction parameters and the thermodynamics of this system over a wide concentration region that covers the entire E.C. in Fig. 3.1 is necessary.

In addition, the present study clarified that the location of the coexisting point is able to be predicted by the associated solution model. However, the

coexisting point calculated using this model is slightly larger in aluminum content than the present results. Therefore, recalculation by this model would be necessary and further discussion and investigation of the effectiveness of the associated solution model is expected in various fields of research.

V. Conclusion

1. The oxygen and aluminum contents at the coexisting point at 1873K, at which liquid iron was in equilibrium with hercynite and α-alumina, were determined. The obtained contents at this point are 0.072 mass%O and 0.0018 mass%Al. Thus, the E.C., on which liquid iron is in equilibrium with α-alumina, is not a straight line, but rather is a concave curve.

2. The aluminum content of the coexisting point is two orders of magnitude larger than the activity of aluminum, which indicates that the interaction parameters reported for the Fe-Al-O system are not appropriate in the high oxygen region. The rexamination of the interaction parameters and the thermodynamics of this system are necessary.

3. The synthetic hercynite which was added to the liquid iron in the present experiment, acted as a catalyst for leading oxygen into liquid iron, even after the iron reached equilibrium. Thus, the experiment was performed with no addition of synthetic hercynite. Hercynite was formed naturally on the wall of the α-alumina crucible during the experiment.

4. The effectiveness of the associated solution model which is capable of predicting the coexisting point to a fair degree of precision, should be further investigated in various fields of research.

References

1. E.Schürmann and N.Bannenberg : Arch. Eisenhüttenwes., 55(1984), 409.
2. C.K.Kim and A.McLean : Proceedings of Int.Symp.Met.Slag Gas Reactions and Processes, Toronto, Canada (1975), Electrochemical Soc., 284.
3. T.C.Pillay, J.d'Entremont and J.Chipman : J.Amer.Ceram.Soc., 43(1960), 583.
4. A.McLean and R.G.Ward : J.Iron Steel.Inst., (1966), 8.
5. I.A.Novokhatskiy and B.F.Belov : Russian Metall., (1966), Nr.1,12.
6. J.C.Chan, C.B.Alcock and K.T.Jacob : Can.Met.Quart., 12(1973), 439.
7. R.D.Pehlke and J.F.Elliott : Trans.Meta.Soc.AIME, 218(1960), 1088.
8. J.C.d'Entremont, D.L.Guernsey and J.Chipman : Trans.Meta.Soc.AIME, 227(1963), 14.
9. D.C.Hilty and W.Crafts : Trans AIME, 188(1950), J. Metal., 414.
10. Recommended Values of Equilibrium Constant for Steelmaking Reaction, A Revised and Enlarged Edition by The 19th Committee (Steelmaking) of The Japan Soc. Promotion of Sci., Rep. No. 10588 (Nov. 1984), 38.
11. K.Wasai and K.Mukai : J.Japan.Inst.Metals, 52(1988), 1088.
12. U.Kuxmann and J.Reiche : Erzmetall, 25(1972), 395.
13). U.Kuxmann and J.Geissler : Erzmetall, 30(1977), 317.
14. H.Schenck, E.Steinmetz and K.K.mehta : Arch.Eisenhüttenw, 41(1970), 131.
15. Recommended Values of Equilibrium Constant for Steelmaking Reaction, Edited by The 19th Committee (Steelmaking) of The Japan Soc. Promotion of Sci., Nikkan-Kogyo Publishers (1978).

16. W.A.Fischer and A.Hoffmann : Arch.Eisenhüttenw, 26(1955), 43.

17. C.K.Kim and A.McLean : Meta. Trans.B, 10B(1979), 575.

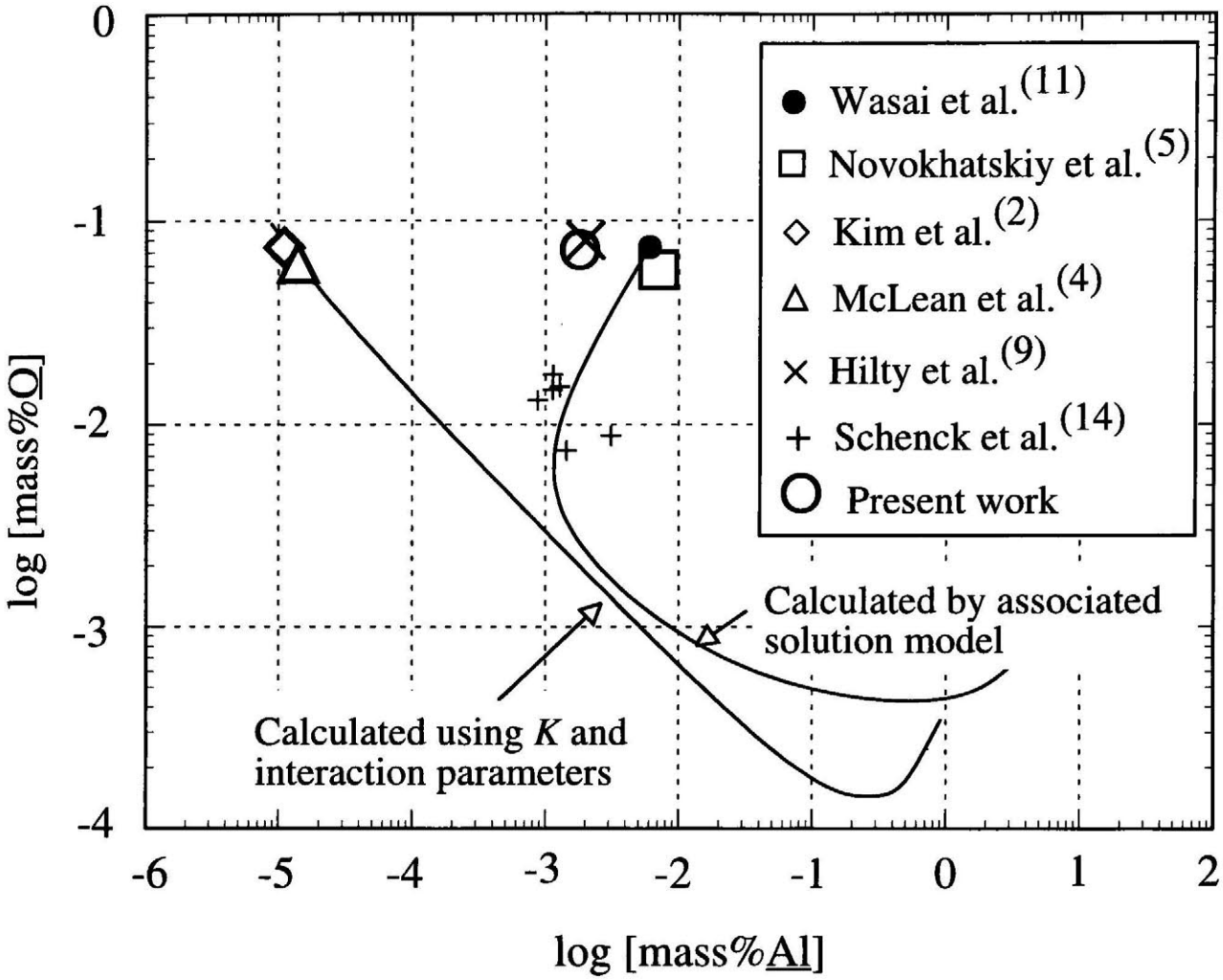

Fig. 3.1 Coexisting point as reported in various studies. The two solid curves show the equilibrium curves calculated by associated solution model and using K and interaction parameters, respectively.

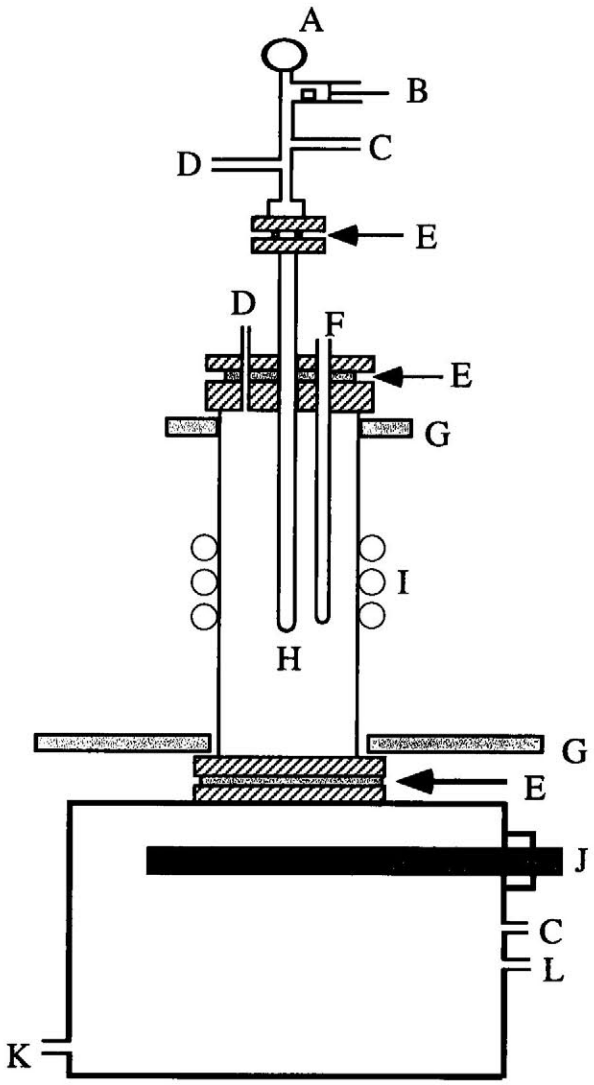

A: Pressure gage
B: Sample loading device
C: Gas inlet
D: Gas outlet
E: O-ring
F: Thermocouple sheath
G: Cooling device
H: Alumina crucible
I: $LaCrO_3$ Heater
J: Shutter
K: Water inlet
L: Water outlet

Fig. 3.2 Schematic diagram of the experimental apparatus.

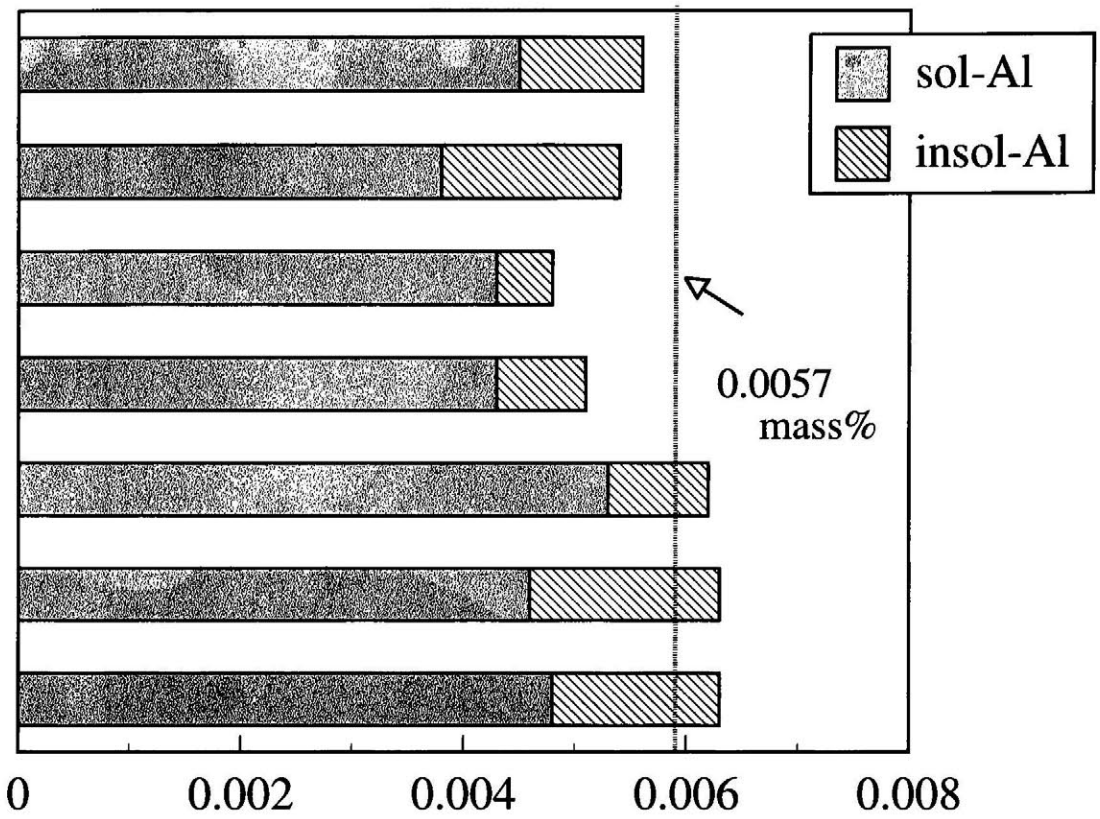

Fig.3-3 Results of aluminum analysis performed according to Japanese Iron and Steel Certified Reference Material. (Certified value: sol-Al=0.0045±0.00045 mass%, total-Al =0.0057±0.00048 mass%)

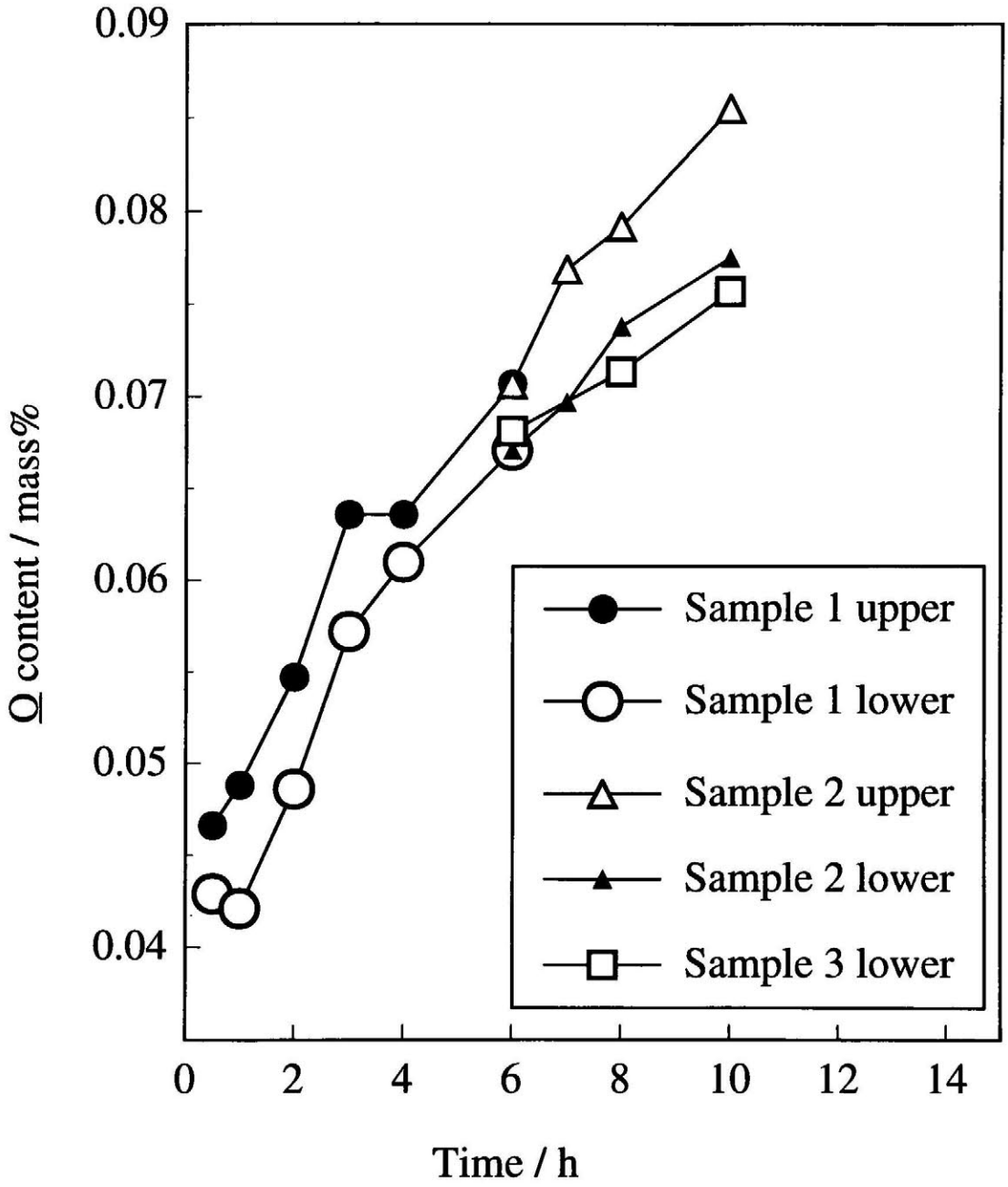

Fig. 3.4 Change in oxygen content for Samples 1-3 with respect to holding time at 1873K.

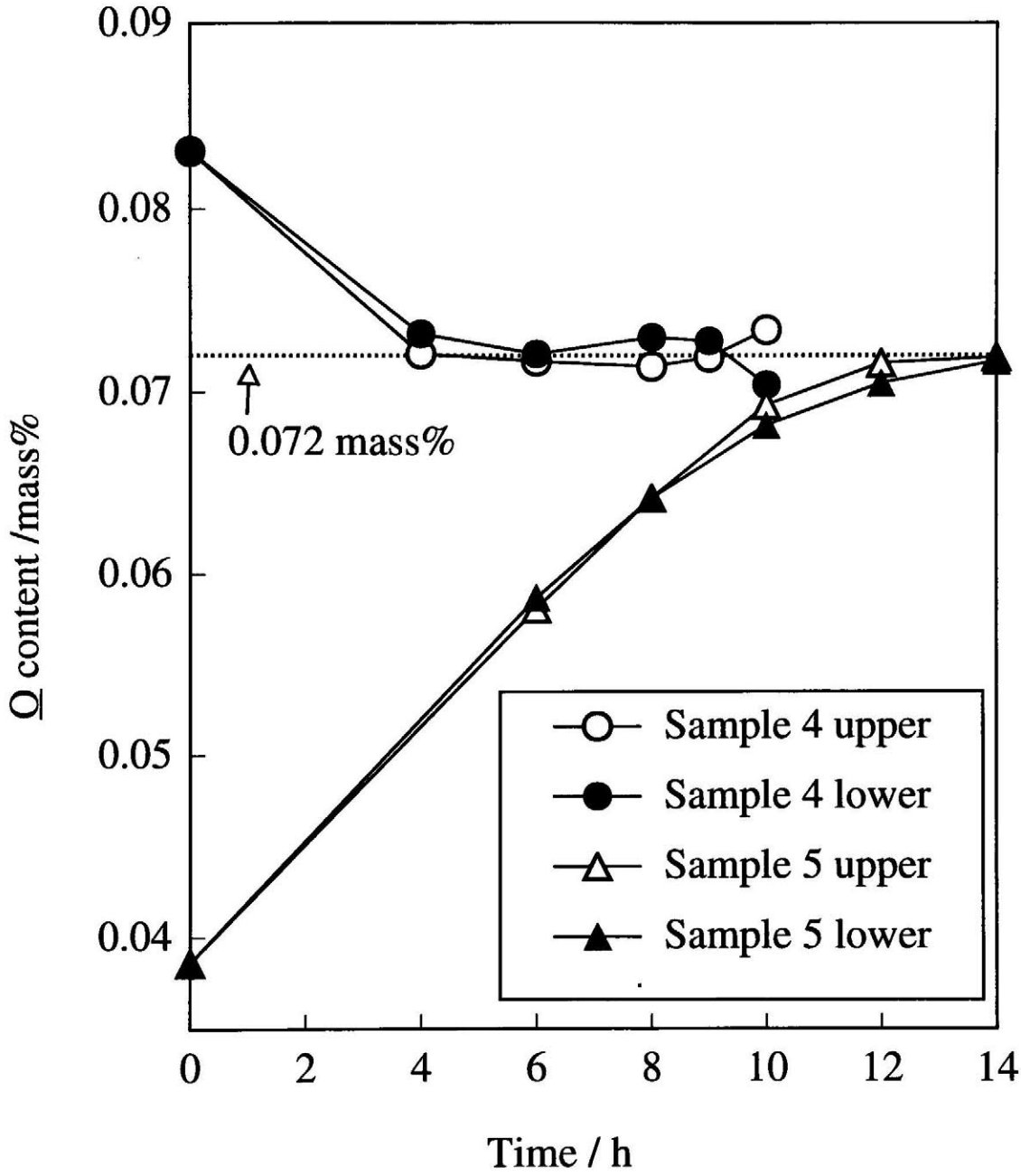

Fig. 3.5 Change in oxygen content for Samples 4 and 5 with respect to holding time at 1873K.

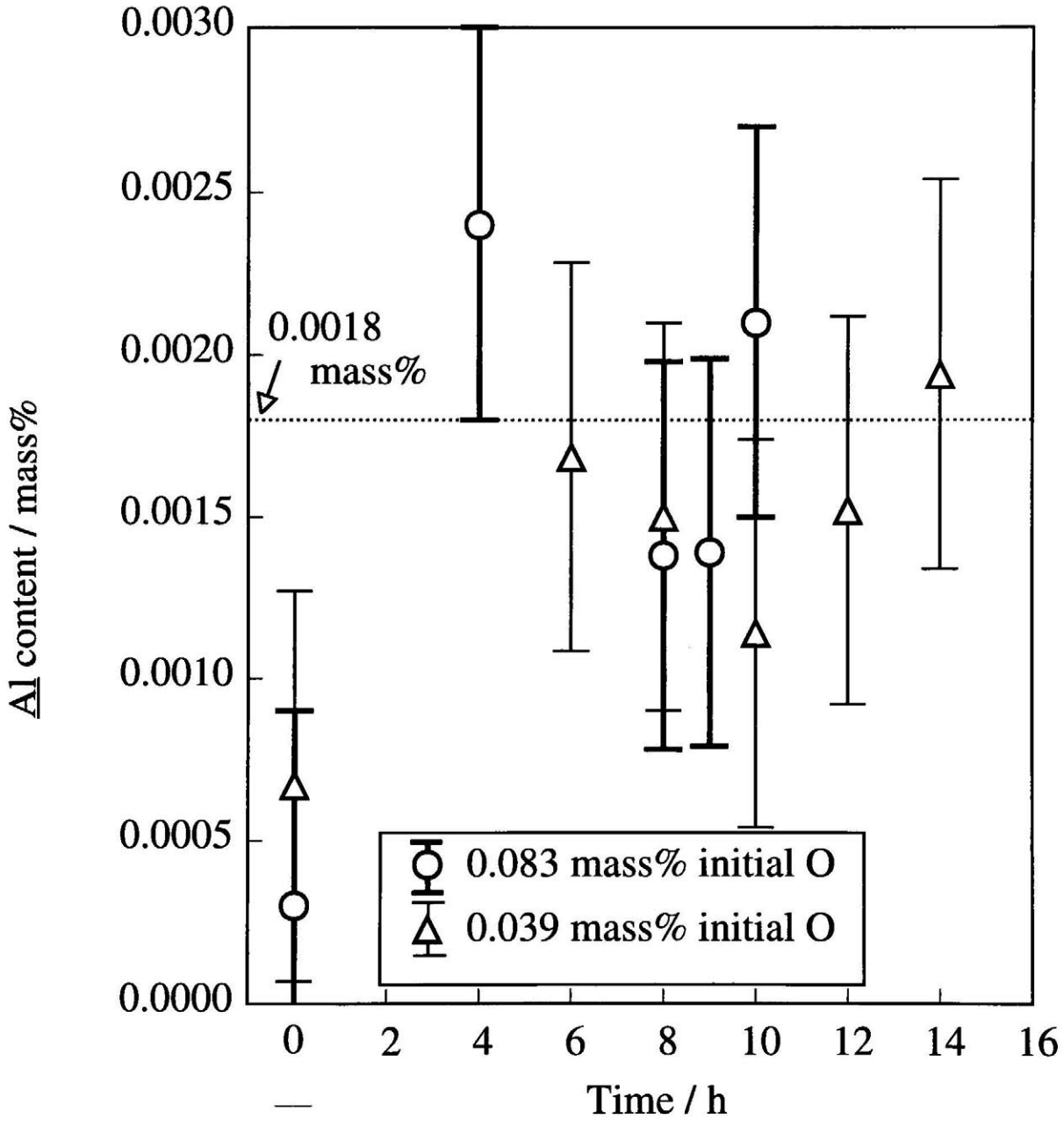

Fig. 3.6 Change in aluminum content for Samples 4 and 5 with respect to holding time at 1873K.

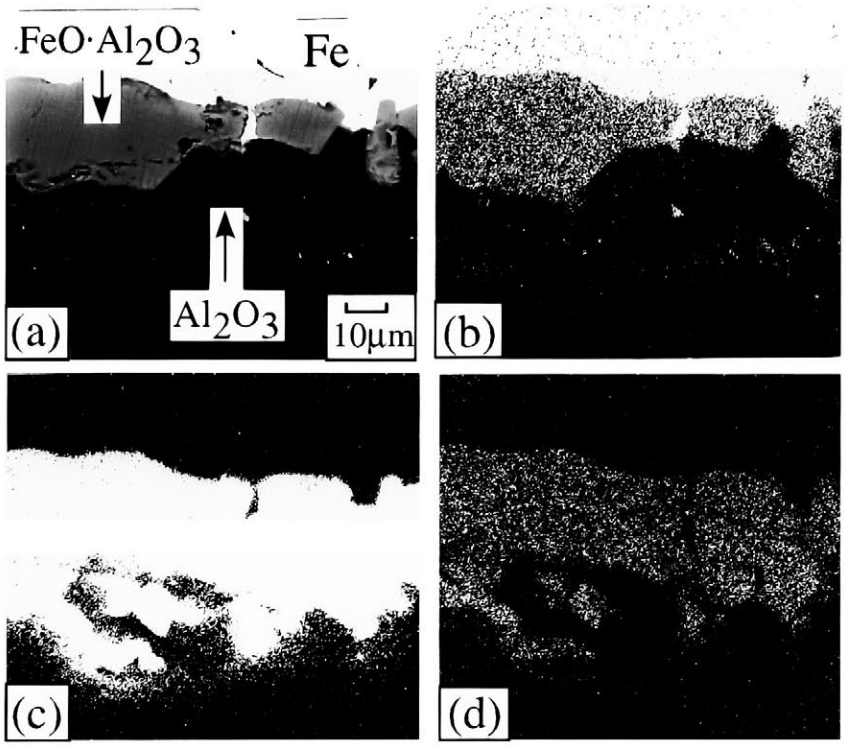

Fig. 3.7 EPMA image of $FeO \cdot Al_2O_3$ and Al_2O_3 attaching to the solidified Fe of Sample 4 holding 8 hours at 1873K. Composition image: (a) X-ray image, (b) Fe, (c) Al, (d) O

Table 3.I. O and Al contents in liquid Fe in equilibrium with Al_2O_3 and $FeO{\cdot}Al_2O_3$ as reported in various studies.

Study	O content (mass%)	Al content (mass%)	a_{Al} (henrian, mass%)
Kim and McLean[2)]	7.4×10^{-2}	(1.1×10^{-5}*)	(8.2×10^{-6}*)
Pillay, D'entremont and Chipman[3)]	7.9×10^{-2}	($<5\times10^{-4}$ at 1973K)	(7.5×10^{-6}*)
McLean and Ward[4)]	6.23×10^{-2}	(1.4×10^{-5}*)	(1.1×10^{-5}*)
Novokhatskiy and Belov[5)]	5.74×10^{-2}	7.0×10^{-3}	(1.2×10^{-5}*)
Chan,Alcock and Jacob[6)]	7.5×10^{-2} (calculated value)	1.7×10^{-5} (calculated value)	
Phelke and Elliott[7)]	($>7\times10^{-2}$)		
Hilty and Crafts[9)]	(8×10^{-2})	(2.0×10^{-3})	
Wasai and Mukai[11)]	7.4×10^{-2}	6.0×10^{-3}	6.5×10^{-6}
Present work	7.2×10^{-2}	1.8×10^{-3}	

* indicates values calculated in the present study.

Chapter 4 Thermodynamic Investigation on Nucleation and Supersaturation for the Aluminum-deoxidation Reaction in Liquid Iron.

I. Introduction

Deoxidation of liquid iron to a level such that the oxygen contained in the liquid iron is in equilibrium with the solid α-alumina is generally difficult. Thus, the oxygen content in the iron often exceeds the equilibrium level. The excess oxygen which exceeds the equilibrium value with solid α-alumina is hereafter referred to as excess oxygen. Although reports concerning excess oxygen have been published[1-6], a persuasive explanation for the presence of excess oxygen beyond the equilibrium value has not yet been reported. Suito et al.[1] recently reported that the low oxygen content (0.002-0.004 mass %) in Fe-0.0001-33 mass % Al before melting was found to persist long after melting, although the oxygen content in the liquid iron could be lowered to the equilibrium value after repeated stirring when the oxygen content was high (≒ 0.1 mass %) before the addition of Fe-Al deoxidizer. Suito et al.[1] considered that this excess oxygen should be in the supersaturated state. Li and Suito [2] reported that the logarithm of the critical degree of supersaturation ($\log S°$) is 3.5. The parameter $S°$ shows a maximum degree of supersaturation (S), over which nucleation occurs. Repetylo et al.[3] observed the change in aluminum and oxygen contents with time after the addition of aluminum to liquid iron, which was maintained at 1873 K in an induction furnace under a deoxidized argon atmosphere. The aluminum and oxygen contents in liquid iron which has an initial oxygen content between 0.01 and 0.055 mass % and a concentration product (=[mass % Al]^2[mass % O]^3) of approximately 3×10^{-9}, decreased. The

concentration product approached the equilibrium value (10^{-14}) with time; however, the equilibrium value was never reached, and the final value of approximately 5×10^{-13} and an oxygen content of between 0.002 and 0.006 mass % was obtained. Repetylo et al.[3] concluded that the residual oxygen and aluminum should be present in liquid iron as a fine alumina suspension, the upward movement of which might be very slow. Similarly, Rode et al.[4] reported that the excess oxygen is attributable to the suspension of an alumina deoxidation product, and showed that covering liquid iron with $CaO\text{-}Al_2O_3$ slag and the bubbling of argon gas in liquid iron were effective methods of eliminating the suspension.

Previously, liquid iron in equilibrium with solid α-alumina was analyzed[7] based on an associated solution model. The results of this analysis showed that not only the thermodynamic properties, but also inconsistencies between measurements performed in various studies, could all be explained reasonably using this model. Considering the applicability of this model to the liquid iron and solid α-alumina system, the excess oxygen might also be explained using this model, if the alumina-associated compound in this system ($Al_2O_3(a)$*[1]) is in a supersaturated state.

Clarification of the reason for the existence of this excess oxygen and the behavior of nucleus formation during the deoxidation process is important, because this excess oxygen will finally crystallize as alumina inclusions upon cooling.

In the present study, the nucleation process of alumina in liquid iron was investigated using a modified classical homogeneous nucleation theory. The

*[1] (a) indicates the associated compounds.

interfacial free energy between liquid iron and α-alumina, which was indispensable for this simulation, should depend on oxygen content. Furthermore, the Gibbs free-energy change of the parent liquid iron phase should be taken into consideration. Despite the fact that the Gibbs free-energy change of the parent phase is essentially included in the original theory of nucleation[9], this energy term has either been ignored or has been neglected based on the assumption of an adequate supply of parent phase of constant constitution. Only Popel and Kuzin[8] have recently reported a simulation for nucleation of hydrogen bubbles in liquid aluminum which considers the Gibbs free-energy change of the parent aluminum phase.

II. Method of Calculation

A. Free-Energy Change

The Gibbs free-energy change (ΔG) of one mole of liquid Fe-O-Al system, when n_0 nuclei with radius r are formed, is written as follows:

$$\begin{aligned}\Delta G &= \Delta G_S + \Delta G_A + \Delta G_B \\ &= n_0(\Delta g_S + \Delta g_A + \Delta g_B),\end{aligned} \qquad [4.1]$$

where Δg_S ($= \Delta G_S / n_0$) is the interfacial free energy of a nucleus and is equal to $4\pi r^2\sigma_0$, and Δg_A ($= \Delta G_A / n_0$) is the Gibbs free-energy change of the alumina formation reaction ($2\underline{Al}+3\underline{O} \rightarrow Al_2O_3(s)$) of a nucleus, which is expressed as follows using the degree of supersaturation of the initial parent iron phase:

$$\Delta g_A = -mRT\ln\left[\left\{(a_{Al}^{(1)})^2(a_O^{(1)})^3\right\}/\left\{(a_{Al}^{e})^2(a_O^{e})^3\right\}\right] = -mRT\ln S. \qquad [4.2]$$

Where m is equal to $(4/3)\pi r^3 / V_A$ and V_A is the molar volume of alumina. The term ΔG_B ($= n_0\Delta g_B$) is the Gibbs free-energy difference of the parent liquid iron before and after nucleation and is expressed as the following equation.

$$\Delta G_B = RT\{(x_{Al} - 2n_0m)\cdot\ln a_{Al}^{(2)} + (x_O - 3n_0m)\cdot\ln a_O^{(2)} + x_{Fe}\cdot\ln a_{Fe}^{(2)}\}$$

$$-RT\{(x_{Al}-2n_0m)\cdot\ln a_{Al}^{(1)}+(x_O-3n_0m)\cdot\ln a_O^{(1)}+x_{Fe}\cdot\ln a_{Fe}^{(1)}\}. \quad [4.3]$$

Here, a_i is the activity of i, the superscripts (1), (2) and e show the parent iron phase before nucleation, after nucleation and in equilibrium with α-alumina, respectively, and x_i is the initial molar fraction of i. Estimation of the activity was performed by two methods using different solution models . In the first method, a_i was calculated from the associated solution model (Solution Model 1). In the other, a_{Al} and a_O were calculated from the interaction parameters reported by Li and Suito[2] and a_{Fe} was obtained from the Gibbs-Duhem integration of the a_{Al} and a_O (Solution Model 2).*[2]

Solution Model (1) is a model that assumes associated compounds in liquid iron, namely, $FeO{\cdot}Al_2O_3$(a), Al_2O_3(a), Al_2O(a), FeO(a), Fe_3Al(a), FeAl(a) and $FeAl_3$(a). Fe and Al monomers also exist in liquid iron, but the oxygen monomer content is considered to be negligible. Further details concerning this model are described in a previous article[7] and in Chapter 2.

B. Estimation of Interfacial Free Energy between Liquid Iron and Solid α-Alumina

In Fig. 4.1, the interfacial free energy between various metals and alumina or zirconia measured by Nikolopoulos et al.,[10] and those between iron and oxides (hercynite, silica and wüstite) summarized by Mukai et al.[11] are shown after transformation by Eq. [4.4].

$$\sigma^*_{metals-oxide}=\sigma_{metals-oxide}N^{1/3}V_{oxide}{}^{2/3} \quad [4.4]$$

Here, $\sigma_{metals-oxide}$ is the interfacial free energy, V_{oxide} is the molar volume of

*[2]The calculated Fe activities show positive deviation in much of the aluminum and oxygen region concerned in both Solution Models 1 and 2.

oxides and N is Avogadro's number. The data of Nikolopoulos et al.[10] are encircled by a large solid line and are designated respectively as Al_2O_3 and ZrO_2. The data of Mukai et al.[11] are encircled by dotted line and are designated as either $FeO{\cdot}Al_2O_3$, SiO_2 or FeO. The iron data are shown as triangles and the data for other metals are shown as small circles. The abscissa of Fig. 4.1 represents the enthalpy values of oxides (H°_{oxide}) at temperature (T), expressed as

$$H^{\circ}_{\text{oxide}} = \Delta H^{\circ}_{\text{oxide,at298K}} + \int_{298}^{T} Cp_{\text{oxide}}\,dT, \qquad [4.5]$$

where $\Delta H^{\circ}_{\text{oxide,at298K}}$ and Cp_{oxide} are the molar enthalpy of formation at 298K[12] and the molar heat capacity at constant pressure, respectively. Figure 4.1 shows the linear correlation between H°_{oxide} and $\sigma^{*}_{\text{metals-oxide}}$. This correlation suggests that $\sigma^{*}_{\text{metals-oxide}}$ depends largely on the bond energy of oxide. The following linear equation between H°_{oxide} and $\sigma^{*}_{\text{metals-oxide}}$ is obtained by the least squares method.

$$\sigma^{*}_{\text{metals-oxide}} = -6215 + 0.1210(-H^{\circ}_{\text{oxide}}) \quad \text{(J/mol)}. \qquad [4.6]$$

Although no certain method is known for estimating interfacial free energy, Fig. 4.1 shows that estimation is possible using the term H°_{oxide}. The interfacial free energy between liquid iron and α-Alumina at 1873 K is calculated to be 2.364 N/m using Eq. [4.6].

Tenabe and Suito[13] reported that the interfacial free energy between liquid iron and α-alumina decreased with the increase of oxygen in liquid iron. Therefore, considering this dependence on oxygen, the interfacial free energy between liquid iron (0 - 0.025 mass % $\underline{O}$) and α-Alumina is expressed as follows (Fig. 4.2).

$$\sigma = 2.328 - 43.18[\text{mass\%}\underline{O}] - 708.6[\text{mass\%}\underline{O}]^2 \quad \text{(N/m)}. \qquad [4.7]$$

However, this interfacial free energy is that between α-Alumina having zero curvature and liquid iron. The interfacial free energy of a fine nucleus having a large curvature should be smaller than the interfacial free energy of a large bulk phase such as a plane having zero curvature. According to Defay and Prigogine,[9] the surface free energy between gas and liquid is expressed as follows.

$$\sigma_o / \sigma = (1/V_A)/\{(2\Gamma/r) + ((1/V_A)\} \ . \qquad [4.8]$$

Where σ_o is the surface free energy of a liquid droplet with radius of r, σ is the surface free energy when r is infinity (zero curvature) and Γ is the surface excess. Eqation [4.8] is applicable only to liquid droplets surrounded by the gas phase. However, the relationship between gas and liquid droplets is similar to that between liquid iron and solid alumina inclusions because the aluminum and oxygen contents in liquid iron are very low and the bond energy of α-alumina is considerably larger than that of liquid iron. Therefore, Eq. [4.8] was used in the estimation of the interfacial free energy between liquid iron and α-alumina nucleus, where Γ was assumed to be $\Gamma = N^{-1/3} V_A^{-2/3}$.

Figure 4.3 shows the dependence of σ_o for the oxygen-free iron on r. As r decreases, σ_o decreases. However, when a nucleus is constituted of only a few molecules, the significance of σ_o, shown in Fig. 4.3 is uncertain. However in the present study, σ_o obtained from Eq. [4.8] was used for the entire range of r. This will be discussed in Section IV-B.

III. Results of Calculation

A. Degree of Supersaturation

In Table 4.I, the degree of supersaturation was calculated using two solution models for the iron solutions which have initial oxygen contents of 0.025, 0.02,

0.01 and 0.005 mass % and initial aluminum contents of 0.1 and 0.01 mass %. Large differences are observed between the values calculated using these two models; however, both of the obtained values show a tendency to decrease with the decrease of aluminum and oxygen contents*[3]. Therefore, in general, less nucleation occurs for low contents of aluminum and oxygen.

B. Change in ΔG Curve with Respect to r and Oxygen Content

Figures 4.4-(a) and 4.4-(b) show the dependence of the Gibbs free-energy change on $\log r$ calculated by Solution Model 1 for iron solutions initially containing 0.02, 0.01 and 0.005 mass % O, respectively. Figure 4.4-(a) is the case of 0.1 mass % initial aluminum, and Fig. 4.4-(b) is the case of 0.01 mass % initial aluminum. Figure 4.4-(a) includes an insert figure which has a magnified vertical axis. The curves of the Gibbs free-energy change start from the first stage of nucleation and end just before the equilibrium with alumina. In this calculation, n_0 is assumed to be 10^{16}. Figure 4.4-(a) shows that ΔG at 0.02 mass % initial oxygen is negative with respect to r, except in the small radius region, whereas ΔG at 0.005 mass % initial oxygen is positive. This result indicates that nucleation does not occur at 0.005 mass % O. At 0.01 and 0.02 mass % O, ΔG shows a minimum near $\log r$= -8.4 and -8.3, respectively, which suggests the end of nucleation. The maximum ΔG for 0.01 mass % O is one order of magnitude larger than that for 0.02 mass % O, which suggests difficulty in nucleation. For 0.01 mass % initial aluminum, Fig. 4.4-(b) shows that the Gibbs free energy is positive over the entire range of the nuclear radius.

*[3]The degree of supersaturation for 0.01 mass % Al calculated by Solution Model 1 does not decrease with the decrease of oxygen because the aluminum and oxygen activities in this region are influenced by the concave equilibrium curve which will be disscussed in Section IV-D.

Therefore, nucleation is difficult at 0.01 mass % initial aluminum. In contrast, the results calculated using Solution Model 2 for 0.1 mass % initial aluminum (Fig. 4.5-(a)) and 0.01 mass % initial aluminum (Fig. 4.5-(b)) show a negative ΔG, except in the small radius region. Furthermore, the minima shown in Fig. 4.5-(a) and 4.5-(b) are located just before the equilibrium, and, thus, the energy barriers on the right-hand side of the minima for reaching the equilibrium are not so high as those for Solution Model 1.

C. Change in ΔG_S, ΔG_A and ΔG_B Curves with Respect to r and Oxygen Content

In Fig. 4.6, ΔG_S, ΔG_A and ΔG_B, which are the first, second and third terms of Eq. [4.1] and are calculated using Solution Model 1, are shown with respect to $\log r$ for 0.1 mass % Al and 0.02 mass % O initial contents. Since the oxygen content decreases with the growth of nuclei, ΔG_S is positive and becomes larger as r increases, due not only to the increase of $4\pi r^2$, but also to the increase of σ_o. For a low initial oxygen, $\Delta G_S (= n_0 4\pi r^2 \sigma_o)$ is larger than in the case of a high initial oxygen content because σ_o is larger at a low oxygen content. The value of ΔG_B is positive and increases following nuclei growth. The positiveness of ΔG_B is mainly due to the increase in iron activity that accompanies the decrease in aluminum and oxygen contents. In addition, ΔG_B increases as the initial oxygen content decreases. In contrast, ΔG_A is negative. Since $\Delta g_A / m$ is negative and constant for given initial aluminum and oxygen contents, ΔG_A decreases as m increases. However, ΔG_A is larger in the case of a lower initial oxygen content because S becomes smaller at lower oxygen contents (Eq. [4.2]).

Figure 4.7 (0.1 mass % Al and 0.02 mass % O) shows ΔG_S, ΔG_A and ΔG_B derived using Solution Model 2. The positiveness or negativeness of these

values are similar to those obtained using Solution Model 1; however, ΔG_B is larger and ΔG_A is smaller because the degree of supersaturation is larger in this case (Table 4.I).

D. Change in $\Delta G/n_0$, Δg_S, Δg_A and Δg_B Curves with Respect to n_0

For various n_0 values,(n_0=10^{16},10^{17},10^{18})· $\Delta G/n_0$, obtained using Solution Model 1, is shown in Fig. 4.8 (0.1 mass % Al, 0.02 mass % O). Figure 4.8 includes an insert figure which has a magnified vertical axis. The values of Δg_A with respect to r for n_0=10^{16}, 10^{17} and 10^{18} are the same, because $\Delta g_A / m$ is constant for given initial aluminum and oxygen contents. For constant r value, Δg_S and Δg_B for high n_0 values are larger than those for low n_0 values, because the aluminum and oxygen contents become lower as the result of the increase of n_0. Yet in the small-radius region and for the n_0 values lower than 10^{17}, the values of Δg_S at different n_0 values virtually coincide with each other, and those of Δg_B are almost zero. Thus, in the small-radius region, the $\Delta G/n_0$ curve is determined by the almost-constant curve of Δg_S and Δg_A. Therefore, as shown in Fig. 4.8, the maxima of $\Delta G/n_0$ for 10^{17} and 10^{16} and lower values of n_0 lie at nearly the same position, are almost constant and do not depend largely on n_0. In contrast, the minimum of $\Delta G/n_0$ moves to the lower-radius side as n_0 increases. In addition, the $\Delta G/n_0$ curve becomes shorter, namely, the parent liquid iron reaches equilibrium at an early stage when the radius is small. The increase of n_0 finally results in a positive $\Delta G/n_0$ value showing no maximum nor minimum, because Δg_A has less effect on $\Delta G/n_0$, in the small-radius region. The tendencies of $\Delta G/n_0$ for various n_0 values calculated using Solution Model 1 are similar to those of Solution Model 2. However, the behaviors of the minima are different. Although the minima shown in Figs. 4.5-(a) and 4.5-(b) are not distinct and located just before the equilibrium,

$\Delta G/n_0$ for a larger n_0 shows a distinct minimum in the smaller-radius region.

The flow diagram of the calculations is shown in Fig. 4.9.

IV. Discussion

A. Critical Free Energy of Nucleation and Rate of Nucleation

Nucleation does not occur over the large $\Delta G/n_0$ maximum, but instead proceeds through the maximum of the moderate positive value. Regarding the maximum as a critical Gibbs free energy ($\Delta G^*/n_0$) and its radius as a critical radius (r^*), the rate of nucleation can be evaluated from Eqs. [4.9] and [4.10], which was derived by Turnbull and Ficher[14] and Hollomon and Turnbull[15] for the spherical nucleus.

$$I = A\exp\{-(\Delta G^*/n_0 + \Delta G_D)/kT\}, \qquad [4.9]$$

$$A = n^*(\sigma_o/kT)^{1/2}(2v/9\pi)^{1/3}n(kT/h), \qquad [4.10]$$

where ΔG_D is the Gibbs free energy of activation for transporting a molecule across the interface, n^* is the number of molecules on the surface of critical nuclei, and n is the number of molecules per mole of parent phase. In the present study, n is assumed to be one-third of the oxygen atoms in the parent phase, because an alumina molecule is constituted of three oxygen atoms. The v in Eq. [4.10] is the volume per molecule of the critical nucleus. Although v is described as the volume per molecule of the parent phase in the report by Turnbull and Ficher,[14] investigation of their report revealed this to be incorrect. In Eq. [4.9], ΔG_D is neglected because this term is unknown and is thought to be very small in comparison to $\Delta G^*/n_0$. In Eqs. [4.9] and [4.10], the n^*, n and v values are as follows:

$$n^* = 4\pi(r^*)^2/\{M/(\rho N)\}^{2/3}, \qquad [4.11]$$

$$n = N x_O / 3, \qquad [4.12]$$

$$v = (M/\rho)/N. \qquad [4.13]$$

Where M is the molecular weight of alumina, h is the Planck's constant, T is the temperature and ρ is the density of alumina (=3.987x10^{6}g·m^{-3}).

The calculated rate of nucleation does not depend largely on n_0 and is of almost constant order if $\Delta G/n_0$ has a maximum, due to the nearly equal value of the $\Delta G/n_0$ maximum even for different n_0 values. In Table 4.II, nucleation rates are shown along with the critical radius. The results of Solution Model 1 in Table 4.II at 0.1 mass % Al for liquid iron having 0.02 or 0.025 mass % O show that the rates of nucleation are large. However, those for 0.01 and 0.005 mass % O are almost zero. This is revealed in Fig. 4.4-(a), which shows the positive value of ΔG at 0.005 mass % O and a large maximum at 0.01 mass % O, which is in contrast to the small maximum at 0.02 mass % O. In addition, at 0.01 mass % Al, iron solutions at 0.02, 0.01 and 0.005 mass % O do not nucleate at all. This nucleation tendency is the same as that explained for the case of n_0=10^{16} in Section III-B. The results for Solution Model 2, listed in Table 4.II, are also the same as those described in Section III-B. However, the results for Solution Model 2 show that the critical radius of the nuclei is very small.

B. Validity of the Interfacial Free Energy

Figure 4.10 shows the comparison of the interfacial free-energy changes (σ and σ_o) during the nucleation process (n_0=10^{16}) for the 0.1 mass % Al and 0.02 mass % O initial solution derived from Eqs. [4.7] and [4.8], respectively. Although σ_o approaches zero at the radius below 10 Å, σ is roughly constant. Eqation [4.8] was derived thermodynamically and theoretically for the fine particle with a large curvature of interface; however, the validity of this equation

is unclear for nuclei constituted of a few molecules that have radii of less than 10 Å (log r <-9) because the thermodynamic properties of these small particles are quite different from those of the bulk phase. In contrast, σ is the interfacial free energy for the bulk alumina with a curvature of interface of zero. The actual interfacial free energy is smaller than σ. Therefore, σ gives the border (or maximum) value which the interfacial free energy does not exceed. For comparison, the rate of nucleation was calculated using σ as the interfacial free energy of nucleus, and the results are shown in Table 4.III. The results from both Solution Models 1 and 2 show that the nucleation becomes more difficult in this case. In addition, the rates of nucleation for 0.1 mass % Al at different oxygen contents calculated from Solution Model 2 using σ, shown in Table 4.III are similar to those calculated from Solution Model 1 for 0.1 mass % Al shown in Table 4.II. Thus, both rates of nucleation calculated from different interfacial free energies indicate the easy nucleation at a high oxygen content and no nucleation at a low oxygen content, which agrees well with the results obtained by Suito et al.[3] Namely, comparison of Tables 4.II and 4.III reveals that both interfacial free energies may be adequate for explaining the actual nucleation tendency. Therefore, the actual interfacial free energy in the small-radius region remains unclear; however, the reasons for the excess oxygen are clarified, as explained in Section IV-C.

The flow diagram of the calculations in Sections IV-A and IV-B is shown in Fig. 4.9.

C. Reason for the Excess Oxygen

At 0.1 mass % Al, the rate of nucleation for the iron of 0.02 mass % O in Solution Model 1, shown in Table 4.II, is on the order of 10^{29}, but nucleation does not occur for the iron of 0.01 or 0.005 mass % O. These results indicate

that, in the actual process at high oxygen content, a large number of embryos form at the earliest stage of nucleation, some of which must decompose, because, under the large-n_0 condition, $\Delta G/n_0$ is positive over the entire range of the radius. A large number of these embryos collide with each other and coalescence occurs. As a result, n_0 decreases. Moreover, $\Delta G/n_0$ decreases as n_0 decreases and the embryos grow to nuclei, passing over the moderate value of the maximum of $\Delta G/n_0$. After this, the nuclei may reach the positive minimum of $\Delta G/n_0$, causing the growth of the nuclei to stop. Since this is an unstable state and n_0 is still large, some part of the nuclei may decompose; however, collision and coalescence would further promote the decrease of n_0 and $\Delta G/n_0$ and, consequently, the growth of the nucleus. In addition, stirring would accelerate this collision. Even at the negative minimum, if n_0 is large, collision and coalescence would occur due to stirring. If $\Delta G/n_0$ reaches a low negative minimum for a small n_0 value, the cessation of nucleation might persist for a long time, because the nucleus is difficult to grow or decompose over either side of the high energy barrier. Moreover, the probability of collision is low and the nuclear sizes are not yet large enough to float upward. The nuclei remain suspended in liquid iron for an extended period of time. Repeated stirring and adequate time is required for regrowth and floating upward. Therefore, the suspension of this small alumina is a likely cause of excess oxygen in this system. However, the residual aluminum and oxygen (or associated compounds) in liquid iron after the nuclei reach the Gibbs free-energy minimum are in the supersaturated state. Furthermore, in the case of a low initial oxygen content, since the energy barrier (Gibbs free-energy maximum) is high and no nucleation occurs (Tables 4.II and 4.III), the aluminum and oxygen (or associated compounds) continue to remain in the

liquid iron at the state of supersaturation. These supersaturations are thought to be another reason for the presence of excess oxygen.

The previous explanation takes into account the total Gibbs free energy of the nuclei plus the parent liquid iron; therefore, if the nuclei leave the system due to floating, adherence to the wall, etc., calculation of the Gibbs free-energy change should exclude these nuclei. However, in the present calculation the outflow of these nuclei is not taken into consideration because the nuclei are too small to float upward. The nucleation tendency described previously agrees well with the results obtained in research performed by Suito et al.,[1] Repetyro et al.[3] and Rohde et al.[4]

The lower limit of initial oxygen content, below which nucleation does not occur, i.e., the critical point of nucleation (C_O^{cr}), was calculated using Eq. [4.9] and Solution Model 1 using σ_o. The result is plotted in Fig. 4.11 as a solid curve. The C_O^{cr} value calculated by Solution Model 2 using σ is shown as a long-dashed curve. Figure 4.11 also includes the data for excess oxygen as measured by Hilty and Crafts,[16] Schenck et al.,[5] Novokhatski and Belov,[17] Röde et al.[4] and Suito et al.[1] Although the aforementioned two curves of C_O^{cr} are different for each solution model and interfacial free energy used, both curves look roughly similar to the upper bound for all of these data, except for some of the data of Novokhatski and Belov[17] and Hilty and Crafts[16] at the lower aluminum region. The curve indicating log S=3.5[2] (dotted curve), calculated using the activities from Solution Model 2, lies slightly below these curves. Although the curve for log S=3.5, shown in Fig. 4.11, was calculated using Solution Model 2, this curve differs somewhat from the C_O^{cr} curve (long-dashed curve) calculated by Solution Model 2 using σ, because the latter was derived using Eq. [4.9], which takes into account not only the degree of

supersaturation, but also the activity of the parent liquid phase and the oxygen dependence of interfacial free energy.

Hilty and Crafts,[16] Schenck et al.[5] and Rode et al.[4] dropped aluminum deoxidizer into liquid iron in the furnace from the opened upper inlet. Therefore, the atmosphere in the furnace may have been contaminated with oxygen. However, since Hilty and Crafts[16] and Schenck et al.[5] performed their experiments using an induction furnace, stirring would have been adequate, and at an aluminum content of greater than 0.1 mass % Al, the experimental data of these two studies indicate lower oxygen contents than do the data of Rode et al.[4], who used a resistance furnace. Thus, in the experiments of Hilty and Crafts[16] and Schenck et al.[5] the nuclei in the liquid iron would have been eliminated largely due to stirring. Although the data presented by Novokhatski and Belov[17] are slightly higher, the furnace used in their experiment is not specified.[17]

D. Comparison of the Results from Solution Models 1 and 2

The reason for the presence of excess oxygen is clarified in the previous simulation and discussion; however, several details of this system, for example, the activities, interfacial free energy, critical point of nucleation, etc., remain unclear. In the previous simulation, two kinds of activities and interfacial free energies were used, and the interfacial free energies were discussed in Section IV-B.

Interaction parameters are commonly used when assessing activities. The interaction parameters are defined for use in an infinitely dilute solution of iron, but the concentration limits for which these parameters are applicable are sometimes vague. In a system in which activities deviate largely in the negative direction, as in the Fe-Al-O system, the interaction parameters may depend on

the concentrations of the components in the system. Suito et al.[1] measured oxygen activity using an oxygen sensor made of solid oxide electrolyte and reported agreement between the measured activity and the activity calculated using interaction parameters and concentrations. However, the reliability of measurements of this system using an oxygen sensor have not yet been established, and further investigation is necessary in order to confirm the validity of their method of measurement.

Although the associated solution model is not accepted by several researchers and the degree of supersaturation calculated using this model is very low, this model may be useful in the present study, considering its remarkable capability for explaining the data for equilibrium with solid α-alumina. The short-dashed curve (equilibrium curve) in Fig. 4.11 shows the aluminum and oxygen concentration for equilibrium with solid α-alumina calculated using the associated solution model. The concave portion of this curve in the low aluminum region is characteristic. The large circle at the end of this short-dashed curve shows the concentration calculated using associated solution model of liquid iron, which is in equilibrium with α-alumina and hercynite simultaneously (coexisting point of three phases). In contrast, the equilibrium curve calculated using interaction parameters and the deoxidation constant is almost linear in the low aluminum region and the coexisting point calculated in a similar manner is in a much more dilute Al concentration region, approximately 10^{-5} mass % Al, on the linear equilibrium curve. The experimental determination of this coexisting point in equilibrium with α-alumina and hercynite is important in order to determine which model is more appropriate for this system. Therefore, oxygen and aluminum contents at the coexisting point at 1873K were determined by the present author, which was

reported previously[18] and in Chap. 3. The obtained contents at this point are 0.072 mass%O and 0.0018 mass%Al. Thus, the equilibrium curve., on which liquid Fe is in equilibrium with α-Al_2O_3, is not a straight line, but rather is a concave curve. Therefore, it was proved that Solution Model 2 are not appropriate in the high O region for the calculation of activities, and, in contrast, Solution Model 1 should be appropriate.

V. Conclusions

A new and effective way of estimating the interfacial free energy between liquid metal and oxides was proposed (Fig. 4.1 and Eq. [4.6]). In addition, a new way for investigating the alumina nucleation process in liquid iron was developed, which considers the Gibbs free-energy change of parent liquid iron and the dependence of the interfacial free energy between liquid iron and α-alumina on oxygen content. This method was used to clarify the controversial problem concerning the excess oxygen in liquid iron over the equilibrium value.

The supersaturation or the suspension of small alumina inclusions, which are the two main reasons for excess oxygen as reported by various researchers, both occur in the alumina nucleation process. The present calculations clarified that the curve of the Gibbs free energy of one nucleus with respect to nuclear radius showed a maximum and a minimum. Nucleation was found to occur rapidly when the maximum is not excessively high. This corresponds to the case in which the initial oxygen content is sufficiently higher than the critical point of nucleation. At the Gibbs free-energy minimum, the growth of the nuclei stops, the small alumina nuclei are suspended in the liquid iron, and the excess oxygen remains in the liquid iron at the supersaturated state. Stirring may facilitate the regrowth of the nuclei, because the decrease in the number of nuclei after coalescence leads to the decrease of Gibbs free energy. At the initial oxygen

content under the critical point, nucleation does not occur, and, therefore, supersaturation occurs without causing alumina suspension. The critical point of nucleation was calculated with respect to aluminum content.

The calculations in the present study were performed using two solution models. One model is the associated solution model (Solution Model 1), and the other involved the use of interaction parameters (Solution Model 2). The experiment performed previously proved that Solution model 1 would be appropriate for the calculation of activities in high oxygen region. However, the interfacial free energy used in the models for the very-small-radius region of the nucleus is vague. If the thermodynamics of this system are clarified in the future, determination of the interfacial free energy and an improved solution model may be possible.

References

1. H.Suito, H.Inoue and R.Inoue: ISIJ International 1991, vol. 31, pp. 1381-1388.
2. G.Li and H.Suito: ISIJ International, 1997, vol. 37, pp. 762-769.
3. O.Repetylo, M.Olette and P.Kozakevitch: J Metals, 1967, vol. 19, pp. 45-49.
4. L.E.Rohde, A.Choudhury and M.Wahlster: Arch Eisenhüttenwes., 1971, vol. 42, pp. 165-174.
5. H.Schenck, E.Steinmetz and K.K.Mehta: Arch Eisenhüttenwes., 1970, vol. 41, pp. 131-138.
6. G.R.Fitterer: Proc.Am.Inst.Min.Metall., Pet.Eng.Natl.Open Hearth Basic Oxygen Steel Conf., 1976, vol. 59, pp. 212-226.

7. K.Wasai and K.Mukai: J.Japan.Inst.Metals, 1988, vol. 52, pp. 1088-1097.
8. P.S.Popel and S.N.Kuzin: Proceedings of High Temp.Capillar.Int.Conf (HTC-97), Edited by N.Eustathopoulos and N. Sobczak, Foundry Research Inst., Cracow Poland, 1998, pp. 334-338.
9. R.Defay and I.Prigogine: Surface Tension and Adsorption, Translated by D.H.Everett, John Willey & Sons, Inc., New York, 1966, pp. 319-320.
10. P.Nikolopulos, S.Agathapoulos and A.Tsoga: J.Mater.Sci., 1994, vol. 29, pp. 4393-4398.
11. K.Mukai, H.Sakao and K.Sano: Transactions ISIJ, 1969, vol. 9, pp. 196-202.
12. M.W.Chase Jr., J.L.Curnutt, R.A.McDonald and A.N.Syverud: JANAF Thermochemical Tables, 1978 Supplement, J.Phys.Ref.Data, 1978, vol. 7, pp. 836-840.
13. J.Tanabe and H.Suito: Steel Res., 1955, vol. 66, pp. 146-153.
14. D.Turnbull and J.C.Fisher: J.Chem.Phys., 1949, vol. 17, pp. 71-73.
15. J.H.Hollomon and D.Turnbull: Progr.in Met.Phys., 1953, vol. 4, pp. 342-343.
16. D.C.Hilty and W.Crafts: J Metals, Trns. AIME, 1950, vol. 188, pp. 414-424.
17. I.A.Novokhatskiy and B.F.Belov: Izv.Akad.Nauk SSSR, 1969, (3), pp. 15-26.
18. K.Wasai,K.Mukai,H.Fuchiwaki and A.Yoshida: ISIJ International, 1999, vol. 39, pp.760-766.

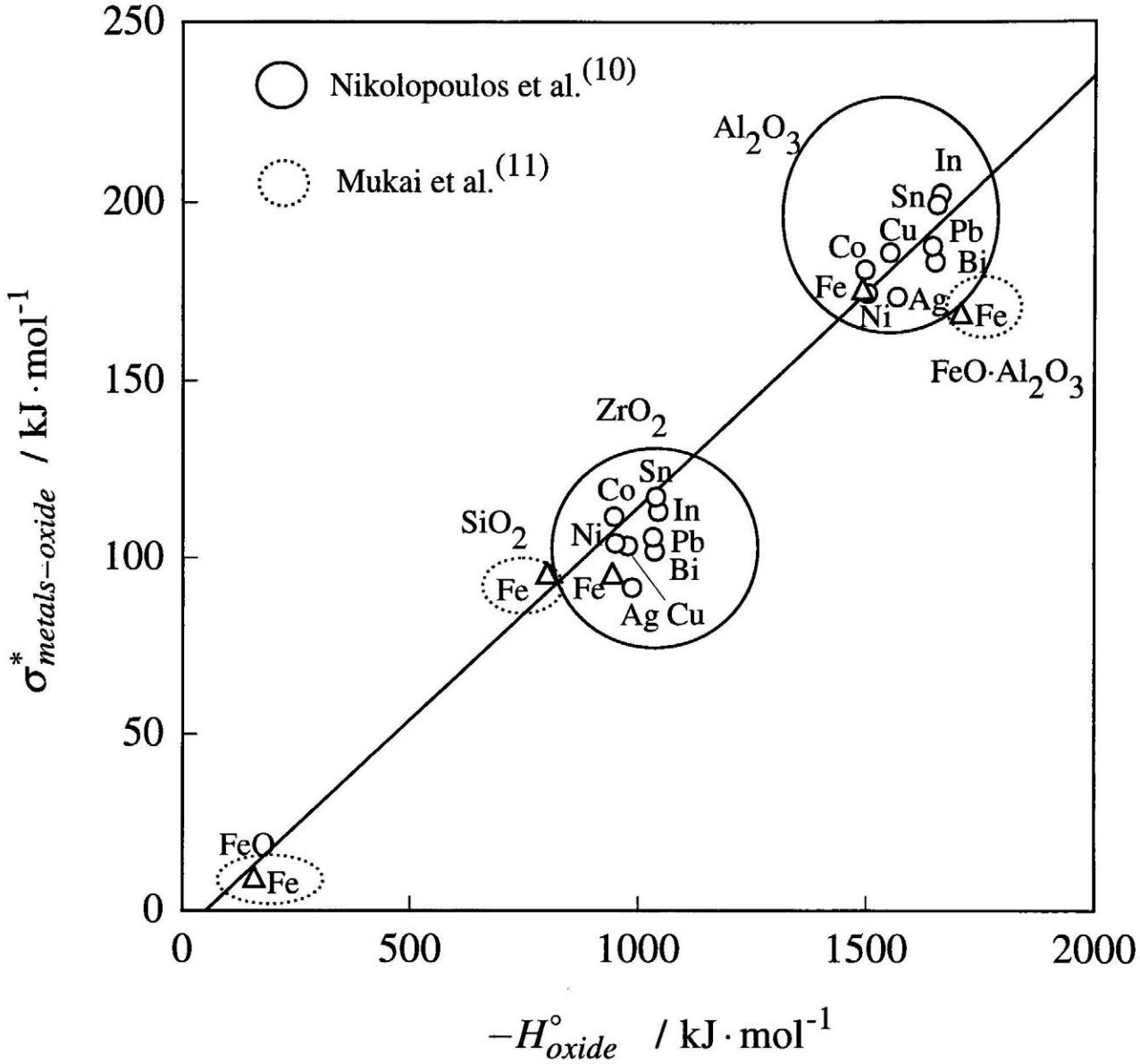

Fig. 4.1 Interfacial free energies between various metals and oxides.

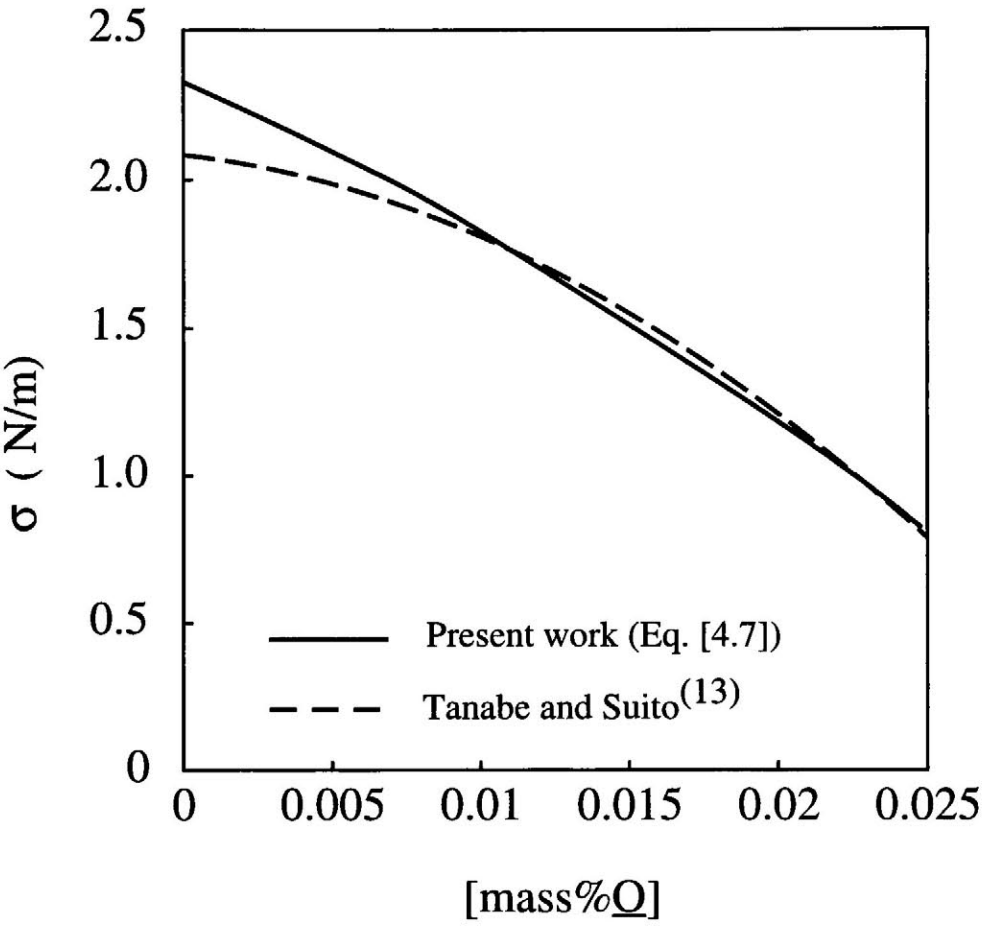

Fig. 4.2 Dependence of the interfacial free energy between liquid iron and α-alumina on oxygen content.

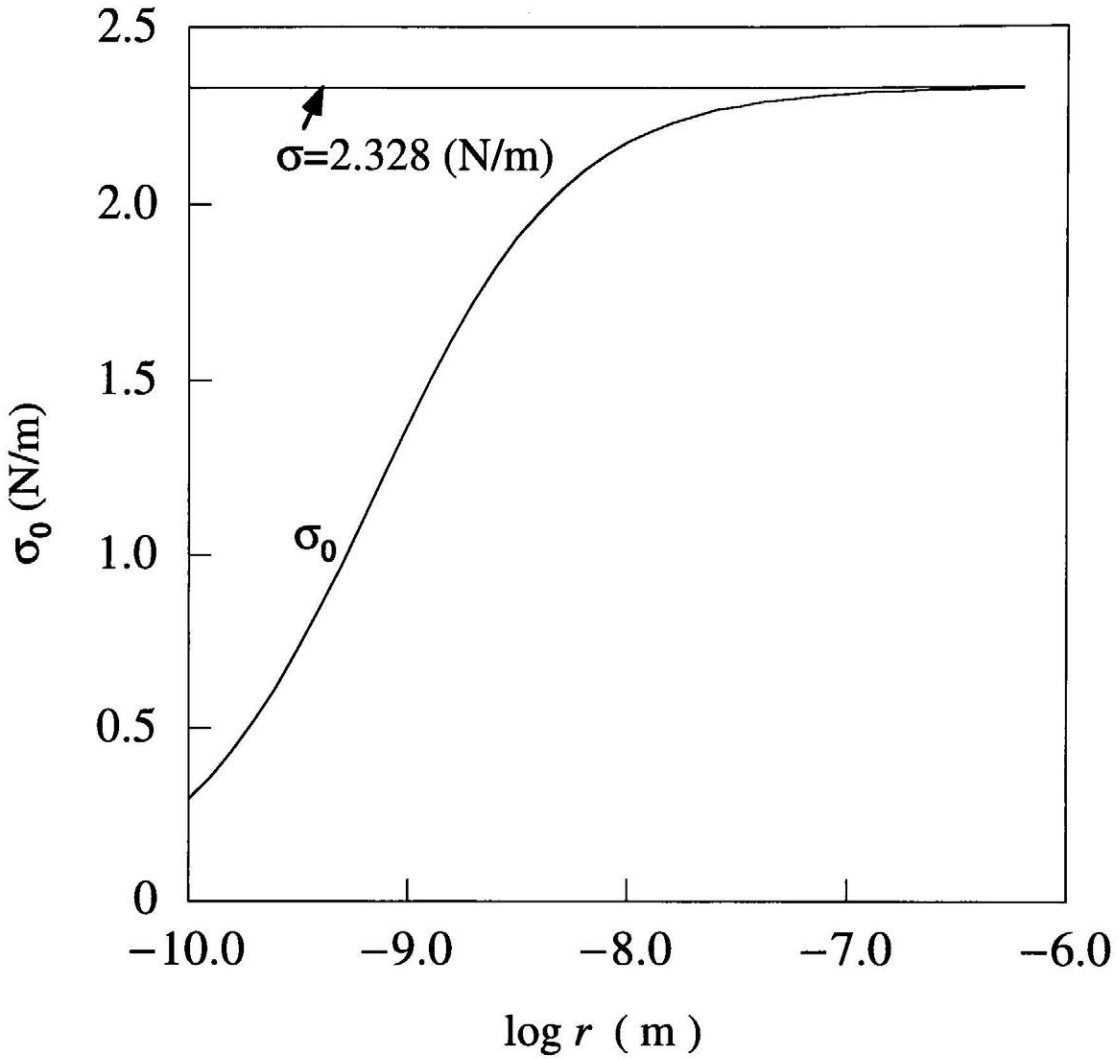

Fig. 4.3 Interfacial free energies between oxygen-free liquid iron and α-alumina having a large curvature (σ_0 from Equation [4.8]) and that having zero curvature (σ=2.328 N/m).

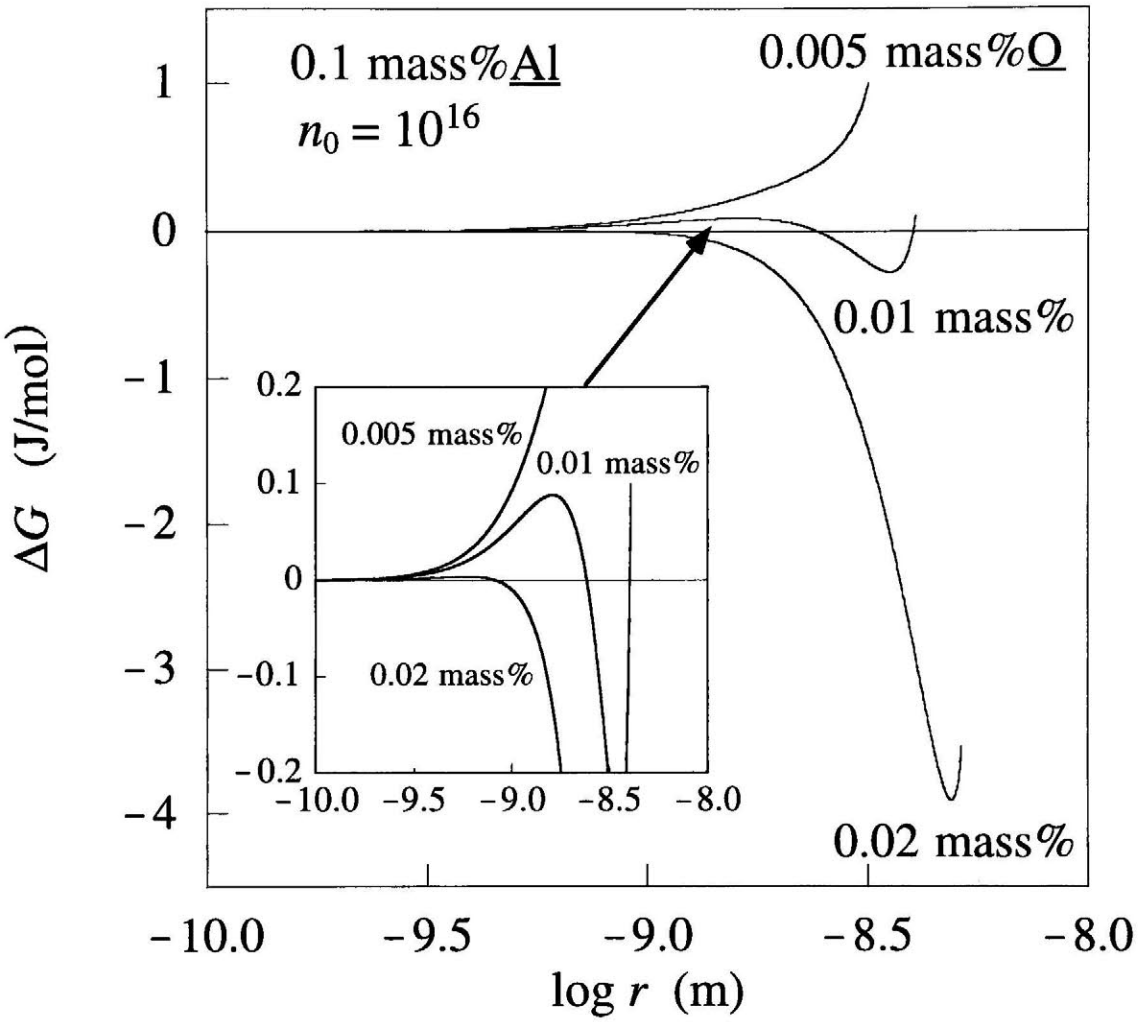

Fig. 4.4-(a) Gibbs free energy change for various initial oxygen contents (0.02, 0.01 and 0.005 mass%O) and 0.1 mass%Al calculated using the activity values from Solution Model 1.

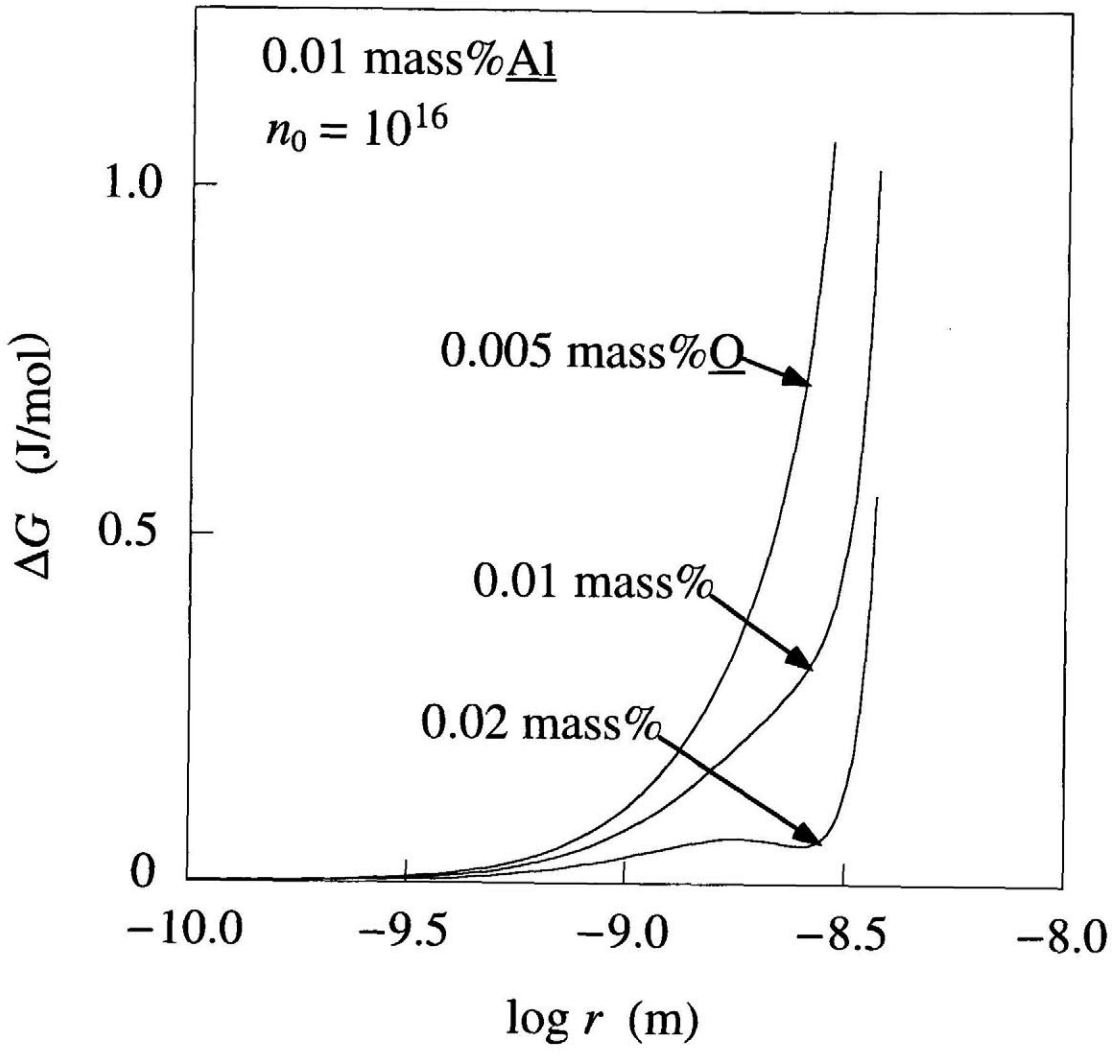

Fig. 4.4-(b) Gibbs free energy change for various initial oxygen contents (0.02, 0.01 and 0.005 mass%O) and 0.01 mass%Al calculated using the activity values from Solution Model 1.

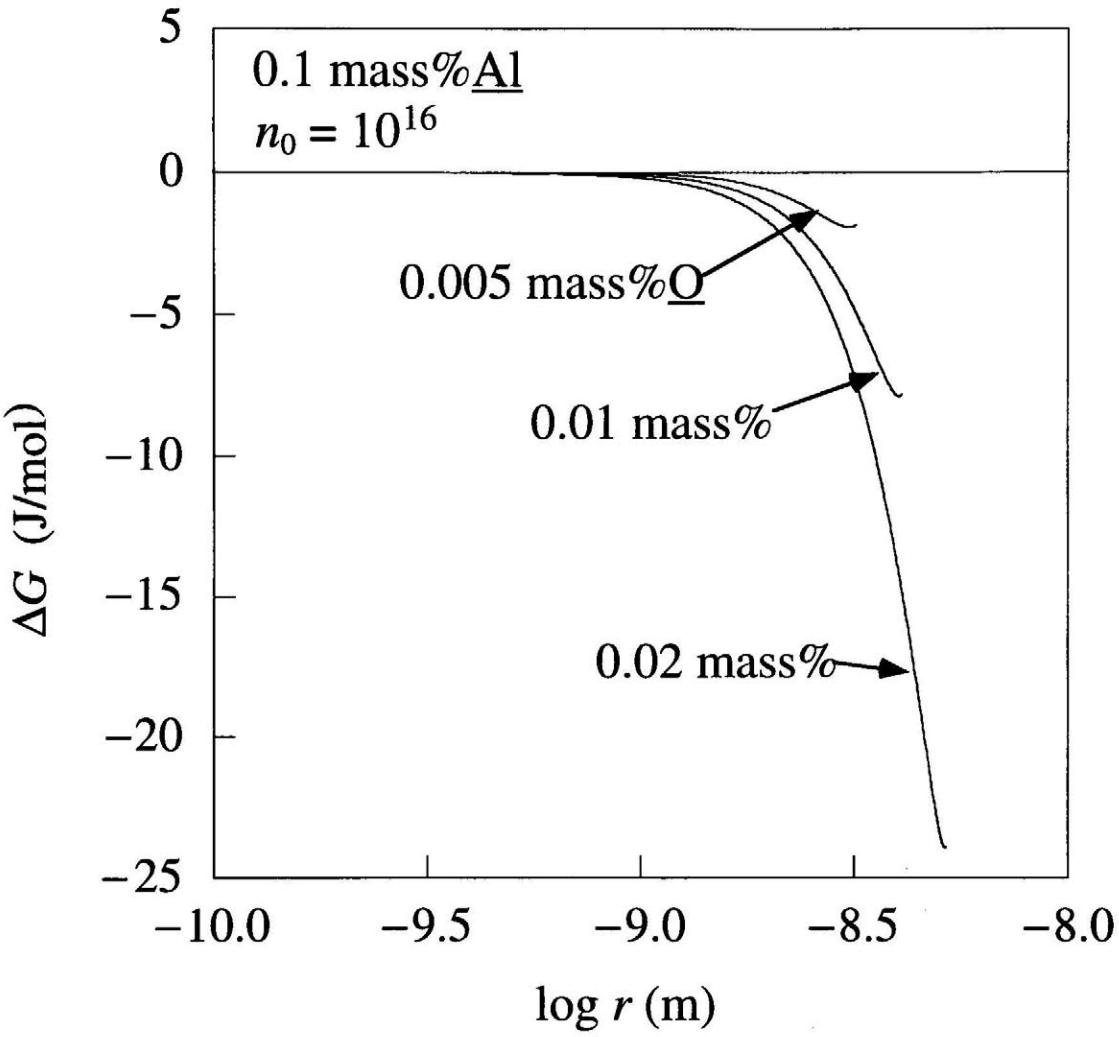

Fig. 4.5-(a) Gibbs free energy change for various initial oxygen contents (0.02, 0.01 and 0.005 mass%O) and 0.1 mass%Al calculated using the activity values from Solution Model 2.

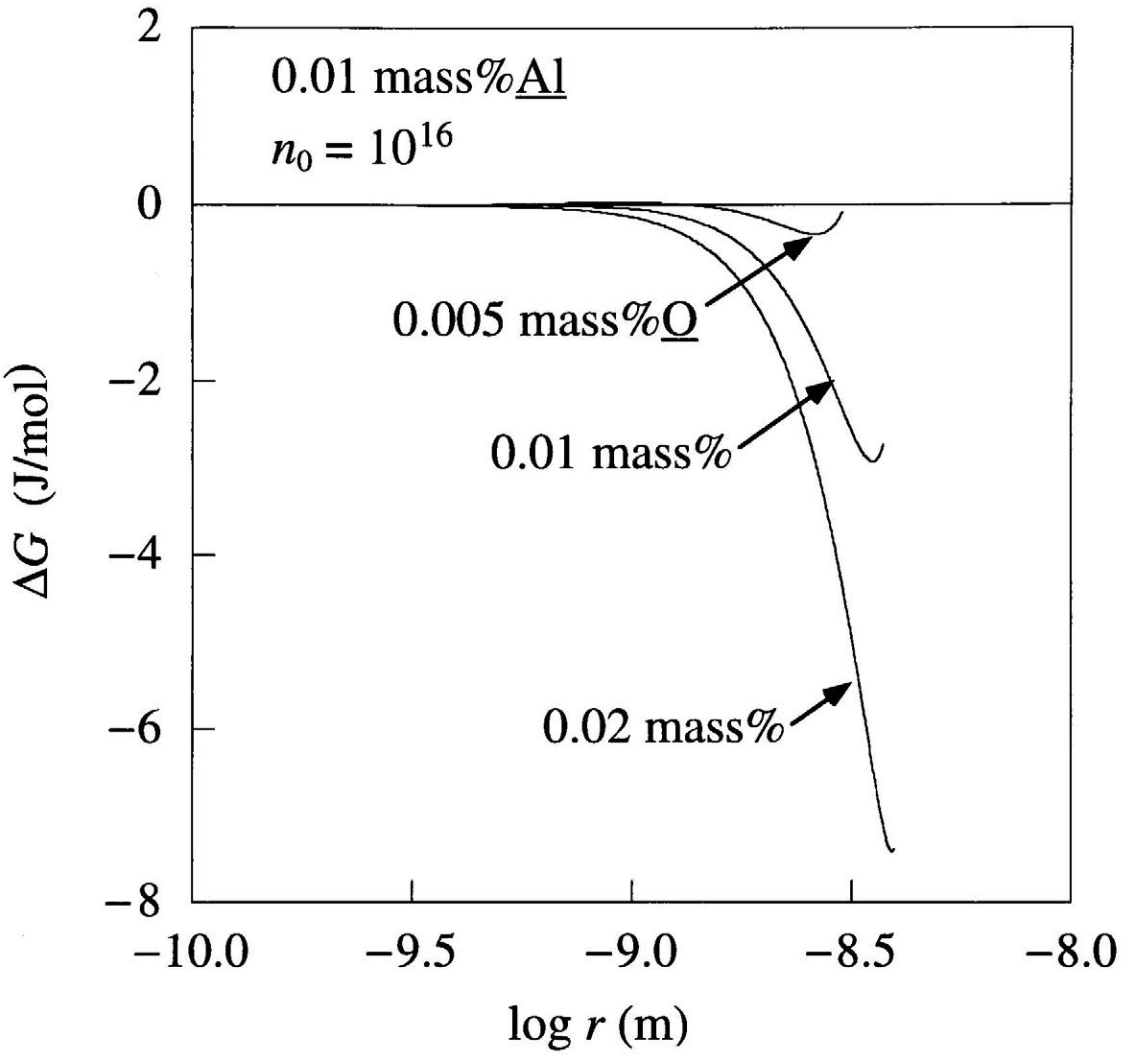

Fig. 4.5-(b) Gibbs free energy change for various initial oxygen contents (0.02, 0.01 and 0.005 mass%O) and 0.01 mass%Al calculated using the activity values from Solution Model 2.

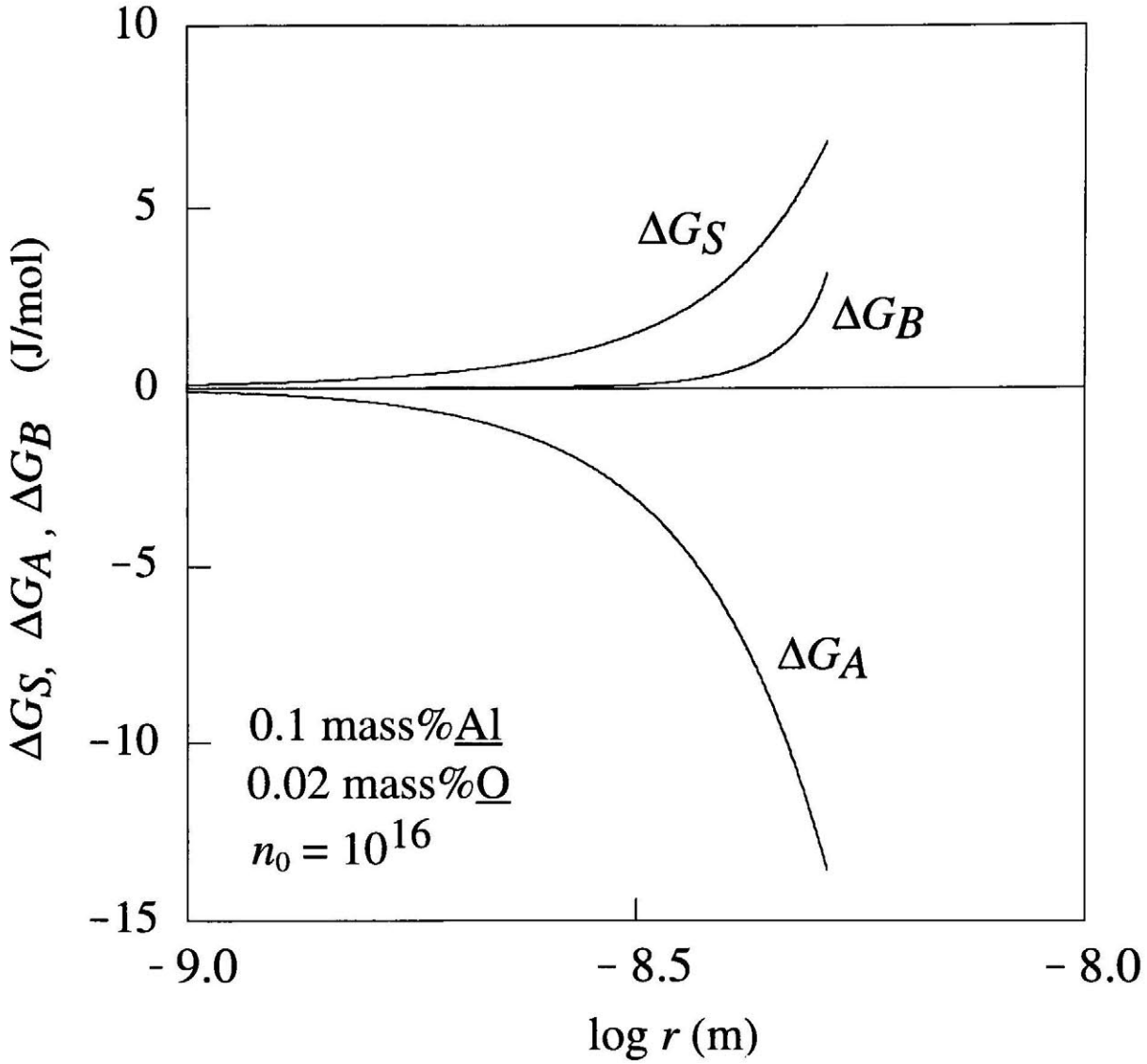

Fig. 4.6 The ΔG_S, ΔG_A and ΔG_B in Equation [4.1] for liquid iron having initial oxygen and aluminum contents of 0.02 mass% and 0.1 mass%, respectively, calculated using the activity values from Solution Model 1.

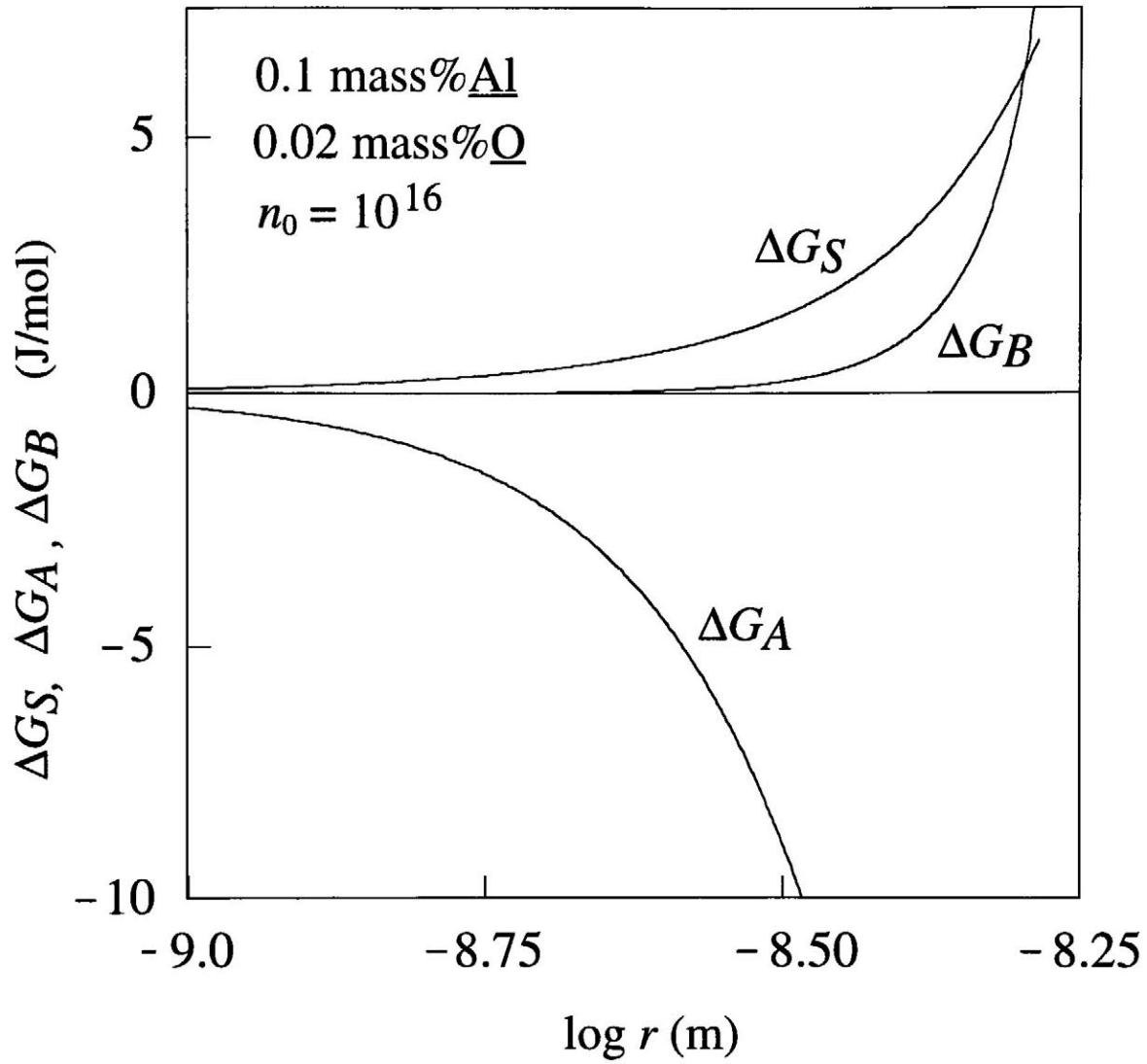

Fig. 4.7 The ΔG_S, ΔG_A and ΔG_B in Equation [4.1] for liquid iron having initial oxygen and aluminum contents of 0.02 mass% and 0.1 mass%, respectively, calculated using the activity values from Solution Model 2.

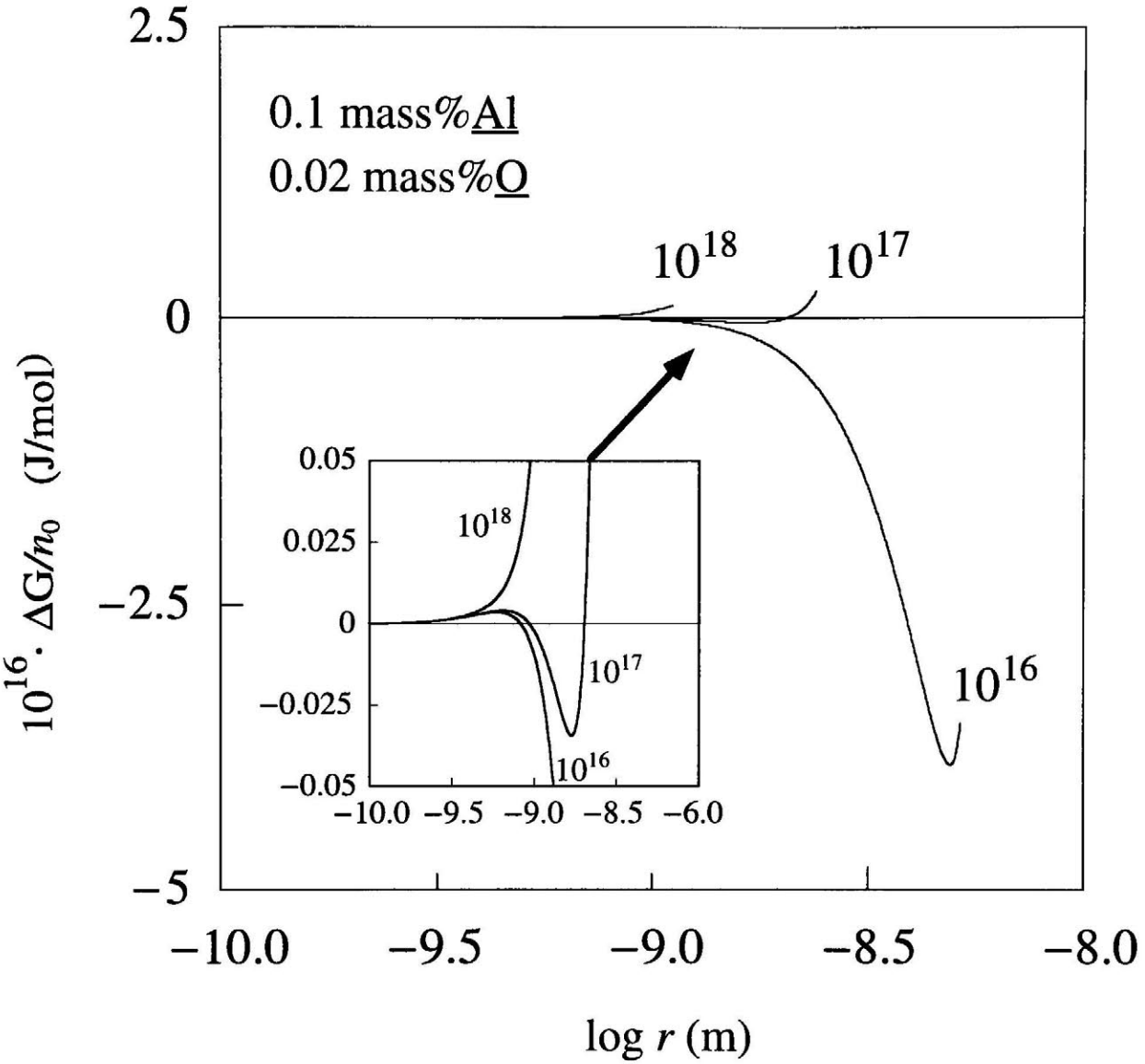

Fig. 4.8 Gibbs free energy change of a nucleus for various n_0 values (10^{16}, 10^{17} and 10^{18}) for 0.1 mass% Al and 0.02 mass% O calculated using the activity values from Solution Model 1.

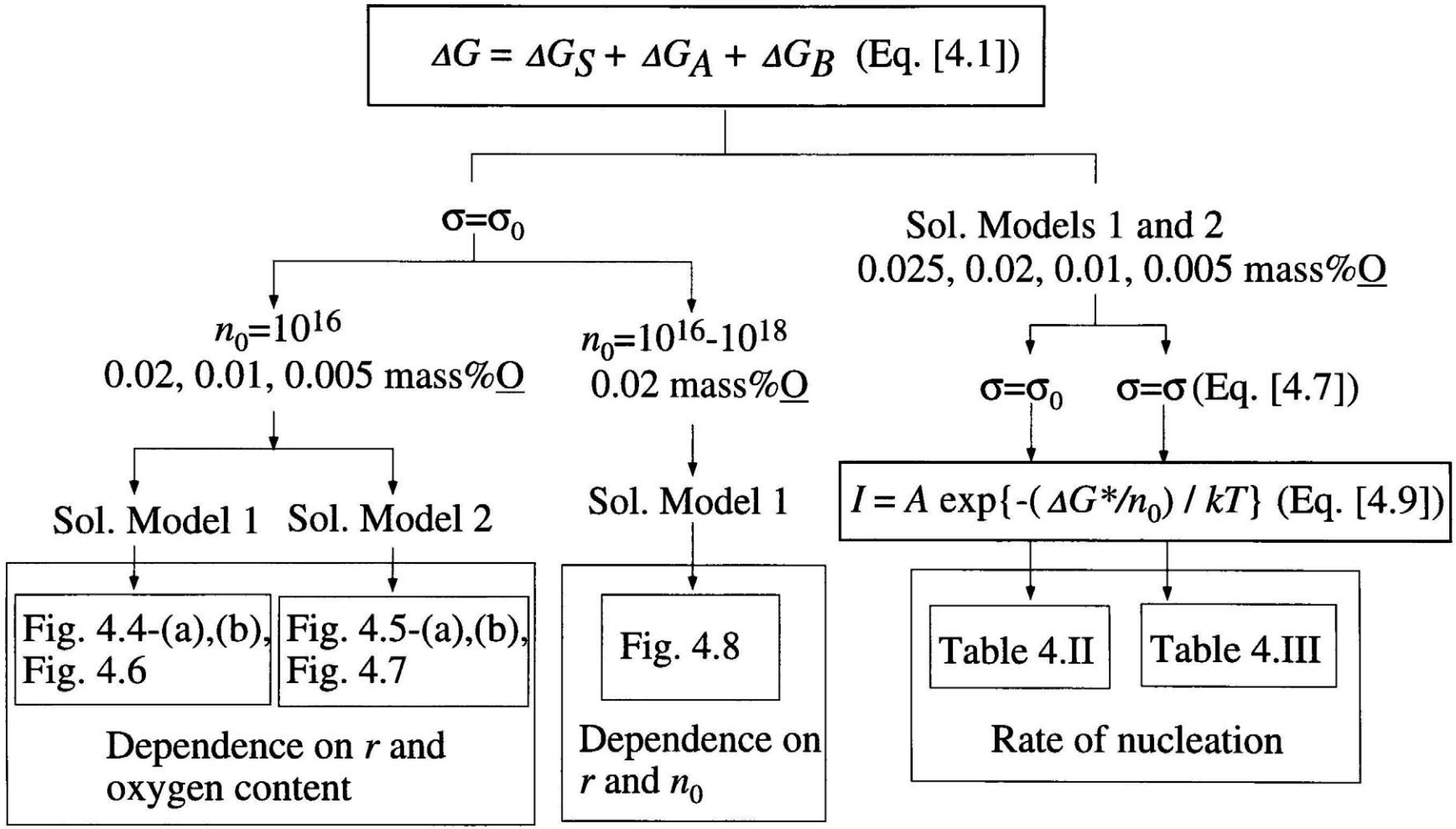

Fig. 4.9 Flow diagram of the calculations in the present work.

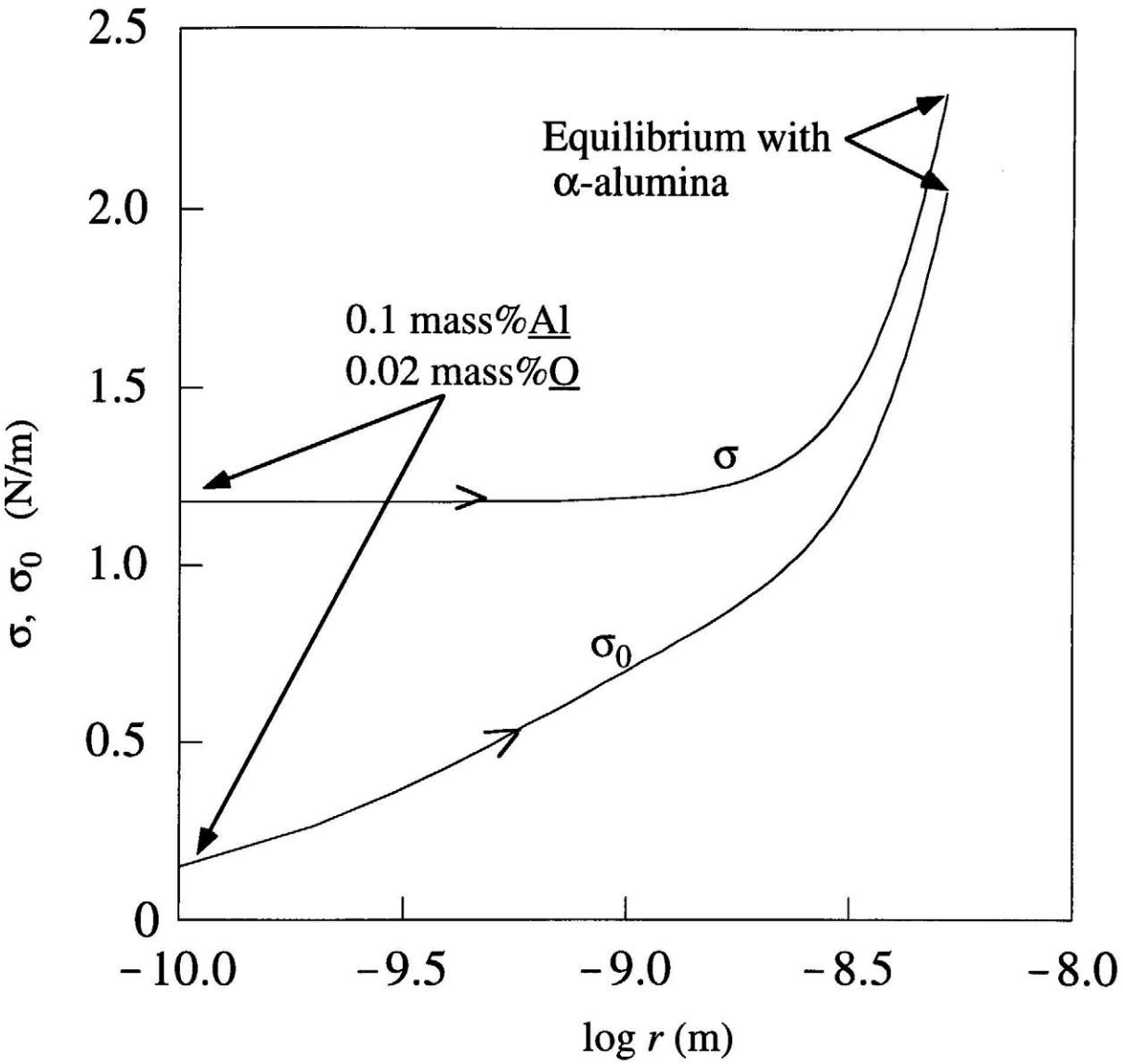

Fig. 4.10 Interfacial free energy changes in the nucleation process started from the liquid iron of initial 0.02 mass%O and 0.1 mass%Al contents (σ_0 from Equation [4.8] and σ from Equation [4.7]).

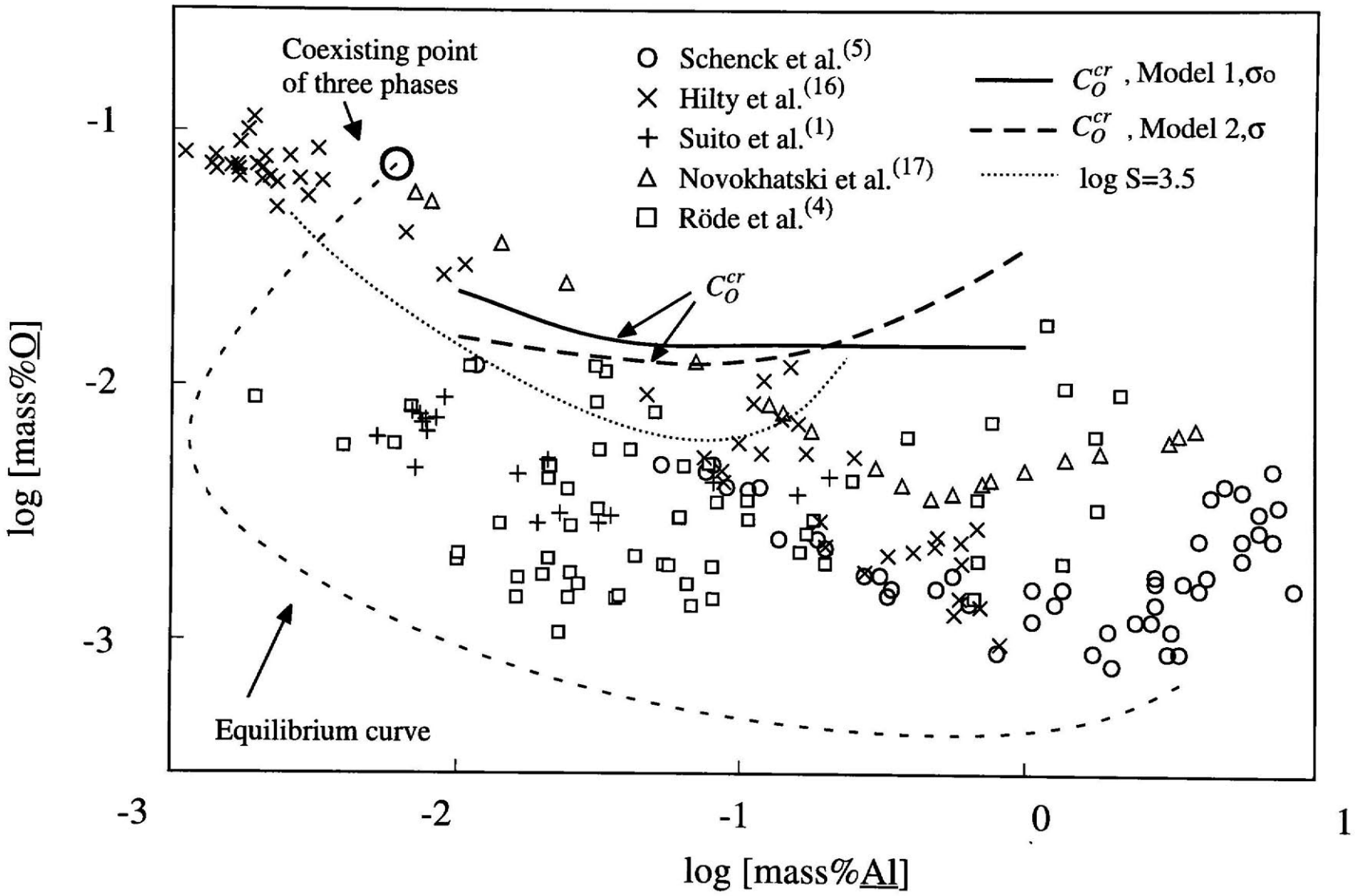

Fig. 4.11 log[mass%Al] vs. log[mass%O] as measured in various studies.

Table 4.I The degree of supersaturation for various contents of oxygen and aluminum calculated from Solution Models 1 and 2.

	Solution Model 1		Solution Model 2	
O content (mass%)	0.1 mass%Al	0.01 mass%Al	0.1 mass%Al	0.01 mass%Al
0.0250	5.8×10	6.0	1.1×10^{5}	1.1×10^{4}
0.0200	4.7×10	8.0	6.4×10^{4}	7.1×10^{3}
0.0100	2.4×10	1.1×10	1.1×10^{4}	1.2×10^{3}
0.0050	1.2×10	7.0	1.6×10^{3}	1.8×10^{2}

Table 4.II The rate of nucleation for various contents of oxygen and aluminum calculated from Solution Models 1 and 2 using σ_0 as the interfacial free energy. The critical radius of nucleus is shown in parenthses. The ∞ symbol indicates that the free energy change is negative for the entire range of the radius.

	Solution Model 1		Solution Model 2	
O content (mass%)	0.1 mass%Al (nucleus/mol·s)	0.01 mass%Al (nucleus/mol·s)	0.1 mass%Al (nucleus/mol·s)	0.01 mass%Al (nucleus/mol·s)
0.0250	10^{34} (2.1Å)	10^{13} (10.5Å)	∞	∞
0.0200	10^{29} (5.9Å)	≈ 0	∞	∞
0.0100	≈ 0	≈ 0	10^{33} (0.9Å)	10^{33} (3.2Å)
0.0050	≈ 0	≈ 0	4×10^{32} (3.2Å)	10^{13} (7.5Å)

Table 4.III The rate of nucleation for various contents of oxygen and aluminum calculated from Solution Models 1 and 2 using σ as the interfacial free energy. The critical radius of nucleus is shown in parenthses.

	Solution Model 1		Solution Model 2	
O content (mass%)	0.1 mass%Al (nucleus/mol·s)	0.01 mass%Al (nucleus/mol·s)	0.1 mass%Al (nucleus/mol·s)	0.01 mass%Al (nucleus/mol·s)
0.0250	2×10^{11} (6.5Å)	≈0	2×10^{32} (2.0Å)	8×10^{30} (2.6Å)
0.0200	≈0	≈0	2×10^{27} (3.0Å)	8×10^{21} (4.0Å)
0.0100	≈0	≈0	≈0	≈0
0.0050	≈0	≈0	≈0	≈0

Chapter 5 Observation of Inclusion in Aluminum-deoxidized Iron

I. Introduction

The presence of γ, δ, θ and κ-alumina inclusions has been reported[1-5] in iron solidified immediately after aluminum-deoxidation. The presence of amorphous silica inclusion in solidified iron has also been reported[2]. The reason why and how the unstable γ, δ, θ and κ-alumina and amorphous-silica inclusions form at steelmaking temperatures is unclear. Also, it is not known whether the unstable aluminas exist as secondary inclusions. However, there are no methods which provide unequivocal, distinctive classification of the two (primary and secondary) types of inclusions. Futhermore, in-situ observation of inclusions in liquid iron is impossible unless by the confocal laser-scanning microscope is used. Thus, we are forced to use the solidified sample to study inclusions even though the morphology, the size and the other information may be different to that when in contact with liquid iron.

In the present study, twin rollers were used to study inclusions in the aluminum-deoxidized liquid iron. The twin rollers press the liquid sample between rollers and solidify the sample so quickly that it results in several kinds of amorphous material. By using this method, liquid iron is solidified very rapidly, and thereby minimizes various changes and reactions which might be expected to occur during cooling and solidification. Comparison of inclusions in the sample solidified by twin rollers with those in the sample quenched in copper mold or water elucidates a distinctive way in which primary and secondary aluminas are formed.

The objectives of this study in Chapter 5 were (1) to confirm the formation of

secondary, unstable aluminas and amorphous silica, and (2) carry a thermodynamic inquiry to understand the formation of unstable inclusions.

II. Experimentals

A. Apparatus

The apparatus used in the present experiment consists of a vertical lanthanum chromite ($LaCrO_3$) resistance furnace fitted with twin rollers (Fig.5.1). A water-cooling jacket seals the top of the alumina tube (42 x 35 x 480 mm) in the furnace. At the other end of the tube, a vessel containing twin rollers is connected in gas-tight condition using O-ring. The connected part is cooled with a water-jacket. Another vessel for water quenching can be also connected to the aluminum tube in a similar manner. A shutter is mounted in each vessel just under the connection part which protects both the twin rollers and the vessel from thermal radiation. An alumina crucible (13 x 9 x 500 mm) is placed in the alumina tube in the furnace. The alumina crucible was constructed with high-grade alumina (99.5 mass % Al_2O_3, 0.1 mass % SiO_2). The bottom of a long alumina crucible containing the iron sample was sited in the constant-temperature-zone in the alumina tube of the furnace. The top of the alumina crucible was equipped with gas inlet and outlet and a sample addition device. High purity argon gas (99.999 %) was introduced directly into the crucible from the gas inlet. The gas outlet was closed when twin rollers were used. The gas flows out through an aperture (0.5 or 1 mm diameter) in the bottom of the crucible. The gas inlet was closed before the melting temperature of iron since the argon pressure tended to force liquid iron drip through the bottom aperture. Then, the argon gas was introduced from the gas inlet attached to the vessel and flowed out through the gas outlet attached to the water-jacket (50 ml/min.). The liquid iron in the crucible can be dripped

through the bottom aperture onto the twin rollers placed under the furnace by increasing the argon pressure in the crucible by opening the inlet of gas again. The two rollers are contact with each other and can rotate rapidly in opposite directions with the aid of a motor. The liquid iron dropped on it solidifies instantly by sandwiching, pressing and rolling between the rollers which are rotated at high speed (3100 rpm; ultra-rapid cooling). The liquid iron can also be quenched by lowering the bottom of the crucible quickly into the water, which was introduced just before quenching in the vessel (water quenching). In this case, the alumina crucible with no aperture (13 x 9 x 1000 mm) was used. Argon gas was introduced and flowed out through the gas inlet and outlet at the top of the crucible (50 ml/min.). Quenching by dripping the liquid iron into a copper mold placed on the shutter or in the vessel can be also performed (copper mold quenching).

The most rapid cooling rate which could be achieved with the ultra-rapid cooling method that was probably about 10^5 K/s[6] followed by the copper mold quenching and water quenching in this order.

B. Experimental Procedure

(1) Experiment 1

An alumina crucible containing electrolytic iron with 0.0360 mass % O was placed in the furnace, and the temperature raised to 1873 K. After arrival at 1873 K, deoxidizer (Fe-1.6 % Al) was added to the liquid iron from upper device. After the subsequent temperature drop and recovery within a few minutes, the liquid was maintained at 1873 K for a certain time (1, 5, 15, 30, 60 minutes). The added aluminum corresponds to 0.08 mass % of the total sample weight (about 15 g). The sample was then solidified ultra-rapidly (Exp. 1-A) or quenched into a copper mold (Exp. 1-B).

(2) Experiment 2

Pure aluminum and electrolytic iron containing 0.0625-0.0675 mass % O were added to the crucible which was maintained at 1873 K in the furnace. The added aluminum quantity corresponds to 0.125 mass % of the total sample weight (about 15 g). After melting, the liquid sample was maintained at 1873 K for a certain time (20, 40, 60 minutes) and was either solidified ultra-rapidly (Exp. 2-A) or quenched into copper mold (Exp.2-B). In Exp. 2-C, the liquid sample was maintained at 1873 K for 20 minutes and then quenched in water together with the crucible.

Hereafter, each experiment is referred to as Exp. 1, Exp. 2, Exp. 1-A and so on. Similarly, the solidified sample after the experiment is referred to as Sample 1, Sample 2, Sample 1-A and etc. The terms A, B, C in the experimental and sample numbers represent the solidifying method and cooling speed; the ultra-rapid cooling, the copper mold quenching and the water quenching, respectively.

C. Observation by SEM and TEM

To observe inclusions by SEM and TEM, the iron matrix was dissolved in dilute hydrochloric acid or iodine-methanol solution. Then, the inclusions were filtered using a filter made of polycarbonate or cellulose nitrate, the pore size of which was 0.1 μm. Even the fine particles smaller than the pore size could be extracted on the filter because such fine particle was apt to adhere to other material and attache firmly. In experiments using hydrochloric acid, alumina and hercynite inclusions, which are insoluble in acid, can be observed on the filter. In experiments using iodine-methanol solution, wüstite inclusions, in addition to alumina and hercynite, were observed. Observation of the filter by EPMA revealed that a long time exposure to electron beam caused damage of

the filter and many inclusions were too small to observe, although the moderate size of the inclusion could be observed. Thus, we performed Filter Replica Method for TEM (F.R.M.). This is a new way developed in the present study of observing inclusions on a filter (polycarbonate, 0.1 μm pore size) by TEM. Over the filter, the carbon was deposited under vacuum conditions. A few pieces of square part (0.3 x 0.3 mm) were cut from the center of the filter. As the polycarbonate is soluble into chloroform, immersion of the cut filters into chloroform causes them dissolution. Then the carbon films, on which many inclusions are adhered, floated up to near the surface of the chloroform solution. Each film can then be scooped onto copper-sheet-mesh, which is usually used to support the TEM sample. After rinsing it with acetone, ethanol and water, the inclusions on the carbon film can be observed by TEM. The Sample 1-A and Sample 1-B were observed by SEM and the Sample 1-A, Sample 2-A, Sample 2-B and Sample 2-C were observed by TEM (F.R.M.).

D. Identification of Inclusion

The constituent elements of inclusion were analyzed by the EPMA or EDX apparatus belonging to SEM and TEM. The inclusion was identified from the constitution as hercynite, alumina, or wüstite. Electron diffraction analysis of alumina inclusion was also performed and the result was analyzed by taking the crystal forms of α, β, γ, δ, θ, κ' and κ-aluminas into consideration. The lattice constants and X-ray diffraction peaks of α, β, γ, δ, θ and κ'-aluminas from the ASTM table were used in the analysis. The lattice constants of κ-alumina from the report by Adachi et al[4] were also used. However, identification based only on the diffraction pattern is generally difficult, because many polymorphisms of alumina are present and the patterns of different crystals often coincide with each other within errors of measurement of diffraction spot

distance and angle. Therefore, several diffraction patterns from different directions were observed for the inclusion, if any distinct diffraction patterns could be obtained within the rotation limit of sample holder (±13 degrees for two transverse directions). For the γ and δ-alumina, the identification was easier because they often show characteristic diffraction patterns[7]. The identification of the inclusion from the diffraction pattern was performed for inclusions where the diameter exceeded about 0.05 μm because the diffraction patterns of very fine inclusions were not clear. By contrast, the electric beam could not pass through the large inclusions (a few μm thickness). Thus, the identification of inclusions with large thickness could not be performed.

III. Results and Discussion

Aluminum analysis of the Sample 1-B which was maintained at 1873 K for 5 minutes, showed the variation of aluminum content from 0.01 to 0.05 mass %. In order to improve the mixing condition of aluminum, the Exp. 2 was performed but similar aluminum variation (0.03-0.08 mass % Al) in Sample 2-B (maintained at 1873 K for 20 minutes) was observed. The formation of alumina primary inclusions at some aluminum-rich position would occur during melting of the sample; the inclusions would float upwards in the liquid iron agglomerating; the solid alumina would be tended to adhere to the crucible wall and subsequently it would grow catching other inclusions and disturb further aluminum diffusion, resulting heterogeneous distribution of alumina and aluminum in the sample for more than 20 minutes after sample addition in the crucible. However, no marked distinctive differences in the species and the shapes of the inclusions between Sample 1 and Sample 2 were observed. Thus, only the classification of the inclusion's shape and size as a function of cooling speed were analyzed in the present experiment. The chemical species and the

crystal structure of alumina were also analyzed.

A. Shape, Size and Species of Inclusion

Dendritic (Fig. 5.2), maple-like(Figs 5.2-(a), 5.2-(b), and 5.2-(c)), polygonal (Figs. 5.2-(b), 5.2-(c), and 5.4-(b)), coral-like (Fig. 5.4-(d)), network-like (Figs. 5.3, 5.4-(a), and 5.4-(c)) and spherical inclusions (Figs. 5.2-(a), 5.2-(b), 5.2-(c), 5.3, and 5.4-(a)) were observed in the present experiments.

(1) Dendritic Maple-like and Polygonal Inclusions

Dendritic and maple-like inclusions on filter were observed in Sample 1 by SEM (Figs. 5.2-(a), 5.2-(b), and 5.2-(c)) especially in the sample maintained 1 or 5 minutes at 1873 K and rarely in the sample maintained for longer times. Many of the dendritic and maple-like inclusions would form during the first stage of deoxidation and, subsequently, float up growing and agglomerating. The agglomerated alumina would be tended to adhere to the crucible wall and, thus, it would not pass through the aperture of the crucible in Exp. 1 which was maintained at 1873K for 15 minutes or more. However, on all the replica films for TEM observation of Sample 1-A, Sample 2-A and Sample 2-B including the replica films of Sample 1-A maintained at 1873K for 1 or 5 minutes, dendritic and maple-like inclusions were not observed. It is probably due to the restricted area (3 x 3 mm) of a cut filter for TEM observation. In contrast, by SEM, wide area of a filter can be scanned and, thus, the dendritic and maple-like inclusions could be observed. In the Sample 2-C, which had been quenched in water with crucible, the inclusions seemed like agglomeration of some dendritic inclusions were observed (Fig. 5.2-(d)).

Polygonal inclusions were observed in almost every sample of Exp. 1 and Exp. 2 by SEM and TEM.

The dendritic and maple-like inclusions are alumina, but they sometimes

contain a small quantity of iron or silicon. The polygonal inclusion contains silicon and aluminum. The silicon could originate from silica impurities in the alumina crucible because there is no silicon source other than the silicon contained in the electric iron used in the present experiment, which is lower than 7 mass ppm. The polygonal inclusions were observed even in Sample1-B which were cooled after maintaining at 1873 K for only 1 minute. Thus, the silicon dissolution from crucible could occur from an early stage of iron melting or in a subsequent period where the temperature increased after melting.

The dendritic, maple-like and polygonal inclusions have similar length (a few μm to a few ten μm) even in the samples quenched at different cooling speeds (Fig. 5.2). Thus, these inclusions are considered to be primary inclusions.

The identification of structure of the dendritic, maple-like and polygonal inclusions by electron diffraction analysis was not performed because of their thickness.

(2) Spherical Inclusions

Spherical inclusions were observed in almost every sample of Exp. 1 and Exp. 2 by SEM and TEM (Figs. 5.2, 5.3, 5.4-(a), and 5.4-(b)). The spherical inclusions were alumina or hercynite. When the solidified iron was dissolved into iodine-methanol solution, wüstite spherical inclusions were also observed. The observed spherical wüstite inclusions would have precipitated at the iron with a high oxygen content. These wüstite inclusions should be secondary inclusion, because wüstite liquid particles could not be formed in liquid iron at 1873K judging from the high solubility of oxygen in liquid iron. In Figs. 5.3-(a), 5.3-(b), 5.3-(c), 5.3-(d), and 5.4-(a), very small spherical inclusions are shown. Figures 5.3-(a) and 5.3-(b) show the inclusions in Sample 2-A (dissolved in iodine-methanol solution). Figures 5.3-(c) and 5.3-(d) show the

inclusions in Sample 2-B (dissolved in iodine-methanol solution). Figures 5.3-(b) and 5.3-(d) are the magnified TEM images of encircled parts with broken line in Figs. 5.3-(a) and 5.3-(c), respectively. The diameter of spherical inclusions in Sample 1-A and Sample 2-A were around 30 nm and these in Sample 2-B were around 60 nm, although some variation in diameter was observed. Figures 5.4-(a) and 5.4-(b) show the spherical inclusions in Sample 2-A (dissolved in hydrochloric acid) and Sample 2-C (dissolved in hydrochloric acid), respectively. In Fig. 5.4-(a), an enlarged photograph of encircled part with square frame is shown, in which small spherical inclusions are observed. The spherical inclusions in the water-quenched sample have diameters in the range several hundreds nm to a few μm (Fig. 5.4-(b)) although a few inclusions with smaller diameter than 100 nm are present. In the result, the spherical inclusions are classified as secondary inclusions because their size changed with cooling rate (Figs. 5.3-(a), 5.3-(b), 5.3-(c), 5.3-(d), 5.4-(a), and 5.4-(b)). However, wide scattering of diameter is observed, especially in the sample quenched in water. The spherical inclusions formed at the first stage of cooling have chance to grow or coalesce until the iron was solidified. In contrast, those formed at the final stage of solidification have no time to grow. Thus, the variation of diameter would reflect the time interval between the first stage of cooling and the final stage of solidification.

The finest spherical alumina ever observed clearly in Sample 1-A and Sample 2-A was about 10 nm in diameter. These finest particles are often observed as a colony which would meet together in acid solution during filtration and the colony seems to consist of the particles of the same species because the pattern of EDX peaks taking for some particles were the same. In Fig. 5.5-(a), a colony observed in Sample 1-A (maintained at 1873K for 5 minutes) whose

several constituent particles show the peaks of hercynite is shown. In Fig. 5.5-(b), a part of the colony of fine alumina particles of about 10-30 nm observed in Sample 2-A (maintained at 1873K for 40 minutes) is shown. Figure 5.5-(c) shows the particles smaller than 10 nm observed in Sample 1-A (maintained at 1873K for 5 minutes). Figure 5.5-(c) is the only one photograph in which such small particles could be seen in comparative clarity, but regretfully, these particles could not be identified by EDX, although they are hercynite or alumina. The photograph at large magnification of such colony is often unclear. This is probably due to the covering of carbon film and also to some overlapping and smallness of the particles.

A few large spherical inclusions with a diameter roughly from 1 to 5 μm observed in Sample 1-A, Sample 1-B, Sample 2-A and Sample 2-B, which stand out from others are observed in every sample (Figs. 5.2-(a), 5.2-(b) and 5.2-(c)). The formation mechanism of these inclusions could be different from the secondary spherical inclusions and they would be primary inclusions because their size did not change with cooling rate.

In Sample 1-A maintained at 1873 K for 60 minutes, a few spherical amorphous silica inclusions were observed (Figs. 5.6-(a) and 5.6-(b)), which were almost pure silicas. The silica would originate from impurities in the alumina crucible. The amorphous silica could be secondary inclusion because primary silica was often observed as a polygonal inclusion containing alumina. Furthermore, it does not seem rational that the silica once dissolved in liquid iron could solidify, melt and solidify again as amorphous silica in the same liquid iron. However, the certain proof that amorphous silica is secondary inclusion is necessary.

(3) Network-like and Coral-like Inclusions

In Figs. 5.3 and 5.4, network-like and coral-like inclusions are shown. The coral-like inclusion seems to be a fragment of a network-like inclusion and the network-like inclusion sometimes extends widely as a plane. The trunk of the network-like and the coral-like inclusion in Sample 1-A, Sample 2-A, Sample 1-B and Sample 2-B has an angular shape but that in Sample 2-C is roundish (Figs. 5.4-(c) and 5.4-(d)). The coral-like and network-like inclusions are alumina, but they sometimes contain a small quantity of iron or silicon. The trunk thickness of the coral -like or the network-like inclusion in Sample 1-A and Sample 2-A was 100 -200 nm (Figs. 5.3-(a) and 5.3-(b)), that in Sample 1-B and Sample 2-B was 200-400 nm (Figs. 5.3-(c) and 5.3-(d)), and that in Sample 2-C was 1-2 μm (Figs. 5.4-(c) and 5.4-(d)). Thus, the network-like and the coral-like inclusions in the samples cooled ultra-rapidly or quenched into a copper mold are secondary inclusions because their trunk thickness varies with cooling speed. However, the variation of the trunk-thickness in the same sample was not so large as that of the spherical inclusions. Therefore, the stage of formation of the network-like and coral-like inclusions might be restricted.

The network-like and coral-like inclusions in Sample 2-C, which was water-quenched together with crucible were roundish (Figs. 5.4-(c) and 5.4-(d)) in contrast to the angular shape of those observed in Sample 1-A, Sample 1-B, Sample 2-A and Sample 2-B (Figs. 5.3-(a), 5.3-(b), 5.3-(c) and 5.3-(d)). The coral-like inclusions in Sample 2-C seemed to be the result of multiple union of spherical inclusions (Fig. 5.4-(d)). The network-like inclusions in the Sample 2-C seems to be formed when several coral-like inclusions were superimposed upon one another (Fig. 5.4-(c)). Thus, the formation mechanism of the network-like and coral-like inclusions in Sample 2-C might be different with those of the inclusion observed in the Sample 1-A, Sample 1-B, Sample 2-A and

Sample 2-B. More investigation and consideration for the network-like and coral-like inclusions will be necessary.

B. Structure of Spherical, Network-like and Coral-like Inclusions

The network-like and coral-like inclusions are polycrystalline. The spherical inclusions were often observed as polycrystals. The diffraction pattern for spherical alumina inclusions revealed that most of them were the γ-alumina. However, another vague diffraction pattern with spots lined at narrow intervals often overlapped on it (Fig. 5.7-(a)). The lattice constants for **a** and **b** axes of the γ-alumina (cubic; **a**=7.9, **b**=7.9, **c**=7.9) and δ-alumina (tetragonal; **a**=7.943, **b**=7.943, **c**=23.5) are almost the same, and the lattice constant for the **c** axis of the δ-alumina is about three times of that of the **a** and **b** axis. Thus, the two crystals could easily mix with one another and the vague overlapping pattern is probably due to the small amount of mixing of δ-alumina in γ-alumina. Some of the network-like inclusions were identified as α, γ and δ-alumina (Figs. 5.7-(b) and 5.7-(c)). The diffraction pattern of the network-like γ-alumina was similar to that of spherical γ-alumina, indicating the small amount of mixing of δ-alumina. The electron diffraction pattern of the spherical silica observed in Sample 1-A (maintained at 1873 K for 60 minutes) showed a halo pattern characteristic for amorphous material (Figs. 5.6-(a) and 5.6-(b)).

The ratio of aluminum to iron in the hercynite was observed to vary and the wüstite inclusion often contained a small quantity of aluminum. Since wüstite and hercynite are soluble in one another in the liquid phase at 1873 K and have the same cubic crystalline structure, the hercynite nuclei can dissolve in liquid wüstite. The wüstite liquid particles containing hercynite would agglomerate through collision during cooling and crystallize as a solid solution, having no time to separate. Since the lattice constant of hercynite (8.113 Å) is nearly

twice that of wüstite (4.307 Å), the wüstite containing a small amount of hercynite has often a similar diffraction pattern to hercynite, showing spots at the center of the two regular spots. On the contrast, the lattice constant of hercynite containing wüstite is larger than that of pure hercynite. In the present study, the inclusion formed from the solid solution which is insoluble to acid is called hercynite, because the solid solution containing significant amount of wüstite would dissolve into acid.

C. Formation Mechanism of Unstable Alumina and Amorphous Silica

In the present experiment, the γ and δ-aluminas in addition to α-alumina were observed not only in the iron having solidified immediately after aluminum deoxidation but also in iron having solidified 40 minute after deoxidation. The unstable aluminas are classified as the secondary inclusions.

Iwamoto[1] and Adachi et al.[4] reported that the hydrogen absorbed into alumina could not be eliminated even through a heating to high temperature and suggested the possibility of hydrogen effect to the unstable alumina formation. However, the solubility of hydrogen in liquid iron is 20-30 mass ppm at 1873 K and 1 atm H_2. Thus, even if hydrogen might influence the formation of unstable alumina, the hydrogen will be consumed for the primary alumina formation and the effect to the secondary alumina formation will be scarce at this experiment.

The oxygen in liquid iron frequently exceeds the value for equilibrium with α-alumina. The origin of the excess oxygen was already discussed in a previous artticle[8] and Chapter 4. It was concluded that the excess oxygen originates in part from the suspension of fine alumina deoxidation products in liquid iron and in part from the supersaturation of oxygen or the supersaturation of an alumina-associated compound in liquid iron[8,9]. From the consideration

on Ostwald's step rule[10, 11], the supersaturated state would cause the secondary, unstable alumina formation . Further, there is another important point to be considered, which is the presence of amorphous silica inclusion. Both the unstable aluminas and the amorphous silicas should be formed during cooling through similar mechanisms. However, the size dependence for amorphous silica inclusions with the cooling speed was not confirmed in this experiment because it was scarcely observed. The evidence for classifying amorphous silica as secondary inclusion was obtained in an experiment on the Cu-O-Si system at 1423K which will be discussed in Chapter 7. The present author will make further detailed discussion in the next Chapter 6 on this mechanism of the unstable alumina formation in which the discussion on the mechanism of the network-like inclusion and amorphous silica inclusion formation will be included.

D. Minimum Size of Inclusion

The minimum diameter of alumina and hercynite inclusions observed in the present work is in the range from a few nm to 10 nm. These inclusions were extracted by filtration of the hydrochloric acid solution in which iron sample was dissolved. However, Inoue et al. reported that fine alumina powder could be dissolved partly into mixed solution of nitric acid and hydrochloric acid[12]. Wakamatu reported that the alumina and the hercynite extracted from iron did not dissolve into nitric acid or mixed solution of nitric acid and hydrogen peroxide[13]. Thus, the species of acid or the process of alumina synthesis will probably have an influence on its solubility. Against this, Inoue et al. obtained the aluminum-deoxidized iron sample by heating at 1873 K in an alumina crucible and showed that the sum of the oxygen content calculated from the insoluble aluminum in acid (Insol Al) and the equilibrium oxygen value was

smaller than the total oxygen[12]. From the result, they concluded that fine alumina in iron was dissolved in acid. The present author do not always deny the dissolution of very fine alumina, yet, have a question about the quantity of dissolution of alumina reported by Inoue et al. For instance, there should be silica inclusions even in the aluminum-deoxidized iron. In the sample heated for 1 hour at 1873 K, there should be the silica which originated from the impurity of alumina crucible. The silica dissolution should be depend firstly on the oxygen and silicon contents in liquid iron. However, under the same condition of liquid iron, it would depend on the purity of alumina crucible[14]. In the present experiment, even from a high purity, alumina crucible, the silica was dissolved in the liquid iron. Thus, the difference between the total oxygen and the sum of oxygen derived from Insol Al and equilibrium value is not always an indication of alumina dissolution. In addition, the equilibrium value of oxygen content is not yet determined correctly and Insol Al was detected even in the solidified iron which had been in the liquid state in equilibrium with α-alumina[15]. However, it might be natural that the fine alumina (constructed of a few or a few ten molecules) would tend to dissolve into acid. If fine alumina can be dissolved in acid, the diameter about ten nm of the finest alumina observed in the present experiment might have been larger in the liquid iron. On the other hand, very fine alumina inclusions, of smaller size than those observed in the present study, might exist in the iron sample and would not be observed since they would dissolve in the acid. As the author described earlier from the calculations based on nucleation theory, the suspension of alumina particles should be present in liquid iron[8]. If the suspended alumina particle in liquid iron does not collide and coalesce during cooling and does not dissolve in acid, the smallest alumina with about 10 nm observed in the present

study might be the suspended particle. On the other hand, the smallest alumina with about 10 nm diameter observed in the present study might be formed at the latest stage of solidification. In any case, further investigation of the finest inclusions present in an iron matrix is expected to clarify the nucleation mechanism.

IV. Conclusion

Two types of experiment (Exp. 1 and Exp. 2) were performed. In both experiments, the iron-oxygen alloy was deoxidized with aluminum deoxidizer while heating at 1873K. The deoxidized iron was solidified using 3 different cooling methods: (1) the ultra-rapid cooling using twin rollers (ultra-rapid cooling), (2) the quenching of iron into copper mold, and (3) the quenching of the iron-bearing crucible in a water bath The most rapid cooling rate achieved with (1), which was probably about 10^5 K/s[(6)], followed (2) and (3).

In the sample in Exp. 1 and Exp. 2, dendritic, maple-like, polygonal, network-like, coral-like and spherical inclusions were observed. Almost all dendritic, maple-like, coral-like and network-like inclusions are alumina, but they sometimes contain a small quantity of iron or silicon. The polygonal inclusion contains silicon and aluminum. The spherical inclusion is alumina, hercynite or wüstite.

The dendritic, maple-like and polygonal inclusions are classified as primary inclusions because they did not vary in size with differing the cooling rates. Many of the dendritic and the maple-like inclusions would form during the first stage of deoxidation. The network-like and coral-like inclusions in the sample cooled ultra-rapidly and quenched into copper mold and spherical inclusions are classified as secondary inclusions because they decreased in size with increases in cooling rate. However, a few large spherical inclusions, which would be

primary inclusions, were present. The network-like and coral-like inclusions in the sample quenched into water might be formed in different mechanism.

The analysis of the electron diffraction patterns of inclusions made clear that the α, γ and δ-alumina were present as secondary inclusions. Amorphous silica inclusions were also observed. The supersaturated state of oxygen in liquid iron could cause the secondary, unstable alumina formation. The amorphous silica would be formed during cooling through similar mechanism.

The minimum diameter of spherical inclusions of alumina and hercynite observed in the present work is in the range from a few nm to 10 nm.

References

1. N.Iwamoto: Tetsu-to-Hagane, **58**(1972), 787.
2. F.Honda and K.Hirokawa: Tetsu-to-Hagane, **60**(1974), 287.
3. S.Watanabe, K.Takano, K.Moriya, Y.Tu and Y.Shiroishi: Tetsu-to Hagane, **65**(1979), 383.
4. A.Adachi, N.Iwamoto and Y.Ueda: Tetsu-to-Hagane, **51**(1965), 1617.
5. M.Okubo, Y.Miyashita and R.Imai: Tetsu-to-Hagane, **54**(1968), S59.
6. H.S.Chen and C.E.Miller: Rev. Sci. Inst., **41**(1970), 1237.
7. B.C.Lippens and J.H.de Bore: Acta. Cryst, **17**(1964), 1312.
8. K. Wasai and K.Mukai: Metallurgical and Materials Transaction B, **30B** (1999)1065 - 1074 .
9. K.Wasai and K.Mukai: The Final Report of Ultra Clean Steel Research Group, Progress in Research on Ultra Clean Steel -Fundamental and Applied Aspects- (1999), 3, No.9511, The iron and Steel Institute of

Japan.

10. W. Ostwald: Z.Phy.Chem., **22**(1897), 289.

11. H.Singu and K.Ishihara: Bulletin Japan. Inst. Metals, **25**(1986), 16.

12. R.Inoue and H.Suito: The Final Report of Ultra Clean Steel Research Group, Progress in Research on Ultra Clean Steel -Fundamental and Applied Aspects- (1999), 330, No.9511, The iron and Steel Institute of Japan.

13. S.Wakamatsu: Tetsu-to-Hagane, **57**(1971), 1360.

14. T.Dan, H.Yin, N.Aritomi, K.Ogawa and Y.Nakamura: J. Japan Inst.Metals, **49**(1985), 865.

15. K.Wasai and K.Mukai: J Japan Inst. Metals, **52**(1988), 1088.

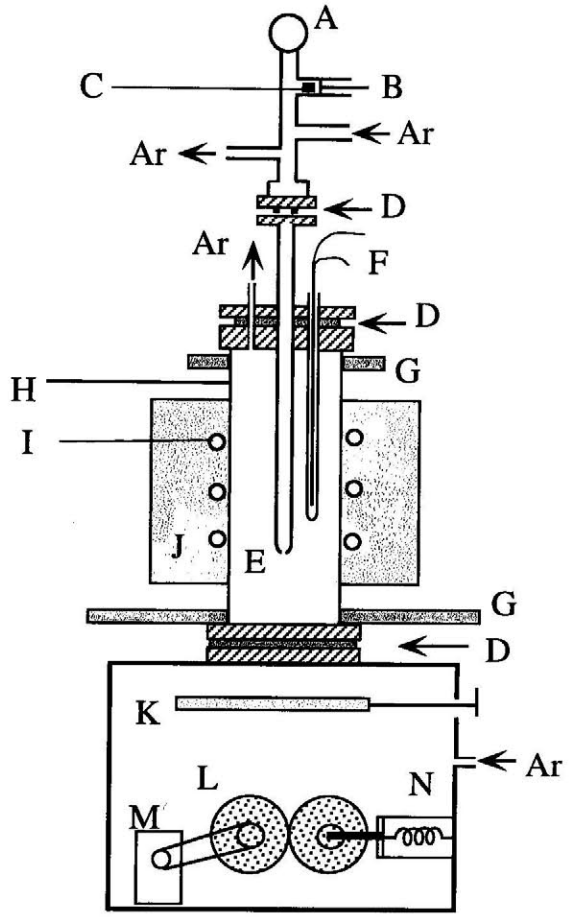

A: Pressure gauge,
B: Sample dropping device,
C: Iron specimen
D: O-ring,
E: Alumina crucible,
F: Thermocouple sheath,
G: Cooling device,
H: Alumina reaction tube
I: $LaCrO_3$ Heater,
J: Alumina refractory,
K: Shutter
L:Roller
M:Motor,
N:Spring

Fig. 5.1 Schematic diagram of experimental apparatus.

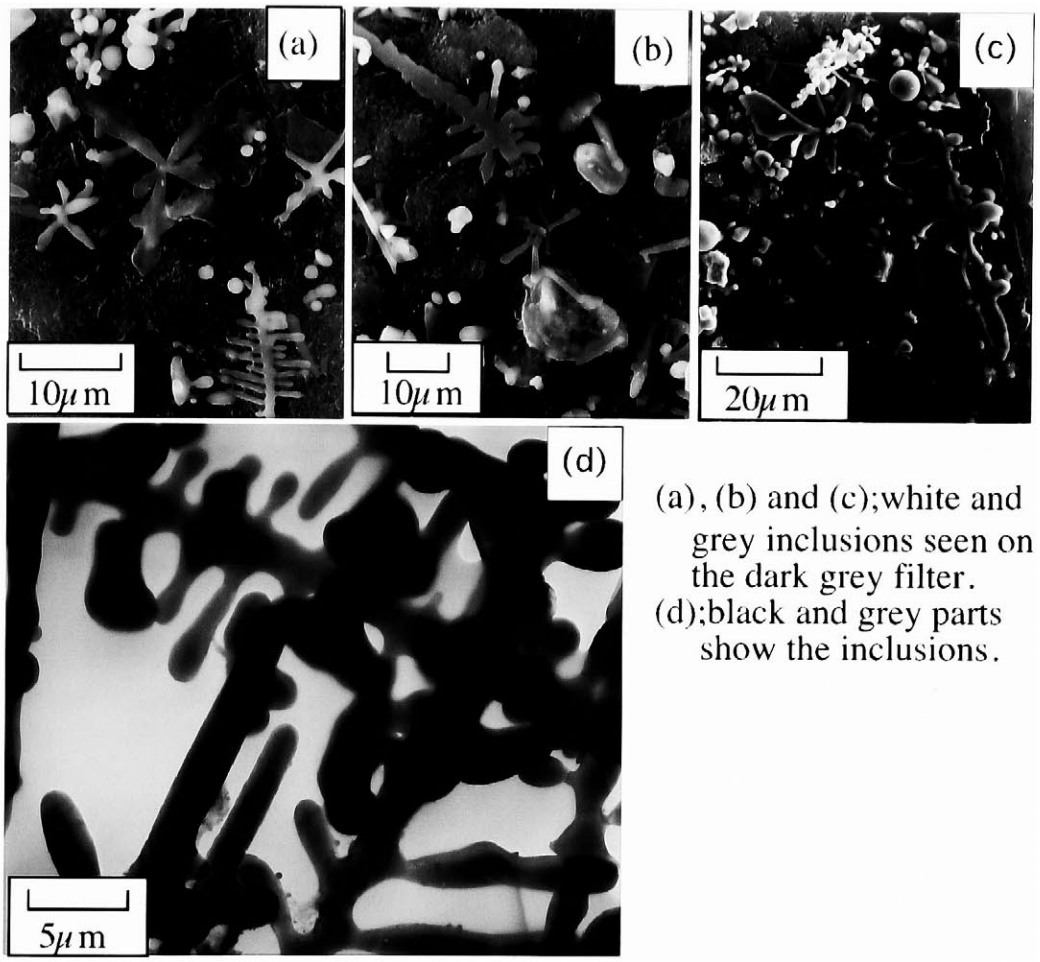

Fig. 5.2 (a) SEM image of dendritic, maple-like and spherical inclusions on a filter in Sample 1-A maintained at 1873K for 1 minute.
(b) SEM image of dendritic, maple-like, polygonal and spherical inclusions on a filter in Sample 1-A maintained at 1873K for 5 minutes.
(c) SEM image of dendritic, maple-like, polygonal and spherical inclusions on a filter in Sample1-B maintained at 1873K for 5 minutes.
(d) Dendritic inclusions in Sample 2-C maintained at 1873K for 20 minutes (F.R.M.).

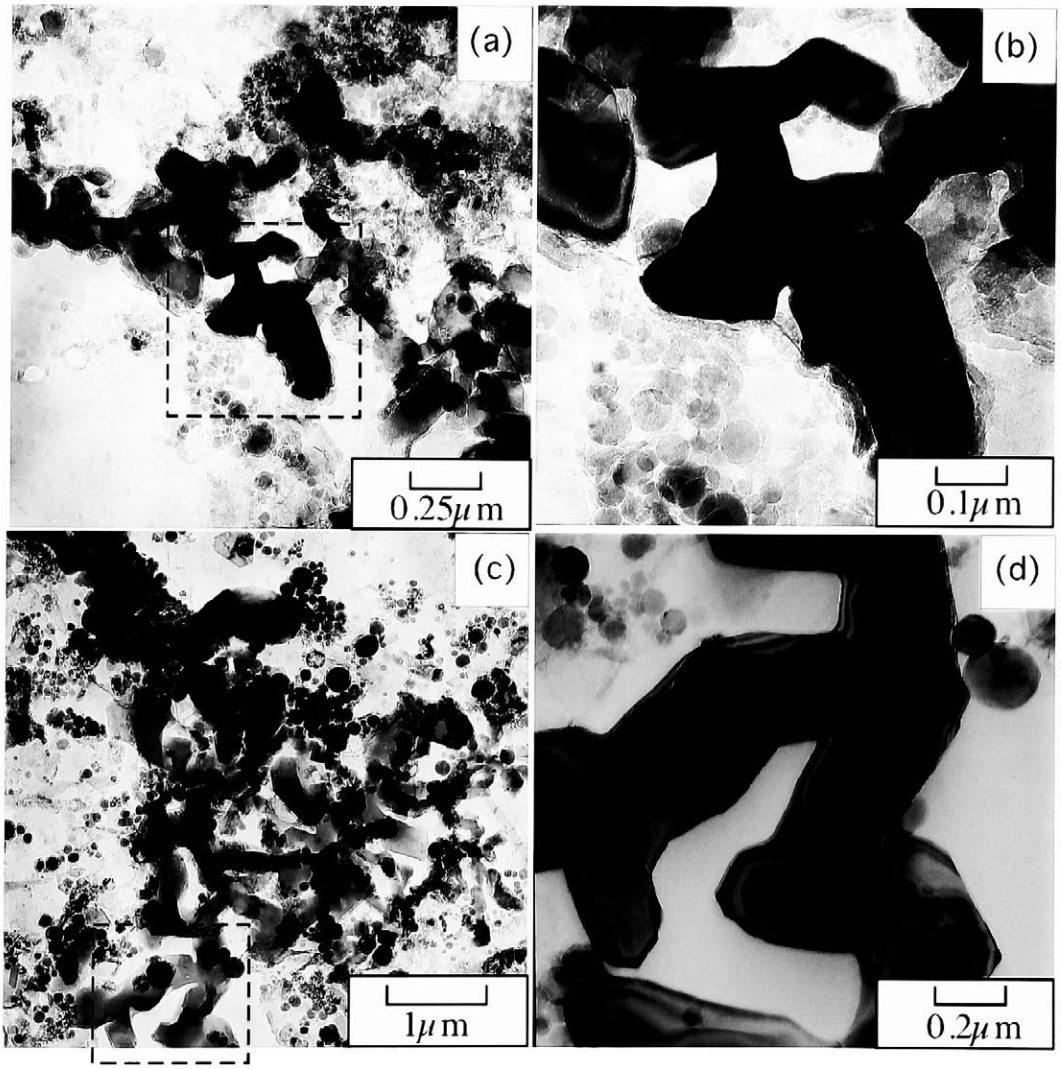

Fig. 5.3 (a), (b) Spherical and network-like inclusions in Sample 2-A maintained at 1873K for 40 minutes (F.R.M.).
(c), (d) Spherical and network-like inclusions in Sample 2-B maintained at 1873K for 20 minutes (F.R.M.).

(a),(b),(c),(d); black and grey parts show inclusions on the light grey carbon film.

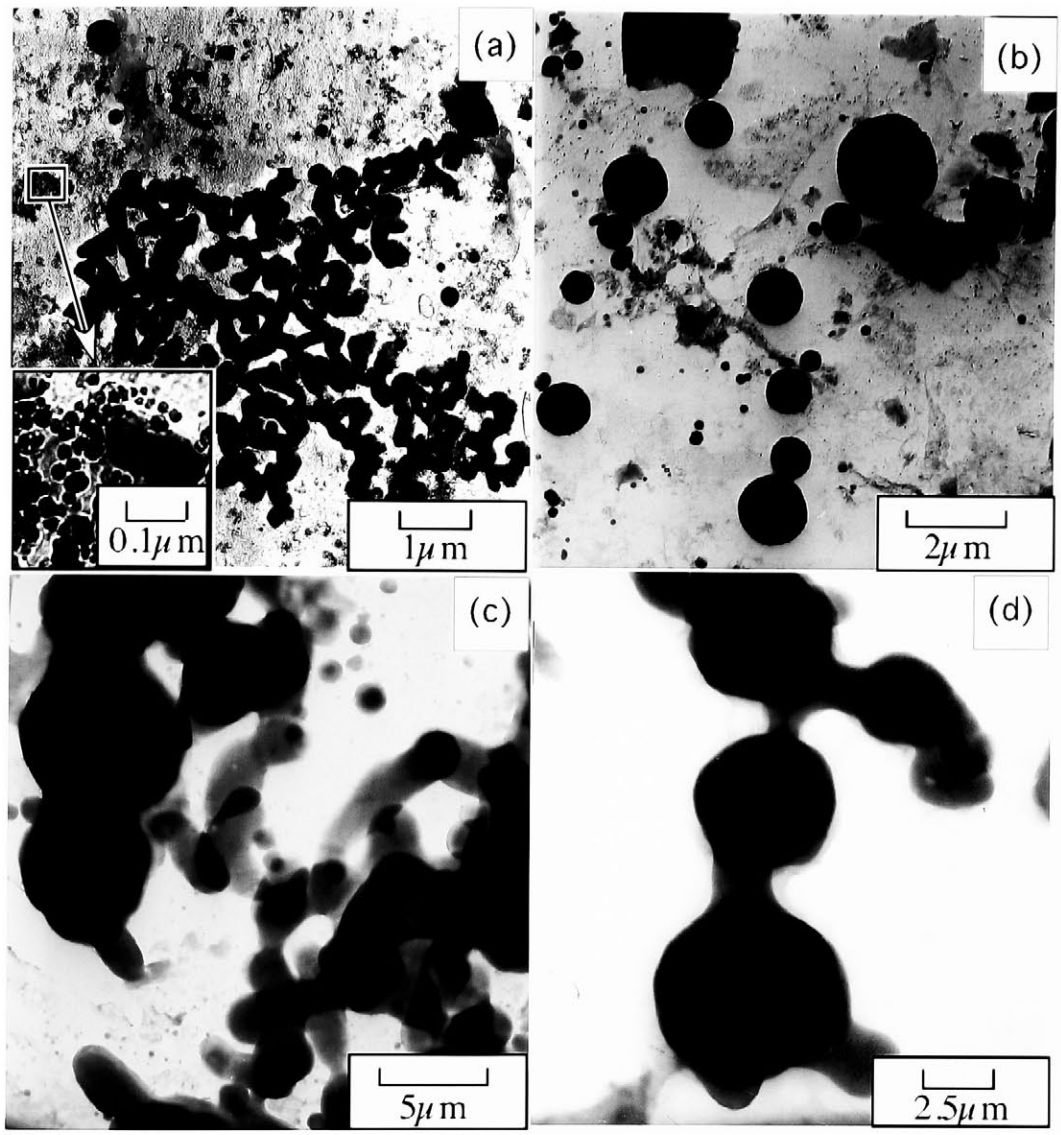

Fig. 5.4 (a) Spherical and Network-like inclusion in Sample 1-A maintained at 1873K for 5 minutes (F.R.M.).
(b) Spherical inclusions in Sample 2-C maintained at 1873K for 20 minutes (F.R.M.).
(c) Network-like inclusion in Sample 2-C maintained at 1873K for 20 minutes (F.R.M.).
(d) Roundish coral-like inclusion in Sample 2-C maintained at 1873K for 20 minutes (F.R.M.).

(a),(b),(c),(d); black and grey parts show inclusions on the light grey carbon film.

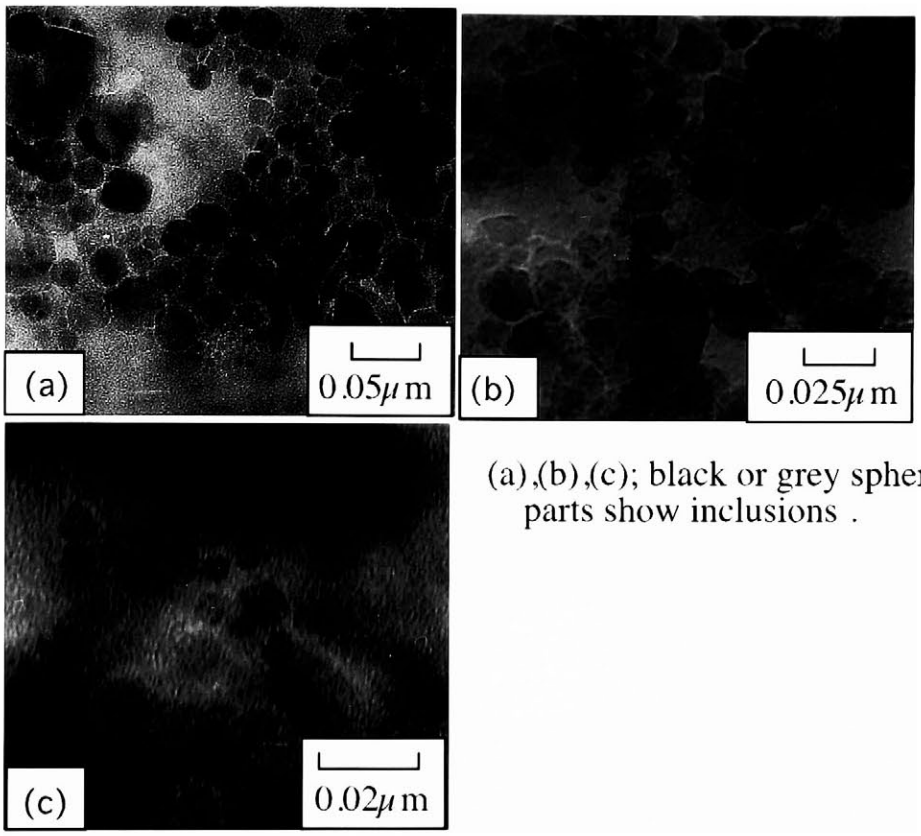

Fig. 5.5 (a) Colony of fine spherical inclusions in Sample 1-A maintained at 1873K for 5 minutes. Several particles in the colony are shown as the hercynite by EDX.

(b) Colony of fine spherical inclusions in Sample 2-A maintained at 1873K for 40 minutes. Several particles in the colony are shown as the alumina by EDX.

(c) The finest inclusion observed in the present experiment in a colony of fine spherical inclusions in Sample 1-A maintained at 1873K for 5 min.

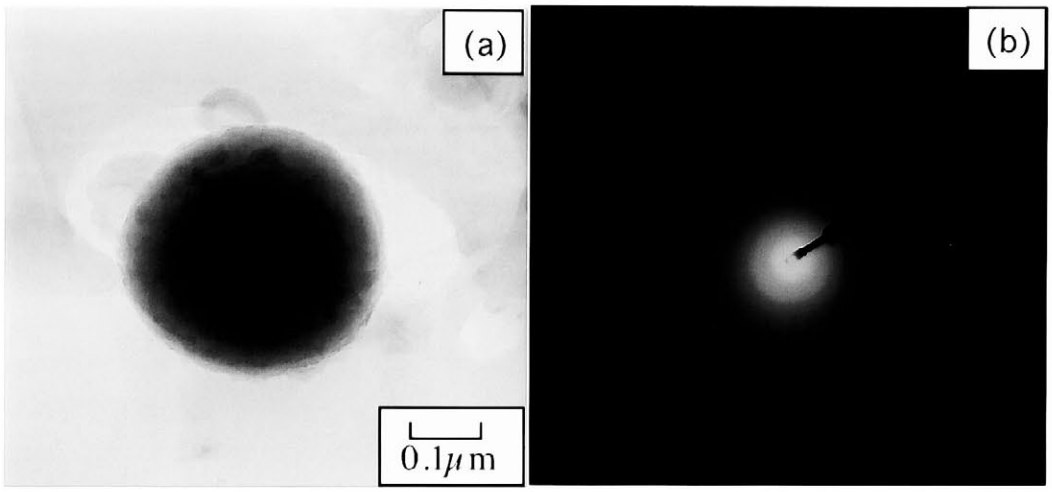

Fig. 5.6 (a) Spherical inclusion of amorphous silica in Sample 1-A maintained at 1873K for 60 minutes. The grey, spherical part shows the inclusion on the light grey carbon film.
(b) Electron diffraction pattern (halo pattern) of the amorphous silica in (a).

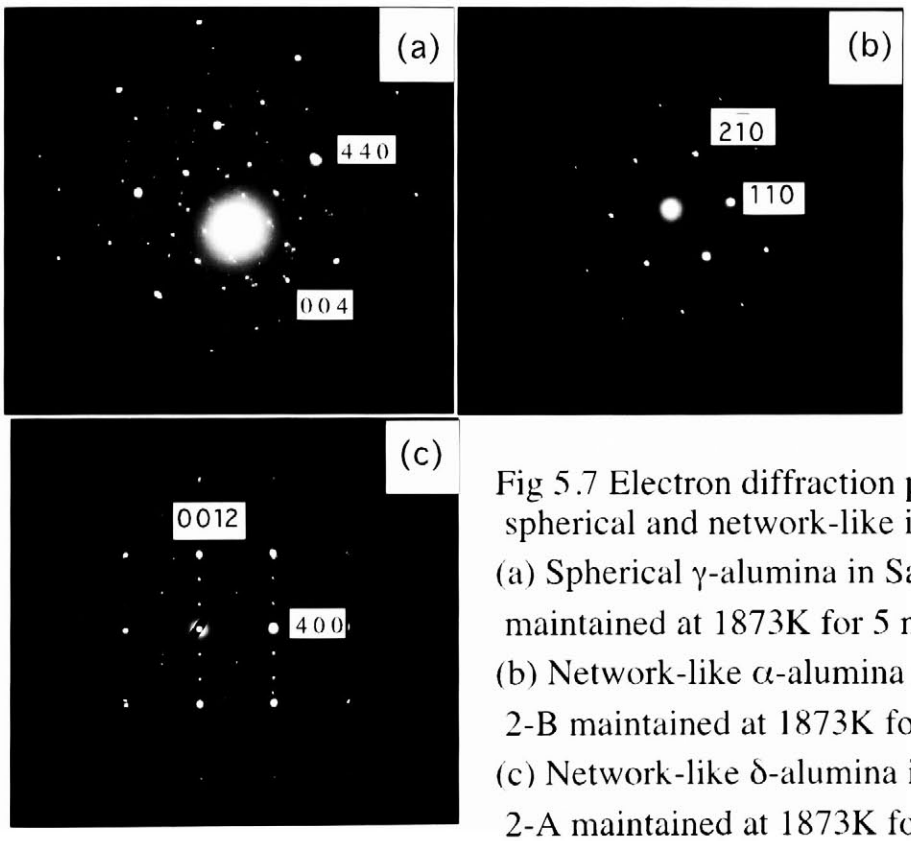

Fig 5.7 Electron diffraction patterns of spherical and network-like inclusions.
(a) Spherical γ-alumina in Sample 1-A maintained at 1873K for 5 minutes.
(b) Network-like α-alumina in Sample 2-B maintained at 1873K for 20 minutes.
(c) Network-like δ-alumina in Sample 2-A maintained at 1873K for 40 minutes.

Chapter 6 Thermodynamic Analysis on Metastable Alumina Formation in Aluminum-deoxidized Iron Based on Ostwald's Step Rule and Classical Homogeneous Nucleation Theories.

I. Introduction

The δ, γ, κ, and θ phases of alumina have been observed in aluminum-deoxidized iron.[1-7] In Chapter 5, the presence of unstable aluminas and amorphous silica inclusions formed during cooling of iron was reported.[1,2] However, the δ, γ, κ, and θ-aluminas are not stable at steelmaking temperatures and are metastable at ordinary temperatures, whilst the α-alumina is stable. Also, cristobalite is the stable form of silica at the steelmaking temperatures. It is not obvious why unstable alumina and amorphous silica are formed under these conditions.

Okubo et al.[7] thought that enthalpy evolved due to the heat of formation when an alumina particle is formed in liquid iron could force it to melt and, as a consequence, the alumina melt would be supercooled resulting in the solidification of unstable alumina. In contrast, Kusakawa et al.[8] reported that only 50 degrees centigrade temperature rise of steel would result from the heat of formation of alumina and thus there was no possibility of liquid alumina formation in the steel. However, Kiessling[9] reported the presence of glassy and partly-molten alumina inclusions. He considered that local overheating with high local temperature peaks resulted from the reaction between liquid aluminum and oxygen in steel at the surface of the steel and thus caused the melting of alumina.

According to Ostwald's Step Rule,[10,11] a supercooled liquid material, which shows polymorphism, solidifies first as an unstable (metastable) crystal and then gradually transforms into other polymorphs with lower chemical potentials in a step by step manner. Therefore, as Okubo et al. have stated,[7] once liquid alumina has formed in the liquid iron, it could subsequently solidify as unstable aluminas. Certainly, liquid alumina could be formed immediately after aluminum addition due to the local overheating as Kiessling reported.[9] However, it is unlikely that the alumina in bulk liquid iron would melt during the cooling process as a consequence of the heat of formation evolution due to the reaction between oxygen and aluminum which are already present as solutes in liquid iron, even if they are present in the supersaturated state. Furthermore, the temperature rise required for the melting of silica is also improbable, although the amorphous silica can easily form from liquid silica and nothing other than the liquid silica formation could explain the presence of amorphous silica.

Oxygen levels in aluminum-deoxidized liquid iron often exceed over equilibrium levels for solid α-alumina for a considerable time after aluminum deoxidation. The excess oxygen would be transformed into an alumina inclusion during the solidification process because the aluminum which is insoluble in acid is detected in the solidified iron. Therefore, the investigation of the excess oxygen is important in order to investigate the mechanism of alumina formation. Many researchers believe that the excess oxygen originates from supersaturated oxygen in the liquid iron. However, the present author have doubts as to why the oxygen and aluminum remain seperate and non-reactive in the liquid iron for a long time without forming a very stable alumina at 1873 K, and, in contrast, react and form alumina inclusions at lower

temperatures during cooling.

In an earlier report[12] and Chapter 2, the present author proposed the presence of alumina-associated compounds in the liquid iron in equilibrium with solid α-alumina, and developed an associated solution model. The model showed reasonable explanations for both the thermodynamic properties and the inconsistencies in the measurements obtained in various studies of liquid iron. Almost all the oxygen is present as oxygen-containing associated compounds. Thus the model does not consider the free oxygen in the usual concentration ranges of oxygen and aluminum in liquid iron. In Chapter 4 and in a previous article,[13] the present author applied this model to liquid iron containing excess oxygen. The results showed that the model could be applied to liquid iron with excess oxygen and the excess oxygen should originate, partly, from the suspension of fine alumina deoxidation products and partly, from the supersaturation of alumina-associated compounds.[13] The suspended aluminas could coalesce to form secondary inclusions during cooling and solidification process . Thus, the structure of the coalesced, secondary alumina depends on the original suspended alumina, which is the primary deoxidation product. Also, the supersaturated-alumina-associated compounds should agglomerate or precipitate on the suspended alumina and solidify as an alumina secondary inclusion. Thus, if the secondary alumina inclusion forms from the suspended alumina and supersaturated-associated compounds and does not form through a reaction between free oxygen and aluminum during cooling, then the heat of alumina formation reaction does not arise during cooling. Thus, another driving force to cause an alumina particle to form liquid alumina must be sought or another reason for unstabl-alumina formation is needed.

In the present study the formation of unstable alumina will be discussed on

the basis of the Ostwald's Step Rule,[10,11] and two homogeneous nucleation theories (namely, one in common use and a modified theory which follows the original equation of the homogeneous nucleation thoery[13]). In both homogeneous nucleation theories, the dependence of the interfacial free energy between liquid iron and alumina on oxygen concentration has been taken into account in different ways. In the latter theory, which was discussed in detail in Chapter 4 and in a previous report,[13] the Gibbs free energy change of parent iron phase has been considered.

II. Supersaturated State and Alumina Associated compound

Generally, a supersaturated state of oxygen means a supersaturation of aluminum and oxygen in relation to the state in equilibrium with α-alumina. The state in equilibrium with solid α-alumina is hereafter referred to as the equilibrium state. The $\mu^{s.s.}$, which is the sum of the chemical potential of aluminum and oxygen in a supersaturated state ($\mu_{Al}^{s.s.}$ and $\mu_{O}^{s.s.}$), is expressed by both the degree of supersaturation (S) and the chemical potential of solid α-alumina, μ_{α}°.

$$\mu^{s.s.} = 2\mu_{Al}^{s.s.} + 3\mu_{O}^{s.s.} = RT\ln S + 2\mu_{Al}^{e} + 3\mu_{O}^{e} = RT\ln S + 2\mu_{\alpha}^{\circ}, \qquad [6.1]$$

$$S = (a_{Al}^{s.s.})^2 \cdot (a_{O}^{s.s.})^3 \,/\, \left\{(a_{Al}^{e})^2 \cdot (a_{O}^{e})^3\right\}, \qquad [6.2]$$

where, μ_{Al}^{e} and μ_{O}^{e} are the chemical potentials of aluminum and oxygen in the equilibrium state, respectively. The $(a_{Al}^{s.s.})^2 \cdot (a_{O}^{s.s.})^3$ and $(a_{Al}^{e})^2 \cdot (a_{O}^{e})^3$ are the activity products of aluminum and oxygen in the supersaturated state, and in the equilibrium state, respectively.

If the alumina-associated compound is present in liquid iron in the supersaturated state, its chemical potential, $\mu_{a.s.}^{s.s.}$, can be written in the same manner as Eq. [6.1] since the mass action law should hold even in the

supersaturated state.

$$\mu_{a.s.}^{s.s.} = 2\mu_{\mathrm{Al}}^{s.s.} + 3\mu_{\mathrm{O}}^{s.s.}. \qquad [6.3]$$

Therefore, $\mu_{a.s.}^{s.s.}$ equals to $\mu^{s.s.}$. The $\mu_{a.s.}^{s.s.}$ can be also written as follows.

$$\begin{aligned}\mu_{a.s.}^{s.s.} &= \mu_{a.s.}^{\circ} + RT\ln a_{a.s.}^{s.s.} \\ &= \mu_{a.s.}^{\circ} + RT\ln a_{a.s.}^{e} + RT\ln S_{a.s.} \\ &= \mu_{a.s.}^{e} + RT\ln S_{a.s.}, \end{aligned} \qquad [6.4]$$

where, $S_{a.s.}$ $(= a_{a.s.}^{s.s.} / a_{a.s.}^{e})$, $a_{a.s.}^{s.s.}$, $a_{a.s.}^{e}$ and $\mu_{a.s.}^{e}$ expresses the degree of supersaturation, activity in the supersaturated state , activity in the equilibrium state, and chemical potential in the equilibrium state, respectively, of alumina-associated compound. The subscript a.s. means alumina-associated compound. The $\mu_{a.s.}^{e}$ equals to μ_{α}° because, in the equilibrium state, the alumina-associated compound is in equilibrium with solid α-alumina. Thus, the two supersaturation degrees, S and $S_{a.s.}$, are also equal. This can also be deduced from the next equation.

$$\begin{aligned}S_{a.s.} &= a_{a.s.}^{s.s.} / a_{a.s.}^{e} \\ &= \{K_{a.s.}(a_{\mathrm{Al}}^{s.s.})^2 \cdot (a_{\mathrm{O}}^{s.s.})^3\} / \{K_{a.s.}(a_{\mathrm{Al}}^{e})^2 \cdot (a_{\mathrm{O}}^{e})^3\} \\ &= S, \end{aligned} \qquad [6.5]$$

where, $K_{a.s.}$ is the equilibrium constant for the formation reaction of alumina associated compound.

As has been discussed above, no matter how the real supersaturated state might be, the $\mu^{s.s.}$ represents the chemical potential of the supersaturated state.

III. Results and Disscussion based on Various Rule and Theories

A. Ostwald's Step Rule

In Fig. 6.1, the chemical potential differences ($\mu_i^\circ - \mu_\alpha^\circ$) between unstable aluminas (δ, γ and κ-aluminas; μ_i°) and α-alumina (μ_α°) are shown as functions of temperature. In Fig. 6.1, the $\mu_\ell^\circ - \mu_\alpha^\circ$ (μ_ℓ°: chemical potential of liquid alumina) is also plotted. The value of $\mu_\ell^\circ - \mu_\alpha^\circ$ from the melting point to 1700K indicates the value of supercooled liquid alumina. All the chemical potentials are cited from the JANAF Thermochemical Tables.[14] Apparently, the μ_ℓ° is larger than any other chemical potentials, μ_i°. Judging from Fig. 6.1 and Ostwald's Step Rule, one can estimate that the supercooled liquid alumina solidifies into δ, γ or κ-alumina since the chemical potential of liquid alumina is larger than those of δ, γ or κ-alumina.

Ostwald also pointed out that a supersaturated state created unstable or metastable states.[10] Thus, the Step Rule should be applied for the supersaturated states. The $\mu^{s.s.}$-μ_α° values at S=100, 50, 10 and 5 are plotted in Fig. 6.1. All the $\mu^{s.s.}$ values are larger than the chemical potentials of various aluminas. Therefore, it shows that, not only the δ, γ and κ-aluminas but also the liquid alumina could be formed from the supersaturated states. The liquid alumina formed will solidify as δ, γ, κ or α-alumina. A supersaturated state will arise not only at a final stage after deoxidation but also at a stage of initial deoxidation process. Thus, above results show the possibility of forming unstable and liquid alumina in both stages without involving the process of temperature rise. However, Ostwald's Step Rule is an empirical one. It should be inspected on the basis of nucleation theory.

B. Classical Homogeneous Nucleation Theory

The nucleation rate can be calculated from the following equations based on the classical, simplified homogeneous nucleation theory[15,16] which is often used

when considering the nucleation of inclusions.

$$I = A\exp\{-(\Delta g^* + \Delta g_D)/kT\}, \quad [6.6]$$

$$\Delta g^* = 16\pi\sigma_{Fe-i}{}^3 M^2 / \{3\rho_i{}^2(\mu^{s.s.} - \mu_i^\circ)^2\}, \quad [6.7]$$

$$A = n_i^*(\sigma_{Fe-i}/kT)^{1/2}(2v_i/9\pi)^{1/3} n(kT/h), \quad [6.8]$$

where Δg_D is the Gibbs free energy of activation for transporting a molecule across the interface and is neglected in calculation because this term is unknown and is thought to be very small in comparison with Δg^*. The Δg^* is the Gibbs free-energy change for the formation of a critical nucleus in which the Gibbs free-energy term of parent iron phase is ignored. In Eq. [6.7], ρ_i, μ_i° and M are the density of critical nucleus of various aluminas, i (i : α, δ, γ or liquid-alumina), the standard chemical potential of i, and the atomic weight of alumina, respectively. In Eq. [6.8], n_i^* v_i and n are the number of molecules on the surface of the i's critical nucleus, the volume per molecule of i's critical nucleus, and the number of molecules per mole of parent phase, respectively. The n^*, n and v_i values are written as follows:

$$n_i^* = 4\pi(r^*)^2 / \{M/(\rho_i N)\}^{2/3}, \quad [6.9]$$

$$n = (6\cdot 10^{-6} M_{Fe}/3M_O)\, S\, N, \quad [6.10]$$

$$v_i = (M/\rho_i)/N, \quad [6.11]$$

where, n is assumed to be one third of the total number of oxygen atoms in the iron, because an alumina molecule is constituted of three oxygen atoms. As the oxygen content in the equilibrium state is around 0.0006 mass%, the value of n is expressed by Eq. [6.10]. The M_{Fe}, M_O and N are the atomic weights of iron and oxygen and the Avogadro's Constant, respectively. The density of liquid alumina can be expressed as a function of temperatur (T),

($\rho_l = 5.34 - 1.15 \cdot 10^{-3} T$ (g·cm^{-3}), where T is in K), which was derived from a figure in the data book.[17] The densities of α, δ or γ-alumina phases (ρ_γ, ρ_δ, ρ_γ) derived from the ASTM card were used here but the density of κ-alumina could not be found.

The interfacial free energy values between various aluminas and liquid iron, σ_{Fe-i}, are needed for the calculation of nucleation rate. The present author have already proposed a correlation between the interfacial free energies of various metals and oxides, and the molar enthalpy values of oxides (Fig. 4.1).[13] The interfacial free energies between various metals and oxides, $\sigma_{metals-oxide}$, can be expressed by linear regression analysis (Eqs. [4.4], [4.5], and [4.6]).[13] Thus, the interfacial free energies between liquid iron and various aluminas, σ_{Fe-i}, can be expressed as follows,

$$\sigma_{\mathrm{Fe}-i} = \sigma^*_{\mathrm{Fe}-i} N^{-1/3} V_i^{-2/3}, \qquad [6.12]$$

$$\sigma^*_{\mathrm{Fe}-i} = -6215 + 0.1210(-H_i^\circ) \quad \text{(J/mol)}, \qquad [6.13]$$

$$H_i^\circ = \Delta H^\circ_{i,\text{at 298K}} + \int_{298}^{T} Cp_i dT, \qquad [6.14]$$

where subscript i means each alumina. The $\sigma_{\mathrm{Fe}-i}$ calculated from the molar enthalpies of aluminas, H_i°,[14] using Eqs. [6.12]and [6.13] are shown as functions of temperature in Fig. 6.2. However, the values of $\sigma_{\mathrm{Fe}-i}$ in Fig. 6.2 refer to those for alumina having zero curvature and oxygen-free iron. The interfacial free energy should change according to the change of nuclear curvature (or nuclear radius) and oxygen content in liquid iron. In the present calculation, it was assumed that all the interfacial free energies had similar dependence on nuclear radius and oxygen content. This assumption means that the difference itself between $\sigma_{\mathrm{Fe}-\alpha}$ and $\sigma_{\mathrm{Fe}-i}$ at a certain temperature, which is

derived from Fig. 6.2, is constant and does not change according to the nuclear radius and oxygen content. In other words, each σ_{Fe-i} can be determined at any value of the $\sigma_{Fe-\alpha}$, even though $\sigma_{Fe-\alpha}$ and σ_{Fe-i} change according to the nuclear radius and oxygen content. Thus, σ_{Fe-i} can be represented as a function of $\sigma_{Fe-\alpha}$, and each nucleation rate can be calculated as a function of $\sigma_{Fe-\alpha}$. The calculated nucleation rates from a supersaturated state (S=50) are shown in Fig. 6.3 as functions of $\sigma_{Fe-\alpha}$.

Figure 6.3 shows that the nucleation rates of liquid, δ and γ -alumina are larger than that of α-alumina. For a value of $\sigma_{Fe-\alpha}$= 0.8N/m, the nucleation rates of liquid, δ and γ -alumina are 10^{17}, 10^{7} and 10^{8}, respectively, greater than that for α-alumina.

The above-mentioned results represent the nucleation rates at any value of the interfacial free energy of α-alumina even if it depends on the oxygen content of liquid iron and the curvature of nucleus. Furthermore, the estimated interfacial free energies shown in Fig. 6.2 should be appropriate. The present author were unable to find any other methods for the reliable estimation of interfacial free energies. However, the homogeneous nucleation theory used in the above calculation does not include a term for the Gibbs free-energy change of parent iron phase. Thus, the dependence of nucleation rate on oxygen and aluminum contents cannot be discussed.

C. Modified Classical Homogeneous Nucleation Theory[13]

The original homogeneous nucleation theory includes a term for the Gibbs free energy of the parent phase. In this section, an influence of the Gibbs free-energy change of liquid iron phase was considered in calculation of nucleation rates. Furthermore, the dependence of interfacial free energy on

both the curvature and oxygen content is introduced.

The Gibbs free-energy change of the 1 mol system can be expressed by the following equation.

$$\Delta G = \Delta G_S + \Delta G_A + \Delta G_B = n_0 \Delta g, \qquad [6.15]$$

where n_0 is the total number of nuclei in a 1 mol system and Δg is the Gibbs free-energy change for the formation of a nucleus. The first term, ΔG_S, which arises from the newly formed interface between alumina and liquid iron, is expressed as follows.

$$\Delta G_S = n_0 4\pi r^2 \sigma_{\mathrm{Fe}-i}. \qquad [6.16]$$

The ΔG_A represents the Gibbs free-energy change of alumina nuclei's formation expressed as follows,

$$\Delta G_A = -n_0 m(\mu^{s.s..} - \mu_i^{\circ}) \ , \qquad [6.17]$$

while m shows the molar number of a nucleus and equals $(4/3)\pi r^3 / V_i$.

In the case of α-alumina nucleation, the following equation can be deduced.

$$\Delta G_A = -n_0 mRT \ln\left[\left\{(a_{\mathrm{Al}}^{(1)})^2 (a_{\mathrm{O}}^{(1)})^3\right\} / \left\{(a_{\mathrm{Al}}^{e})^2 (a_{\mathrm{O}}^{e})^3\right\}\right] = -n_0 mRT \ln S. \qquad [6.18]$$

The term ΔG_B is the Gibbs free-energy change of the parent liquid iron phase excluding the aluminum and oxygen consumed during nucleation. This term is expressed by the activities of aluminum, oxygen and iron before nucleation and after nucleation.

$$\Delta G_B = RT\{(x_{\mathrm{Al}} - 2n_0 m)\cdot \ln a_{\mathrm{Al}}^{(2)} + (x_{\mathrm{O}} - 3n_0 m)\cdot \ln a_{\mathrm{O}}^{(2)} + x_{\mathrm{Fe}} \cdot \ln a_{\mathrm{Fe}}^{(2)}\}$$
$$-RT\{(x_{\mathrm{Al}} - 2n_0 m)\cdot \ln a_{\mathrm{Al}}^{(1)} + (x_{\mathrm{O}} - 3n_0 m)\cdot \ln a_{\mathrm{O}}^{(1)} + x_{\mathrm{Fe}} \cdot \ln a_{\mathrm{Fe}}^{(1)}\}. \qquad [6.19]$$

The superscripts (1) and (2) represent the phases before nucleation and after nucleation respectively, and x_{Al}, x_{O} and x_{Fe} are the molar fractions of aluminum, oxygen and iron, respectively. The value of n is assumed to be one third of the total number of oxygen atoms in liquid iron since an alumina

molecule containes three oxygen atoms. Thus,

$$n = Nx_O / 3. \qquad [6.20]$$

In order to calculate ΔG, the interfacial free energy, which depends on oxygen content and curvature of alumina nucleus, should be evaluated. The dependence of interfacial free energy between liquid iron and α-alumina on oxygen content was estimated in Chapter 4 (Eq. [4.7]) and can be written as follows.[13]

$$\sigma_{Fe-\alpha} = 2.328 - 43.18[mass\%\ \underline{O}] - 708.6[mass\%\ \underline{O}]^2 \quad (N/m). \qquad [6.21]$$

Value for liquid, δ and γ-alumina were estimated by assuming the same dependence on oxygen content as that of α-alumina. It is shown in the next equation.

$$\sigma_{Fe-i} = 2.328 + D - 43.18[mass\%\ \underline{O}] - 708.6[mass\%\ \underline{O}]^2 \quad (N/m), \qquad [6.22]$$

where, D is the interfacial free-energy difference between α-alumina and other alumina polymorphs at 1873K in Fig. 6.2. The dependence of the interfacial free energy on the curvature of alumina of small nucleus, σ°_{Fe-i}, can be assumed from the next equation.[12,18]

$$\sigma^{\circ}_{Fe-i} / \sigma_{Fe-i} = (1/V_i)/\{(2\Gamma/r) + ((1/V_i)\}\ , \qquad [6.23]$$

where Γ is the surface excess and is assumed to be $\Gamma = N^{-1/3}V_i^{-2/3}$.

The activities of constituents in iron were calculated on the basis of the associated solution model.[12,18]

The calculated values of ΔG are shown in Fig. 6.4 for nucleation in liquid iron containing initial contents of 0.1 mass% $\underline{Al}$ and 0.0200 mass% $\underline{O}$ at 1873K for the case where $n_0 = 10^{16}$. Figure 6.5 shows σ°_{Fe-i} ($=\sigma^{\circ}_{Fe-\alpha}$, $\sigma^{\circ}_{Fe-\delta}$, $\sigma^{\circ}_{Fe-\gamma}$ and $\sigma^{\circ}_{Fe-\ell}$) values change according to the growth of the nuclei and the accompanying decrease of oxygen content. The changes in oxygen content for

the process and the $\sigma_{Fe-\alpha}$ calculated from the oxygen content are also shown in Fig. 6.5. The ΔG is the n_0 times of Δg, thus, the maximum values of ΔG represents the n_0 times of Δg^*. As pointed out in the previous report, α-alumina can nucleate from the liquid iron containing 0.1 mass% Al and 0.0200 mass% O. From Fig. 6.4, it is clear that the maximum values of ΔG of α, δ, γ, and liquid-aluminas all display similar values and all the aluminas have a chance of nucleating . The value for δ-alumina is the smallest, which indicates that δ-alumina is the easiest to nucleate. In Fig. 6.6, the ΔG calculated for the liquid iron with initial contents of 0.1 mass% Al and 0.0220 mass% O are shown. The result indicates that the maximum value associated with liquid alumina is the smallest.

The nucleation rates calculated on the basis of Eqs. [6.6]-[6.23] are shown in Table 6.I. The Table 6.I shows that α, γ and liquid-alumina all nucleate at a similar rate and the rate of δ-alumina is the largest in the case of liquid iron with initial contents of 0.1 mass% Al and 0.0200 mass% O. In case of 0.1 mass% Al and 0.0220 mass% O initial content, the situation is entirely different and the nucleation rate of liquid-alumina has the largest value and that of α-alumina has the smallest value. The content of 0.0200 mass% O in liquid iron is located just above the critical point of supersaturation at 0.1 mass% Al (about 0.0150 mass% O at 1873K).[13] Therefore, the liquid and unstable alumina can nucleate easily from the iron with composition beyond the critical point and the liquid alumina will finally solidify as an unstable or α-alumina inclusion. In practice, the nucleation following the aluminum addition in liquid steel would proceed in the same manner as the above nucleation process from the liquid iron which exceeds the critical point. Therefore, many of the primary inclusions were

found to be composed of the unstable alumina.

From the results of the previous calculation,[13] the nucleation of α-alumina is scarce at any oxygen content below the critical point . The nucleation, with respect to the liquid and the unstable aluminas, will be more difficult below the critical point. However, any temperature decrease will bring about an oxygen decrease of the critical point. In Table 6.I, the nucleation rates at 1800K and 1700 K of various aluminas with 0.0150 mass% O are shown. The table shows that δ and α-alumina can be formed at 1800 K and 1700K, due to the decrease of oxygen of the critical point, but there would be difficulties in the formation of liquid and γ–alumina. Moreover, the oxygen solubility in δ–iron at 1720K is about 0.0150 mass% O and it decreases to 0.0082 mass% O at 1663 K.[19] Furthermore, in γ-iron, the oxygen solubility is less than 0.0001 mass% O according to the phase diagram due to O. Kubaschewski.[19] Therefore, for supercooling conditions, the oxygen (or supersaturated-alumina-associated compound) in liquid iron at the solidification front will increase owing to the decrease of oxygen content in solid iron. The liquid and unstable alumina nucleation will be accelerated again in the supercooling process.

The results based on the modified homogeneous nucleation theory also depend on the values of the interfacial free energies. Especially, Eq. [6.23] is uncertain for the case where a nucleus containes only a few molecules. However, as mentioned in Chapter 4 and a previous report,[13] the calculated nucleation rates of α-alumina for various oxygen and aluminum contents in liquid iron are consistent with experimental trends. The present results calculated for unstable and liquid alumina nuclei could also reflect the real trends.

IV. Discussion

A. Network-like and Coral-like Inclusions

The network-like inclusions observed in aluminum-deoxidized iron which was solidified ultra rapidly or quenched into a copper mold sometimes extend to a wide region like a plane.[1,2] Shibata et al. reported, from in-situ observations of alumina inclusions with a confocal laser scanning microscope that fine alumina particles tend to be pushed by advancing interface between the melt and cellular crystal.[20] If liquid alumina is formed during cooling before solidification front, it would tend to be pushed from the interface and the following mechanism would occur. The several fine alumina drops, which are formed in the solidification front, are pressed by the iron grains with the advance of the front, and finally, gather at the grain boundary, where they are pressed and solidified into a network-like plane connected with each other.

However, the network-like and coral-like inclusions in the sample quenched in water were roundish in contrast to those with angular shape which were observed in a sample solidified ultra rapidly or quenched in copper mold. The roundish coral-like inclusions seemed to be the result of multiple union of liquid spherical inclusions with high viscosity. The network-like inclusions in the same sample seemed to be formed when several coral-like inclusions were superimposed upon one another.[2] Thus, in a sample quenched in water, the spherical liquid inclusions formed during cooling would have time to float upward, collide and coalesce with each other in liquid iron, since the cooling speed is rather slow, and finally, they could solidify as the network-like or coral-like inclusions. The above process for the network-like or coral-like inclusion in the sample quenched in water might occur during the early stage of

aluminum deoxidation process in liquid iron with a composition which exceeded the critical point of supersaturation. If the inclusion is formed at this stage, it should be the primary phase.

The above elucidation of the morphology of the network-like and coral-like inclusions supports the significant formation of liquid alumina. If the liquid alumina is present, it will act as a binder of solid alumina particles which would result in a large alumina cluster. Thus, the care must be taken at every place where the supercooling or the reoxidation may occur, for instance, around the wall of mold, if cluster formation is to be prevented.

B. Possibility of Liquid Alumina Formation

The Figs. 6.1, 6.3, 6.4, and 6.6 and Table 6.I indicate the possibility of liquid alumina formation from the supersaturated state without a temperature rise exceeding the melting point of alumina by the heat of formation evolution. Although established evidence for the presence of liquid alumina is currently insufficient, there is a strong possibility of liquid formation. For instance, the spherical inclusion of amorphous silica can not be explained without the formation of liquid silica. The supersaturated silicon and oxygen, or the silica-associated compound in liquid copper participate as a form of liquid silica during cooling, and it subsequently transforms into amorphous silica. This process will be discussed in Capter 7

From the standpoint of controlling the morphology of alumina, it is an important topic as to whether the liquid alumina is present or not. More detailed investigations and deliberations are necessary if the formation of liquid alumina is to be verified.

V. Conclusion

The process of unstable alumina (δ, γ, κ, and θ-alumina) formation has been discussed on the basis of the Ostwald's Step Rule[10,11] and two homogeneous nucleation theories. One of the homogeneous nucleation theories is the simplified in common use whereas the other is the modified theory in which the Gibbs free-energy change of parent iron phase is taken into consideration. All the theories show the possibility of both unstable alumina and liquid alumina being formed. The details are follows;

The chemical potentials of supersaturated states, $\mu^{s.s.}$ ($= 2\mu_{Al}^{s.s.} + 3\mu_{O}^{s.s.} = RT\ln S + 2\mu_{\alpha}^{\circ}$), with various degrees of supersaturation, S (=100, 50, 10 and 5), were larger than any chemical potential of δ, γ, κ and liquid alumina . From the standpoint of the Ostwald's Step Rule, this result indicates that unstable aluminas or liquid alumina could be formed from liquid iron in the supersaturated state.

From the former simplified homogeneous nucleation theory, it was concluded that the nucleation rate of the liquid, δ and γ–alumina were larger than α-alumina; the nucleation rate of liquid-alumina was greatest followed by those for δ and γ–alumina.

From the modified homogeneous nucleation theory[13], in which the dependence of interfacial freee energy on nucleus size and oxygen contents in liquid iron is considered in apparant form, one can calculate nucleation rate of any alumina at any content of oxygen and aluminum in liquid iron. It was found that the nucleation of liquid and unstable aluminas from the liquid iron

containing 0.1 mass % Al and an oxygen content exceeding the critical value of supersaturation (about 0.0150 mass% O at 1873K) were possible in addition to α-alumina. In contrast, the nucleation of every alumina is rare with oxygen contents below the critical value. However, the nucleation of δ and α-alumina began again during cooling process of iron due to the reduction of the critical oxygen content with decrease in temperature. When liquid iron is supercooled strongly, the nucleation rate of liquid and unstable alumina would be accelerated due to the oxygen enrichment at the solidification front resulting from the lower solubility of oxygen in solid iron.

The morphology of the network-like and coral-like inclusion can be described by assuming that liquid alumina is formed. If liquid alumina is present, it will act as the binder of alumina solid particles and create large alumina clusters. The liquid alumina is a key point for considering alumina morphology and its control.

References

1. K.Wasai and K.Mukai: The Final Report of Ultra Clean Steel Research Group, Progress in Research on Ultra Clean Steel -Fundamental and Applied Aspects- (1999), 3, No.9511, ISIJ. Japan.
2. K.Wasai and K.Mukai: ISIJ. Int., **42**(2002), 459.
3. N.Iwamoto: Tetsu-to-Hagane, **58**(1972), 787.
4. F.Honda and K.Hirokawa: Tetsu-to-Hagane, **60**(1974), 287.
5. S.Watanabe, K.Takano, K.Moriya, Y.Tu and Y.Shiroishi: Tetsu-to-Hagane, **65**(1979), 383.

6. A.Adachi, N.Iwamoto and Y.Ueda: Tetsu-to-Hagane, **51**(1965), 1617.

7. M.Okubo, Y.Miyashita and R.Imai: Tetsu-to-Hagane, **54**(1968), S59.

8. T.Kusakawa, Y.Shiohara and S.Araki: Tetsu-to-Hagane, **64**(1978), 2129.

9. R, Kiessling: Non-metallic inclusions in steel Part 3, Second Edition (1978), 24, The Metals Society.

10. W. Ostwald: Z.Phy.Chem., **22**(1897), 289.

11. H.Singu and K.Ishihara: Bulletin Japan. Inst. Metals, **25**(1986), 16.

12. K.Wasai and K.Mukai: J Japan Inst. Metals, **52**(1988), 1088.

13. K. Wasai and K.Mukai: Metall and Mater. Trans. B, **30B**(1999), 1065.

14. JANAF Thermochemical Tables, 1974·1975·1978 Supplements Ed by M.W.Chase et al., HorikoshiLaboratory, (1980).

15. D.Turnbull and J.C.Fisher: J.Chem.Phys., **17**(1949), 71.

16. J.H.Hollomon and D.Turnbull: Progr.in Met.Phys., **4**(1953), 342.

17. Handbook of Physico-chemical Properties at High Temperatures:edited by Y. Kawai and Y.Shiraishi, (1988), 24.

18. R.Defay and I.Prigogine: Surface Tension and Adsorption, Translated by D.H.Everett, John Willey & Sons Inc., New York, (1966), 319-320.

19. O.Kubaschewski: IRON-Binary Phase Diagrams, Springer-Verlag, Berlin / Heiderberg, and Verlag Staahleisen mbH, Düsseldorf, (1982), 79-82.

20. H.Shibata, H.Yin, S.Yoshinaga, T.Emi and M.Suzuki: ISIJ Internat., **38**(1998), 149.

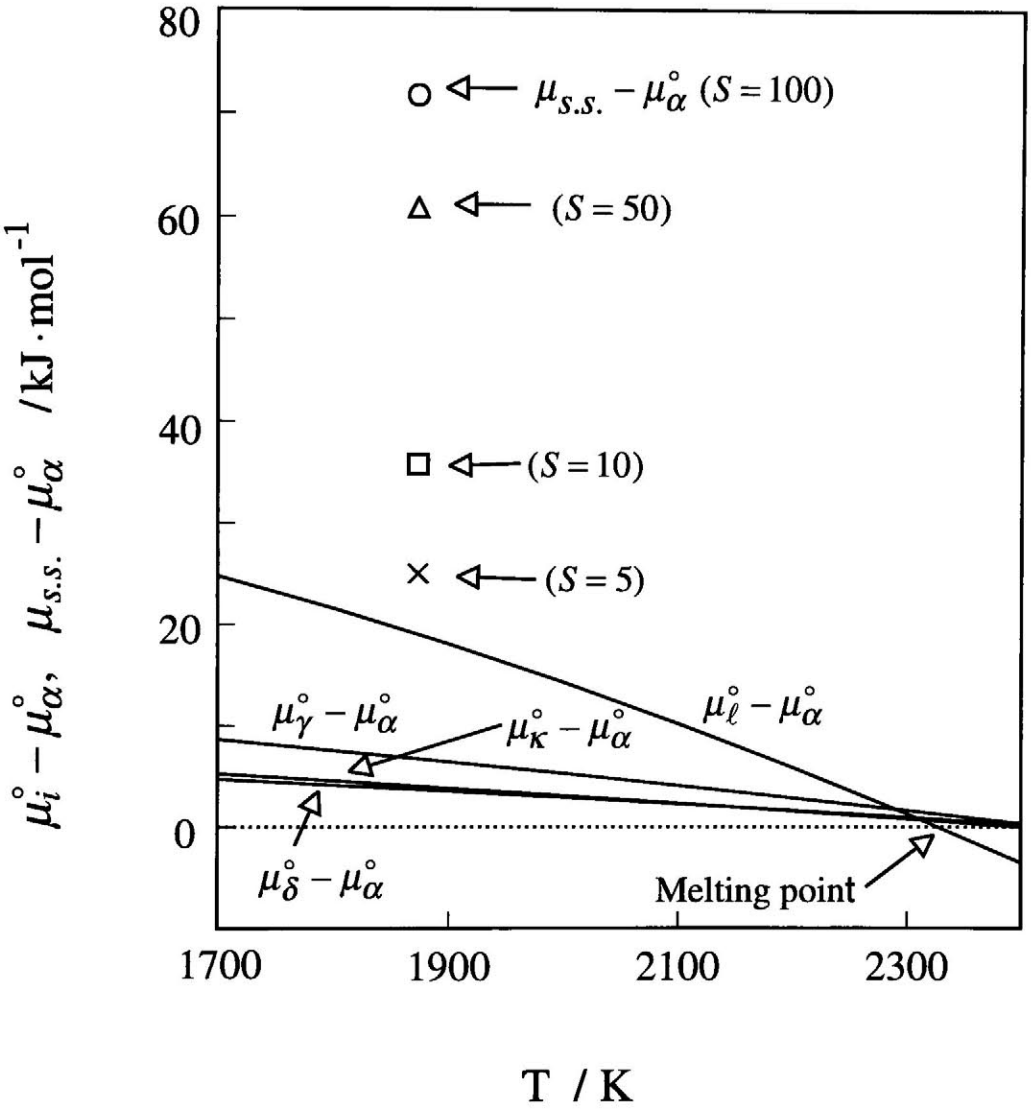

Fig. 6.1 Chemical potentials of various aluminas and supersaturated states.

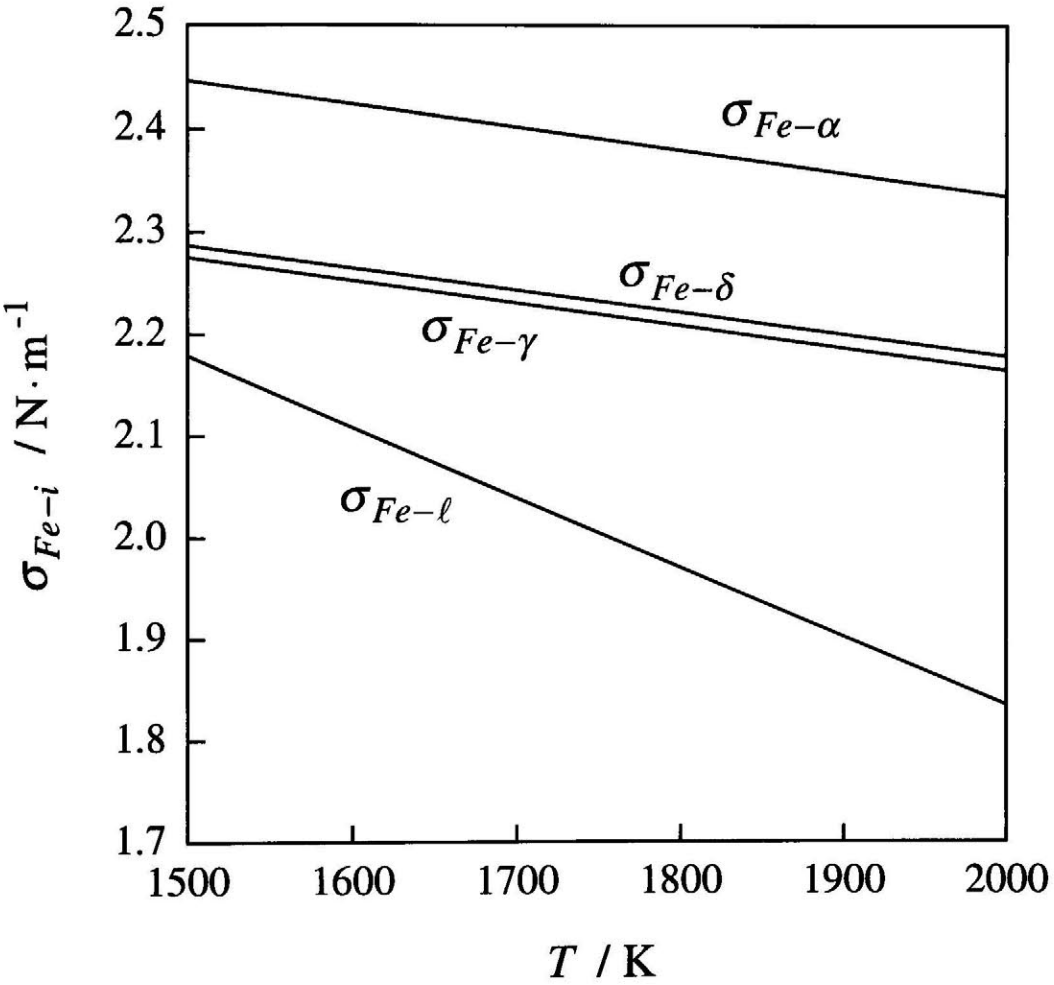

Fig. 6.2 Temperature dependence of interfacial free energies between oxygen-free liquid iron and various aluminas.

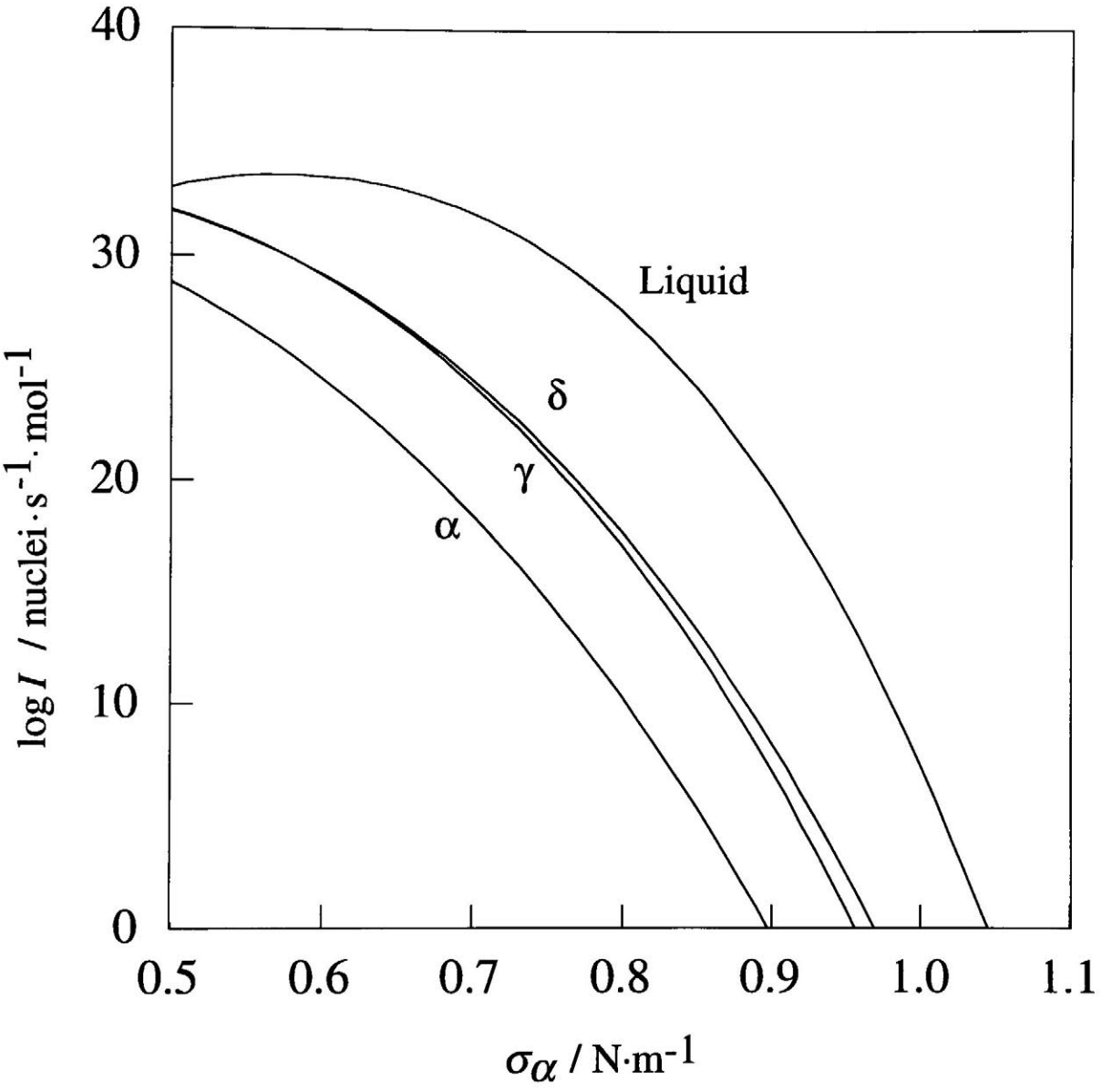

Fig. 6.3 Nucleation rates of various aluminas.

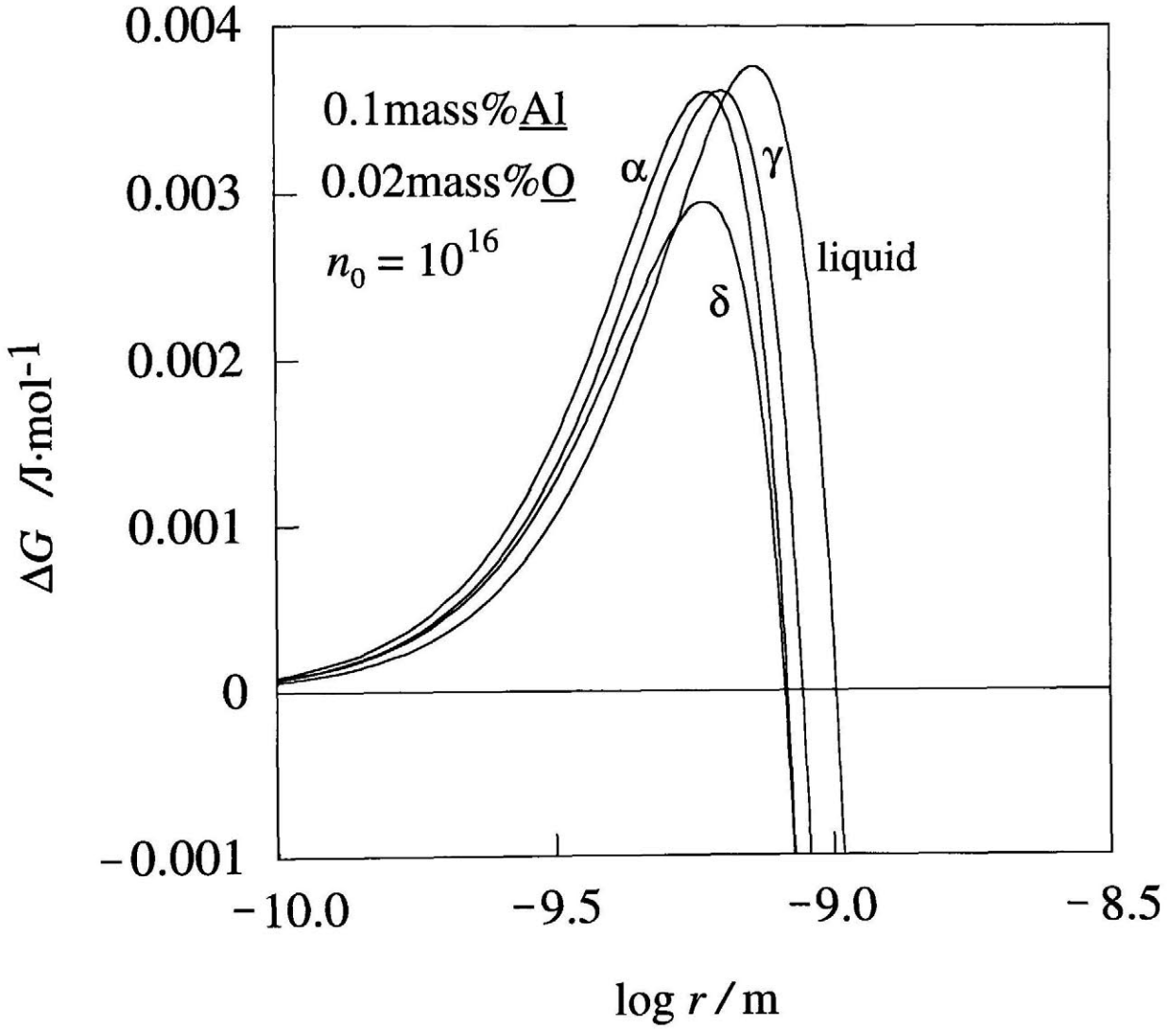

Fig. 6.4 Gibbs free energy changes of various aluminas for 0.02 mass%O and 0.1 mass%Al initial contents.

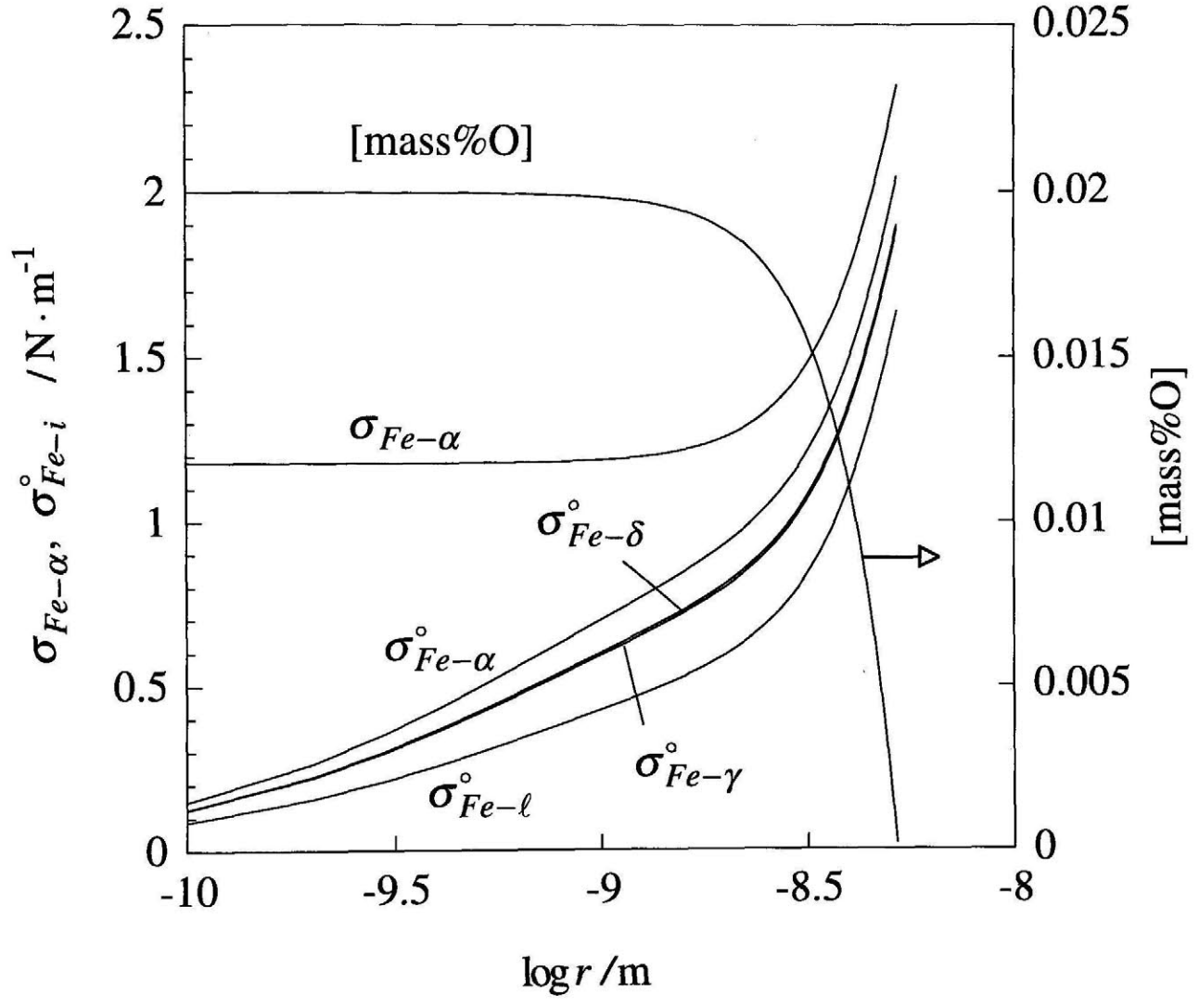

Fig. 6.5 Interfacial free energy changes of various aluminas and oxygen content change in the nucleation process started from the liquid iron of initial 0.02 mass % O and 0.1 mass % Al contents.

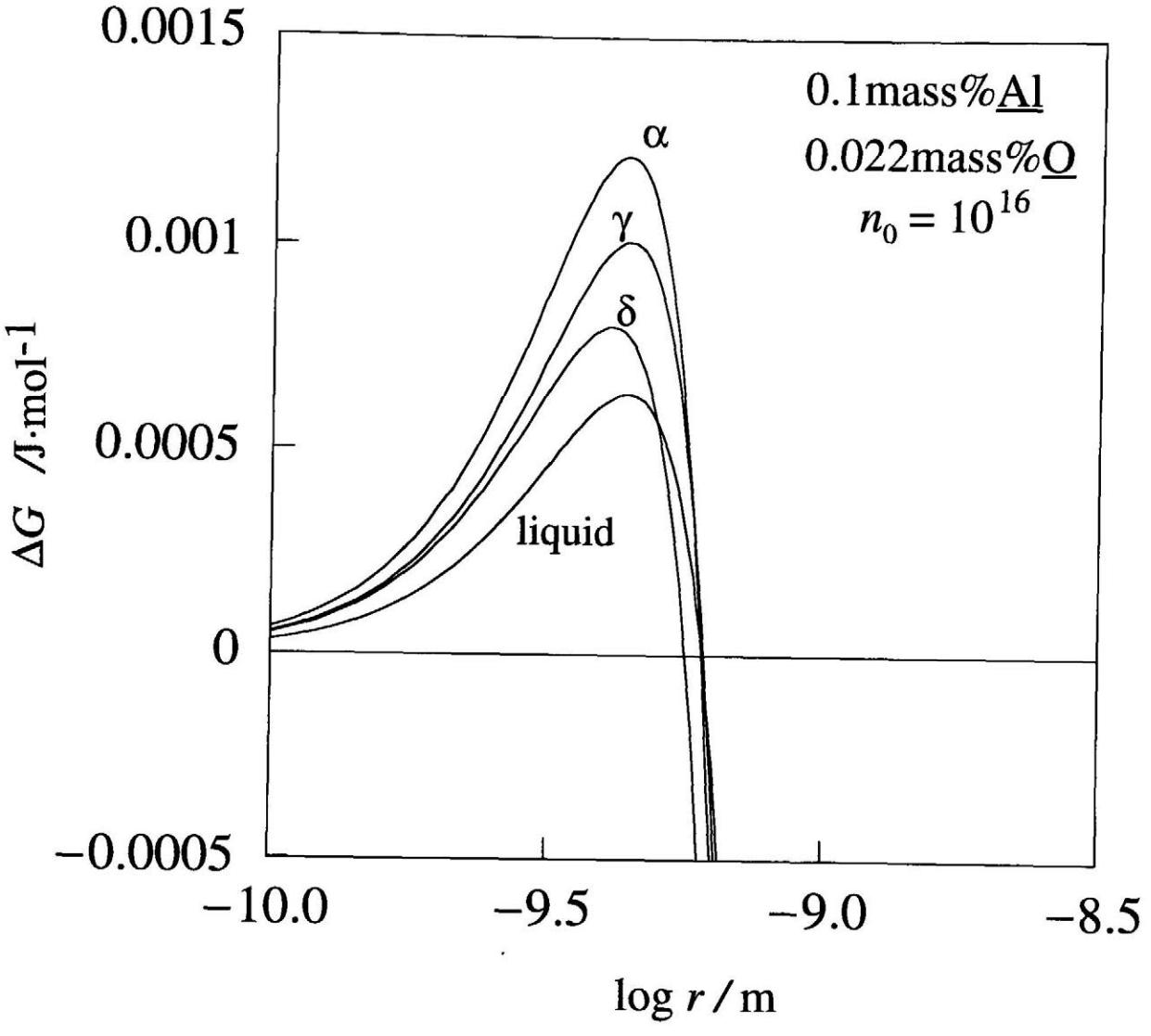

Fig. 6.6 Gibbs free energy changes of various aluminas for 0.022 mass%O and 0.1 mass%Al initial contents.

Table 6.I The rate of nucleation for various contents of oxygen and temperature at 0.1 mass % Al.

Species	Rate of Nucleation (nucleus·mol^{-1}·s^{-1})			
	1873K		1800K	1700K
	0.02 mass% O	0.022 mass% O	0.015 mass% O	0.015 mass% O
α	10^{29}	6×10^{32}	5×10^{9}	8×10^{18}
δ	10^{30}	2×10^{33}	6×10^{8}	10^{18}
γ	10^{29}	10^{33}	0	5×10^{13}
ℓ	7×10^{28}	4×10^{33}	0	0

Chapter 7 Mechanism of Formation of Amorphous Silica Inclusion in Silicon-deoxidized Copper

I. Introduction

In aluminum-deoxidized iron alloy, not only the stable α phase but also unstable δ, γ, κ and θ phases of alumina inclusion have been observed.[1-6] Similarly, amorphous silica and unstable silica inclusion have been observed in silicon-deoxidized iron although cristobalite is the stable form of silica at steel making temperatures.[2] Why the unstable aluminas and silicas were formed under steelmaking condition has been unclear. Recently, secondary inclusions of δ and γ -alumina , and amorphous silica inclusion were observed in aluminum-deoxidized iron at 1873K by the present author.[7] Analyses on the basis of Ostwald' Step Rule and two homogeneous nucleation theories showed that the nucleation of unstable alumina could occur from the supersaturated state of liquid iron.[8] The analyses also indicated the possible formation of liquid alumina inclusion from the supersaturated state of liquid iron. Through a similar mechanism for the unstable and liquid alumina formation, the unstable and liquid silica inclusions would be formed.

Liquid silica easily transforms into amorphous silica with cooling. Therefore, the presence of amorphous silica is strong evidence of the formation of liquid silica. Seeing that the steel-making temperatures around 1873 K are only about 120K lower than the melting point of silica (1996 K), the liquid silica inclusion might be formed through melting of silica deoxidation product immediately after silicon-deoxidation due to the heat of formation evolution. However, amorphous silica inclusion was observed by the present author in the

solidified iron that was deoxidized by aluminum and maintained at 1873K for 60 minutes after deoxidation.[7] There was no silica source other than silica impurity in alumina crucible in which the liquid iron alloy was charged. The silica impurity in the alumina crucible should have been dissolved into the liquid iron. However, after the dissolution of the silica, subsequent forming of solid silica inclusion in the iron, and its melting and solidifying to provide the final amorphous silica inclusion, could not happen at constant temperature of 1873K. Therefore, liquid silica inclusion was probably formed directly in the liquid iron alloy during cooling without temperature rise, and subsequently, solidified as the secondary amorphous silica inclusion. Still, at the current stage, clear evidence of the formation of secondary liquid silica inclusion as well as that of secondary liquid alumina inclusion is not obtained. Thus, an experiment of silicon-deoxidation for copper at 1423K was performed in the present study. The melting point of copper is considerably lower (1356K) than that of iron. The temperature of 1423K is 573 K lower than the melting point of silica[9] and 20 K lower than the glass transition temperature of silica (1443K[10]). Further, copper is a good heat conductor. If amorphous silica inclusion was observed in the copper, it would be satisfactory evidence of the formation of liquid silica without temperature rise. It would also support the formation of secondary liquid silica and alumina inclusions in iron alloy.

II. Experimental Method

A. Preliminary Experiment

Mixed acid of nitric acid and hydrochloric acid (HCl: H_2O: HNO_3 = 10:10:2) was used for dissolution of the copper samples for preparation of TEM specimens. However, silicon in the copper might form amorphous silica during dissolution process into the mixed acid. The present author have ever

experienced the formation of amorphous silica small particles during dissolution of iron (a few mass % silicon) into the mixed acid. A small quantity of silicic acid ($Si(OH)_4$) would be formed from a reaction between silicon and the mixed acid during the dissolution process of the sample and the silicic acid would transform into the amorphous silica particles through gelation and drying.

In addition, the electrolytic copper (99.9 mass % Cu, 0.0017 mass % O, 0.0104 mass% Si) used in the present experiment might contain amorphous silica inclusion. Therefore, following preliminary experiments were performed in order to distinguish the amorphous silica inclusion formed in the copper sample from the amorphous silica particle formed during acid-dissolution process and the silica inclusion contained in the electrolytic copper.

(1) Commercially available silicon standard solution for atomic absorption analysis (1mg Si /ml, KOH solution of K_2SiO_3) of 1 ml was filtered.

(2) The silicon standard solution of 1 ml was added to the mixed acid (10 ml HCl +10 ml H_2O + 2 ml HNO_3), heated and filtered.

(3) The electrolytic copper of 1 g was heated in the mixed acid and dissolved into the acid and filtered.

(4) The electrolytic copper of 1 g and the standard silicon solution of 1 ml were heated in the mixed acid, dissolved and filtered.

The filter used in the experiments from (1) to (4) was the polycarbonate filter with 0.1 μm pore diameter. The deposit on the filter was observed by TEM.

B. Experimental Procedure of Silicon-Deoxidation

Details on experimental apparatus (furnace and twin rollers etc.) were the same as that described in the previous report[7] and in Chapter 3 and 5. A copper specimen, in which copper oxide (Cu_2O) was buried, was charged in a crucible made of transparent silica (13 x 10 x 500 mm or 13 x 10 x 1000 mm)

and maintained at 1423K in the furnace. After melting, a small amount of silicon buried in a copper chip was added. The amount of the copper oxide and silicon was the quantity to change the copper composition to about 500 mass ppm O and 500 mass ppm Si, when both of them were dissolved in the copper matrix (about 6g). The copper sample was maintained at 1423K for 60 minutes in order to dissolve the whole silicon into it. Two methods for cooling and solidifying the sample (ultra rapid cooling and quenching into water[7]) were adopted. The shorter crucible (13 x 10 x 500 mm) had an aperture (1 mm diameter) in the bottom and was used in the experiment for ultra-rapid cooling of the sample. The sample was dripped by increasing argon pressure through the bottom aperture onto twin rollers rotating at high speed (3100 rpm), between which the sample was sandwiched and pressed to solidify instantly (ultra rapid cooling).[7] The sample in the longer crucible (13 x 10 x 1000 mm) with no aperture was lowered for the bottom of the crucible to be quenched into water in a vessel equipped under the furnace, in which water was introduced just before the quenching (quenching into water).[7] The cooling rate that could be achieved with the ultra-rapid cooling method is probably about 10^5 K/s and the rate by the water quenching method is less than it.[7]

From the sample quenched into water, the top and bottom parts, and peripheral part that had been in contact with the crucible wall, were cut off in order to remove primary deoxidation product, which have floated up to the upper part of the sample or adhered to the wall. The remained copper specimen was used for TEM observation. The oxygen content of the sample quenched into water was determined by inert-gas fusion-infrared absorptionmetry (LECO,TC136), although oxygen analysis of the sample cooled ultra-rapidly could not be performed because of thin small ribbon-like shape of the sample.

C. Preparation of Specimen for TEM

Filter Replica Method[7] was used for preparation of specimen for TEM observation. For the TEM specimen of the Preliminary Experiment (1), the polycarbonate filter was soaked in hydrochloric acid before filtration, because, without this process, the filter covered with carbon film often shrank immediately after soaking into chloroform.

III. Experimental Results and Discussion

A. TEM Observation*

Amoeba -like particles of amorphous silica was observed on all the filters used in Preliminary Experiments from (1) to (4). However, there were fewer particles in Preliminary Experiments (1) and (3) than the particles in Experiments (2) and (4). In Preliminary Experiments (1), the mixed acid was not added to the standard silicon solution. In Preliminary Experiment (3), the silicon amount in the electrolytic copper is less than that in the standard solution of 1 ml. Thus, the fewer particles were formed in Preliminary Experiments (1) and (3). Consequently, it is clear that the mixed acid reacts with a small amount of silicon in copper or in the standard silicon solution to form amoeba -like particles of amorphous silica. Figures 7.1-(a), 7.1-(b), and 7.1-(d) show the TEM images of the amoeba -like particles of amorphous silica observed on the filters. In Fig. 7.1-(d), which shows an amoeba-like particle of amorphous silica in the Preliminary Experiment (4), square-shaped inclusions containing

---

* In the TEM photograph from Fig. 7.1-(a) to Fig. 7.3-(b), the dark grey and black parts show the amorphous silica on the light grey carbon film. The carbon film often has creases, rents and holes as shown in Figs. 7.1-(a), (b), (c), and 7.2-(c). The holes originate in pores of polycarbonate filter.

aluminum buried in the amorphous silica were observed. During dissolution process into the acid, the square-shaped inclusions having been contained in the electrolytic copper would be surrounded by a gel of silicic acid formed by the reaction between silicon and the mixed acid, and the gel would be transformed into the amorphous silica by drying. An amoeba -like particle in Fig. 7.1-(b) in preliminary experiment (3), is a little different from the other in Figs. 7.1-(a), 7.1-(c) and 7.1-(d). It seems amoeba-like but also seems an agglomeration of small particles of amorphous silica. It would be an agglomeration of small amorphous silica formed by the reaction between the mixed acid and silicon in the electrolytic copper, or might be composed of small amorphous silica inclusions in the electrolytic copper bound together during dissolution.

In the copper sample deoxidized with silicon and quenched into water, three types of amorphous silica inclusions were observed; the pinecone-like inclusion (Figs. 7.2-(a), 7.2-(b)), gourd-shaped inclusion (Fig. 7.2-(b)) and network-like inclusion (Fig. 7.2-(c)). Amoeba-like particles of amorphous silica except a particle of amorphous silica similar to that in Fig.7.1-(c) were not found in the sample quenched into water.

In the sample deoxidized with silicon and cooled ultra-rapidly, the fine spherical inclusion and coral-like inclusion (Figs.7.3-(a), 7.3-(b)) were observed. The coral-like inclusion would be a fragment of the net-work-like inclusion. Fine amoeba-like particles of amorphous silica were also observed in the sample cooled ultra-rapidly, although the particles were smaller than those observed in the samples of the preliminary experiments shown in Fig. 7.1. In contrast, as was stated above, few amoeba-like particles of amorphous silica were found in the sample quenched into water. The results would show that the fine amoeba-like particle of amorphous silica observed in the copper cooled

ultra-rapidly would be formed by a reaction between the mixed acid and very fine amorphous silica inclusions in copper. The very fine amorphous silica inclusion would form silicic acid through the reaction with the acid, and subsequently agglomerate to form an fine amoeba-like particle of amorphous silica. However, a small number of amoeba-like particles of amorphous silica might form by the reaction between silicon in the copper and the mixed acid. Practically, it is impossible to distinguish the origin of the fine amoeba-like amorphous silica. Therefore, at the present stage, the fine amoeba-like amorphous silica should be counted out of the inclusion in the copper sample.

Spherical inclusion was not observed in the sample quenched into water. Spherical inclusions firstly formed in the sample would have time to coalesce and, due to viscosity of liquid silica at lower temperatures, they would form the pinecone-like or gourd-shaped inclusion. Spherical inclusions formed at the last stage of solidification would be pressed by the advanced copper solidification front and gathered at the grain boundary of the copper where they were pressed and solidified into a network-like inclusion connected each other.[7]

The electron diffraction pattern of the amorphous silica inclusion show halo pattern as shown in Fig. 7.3-(c).

B. Primary and Secondary Inclusion

In the sample cooled ultra-rapidly, inclusion with larger size than the fine inclusions shown in Fig. 7.3 was not found. Primary silica inclusion formed at 1423K from the deoxidation reaction would float up to the upper part of the sample and subsequently connect each other to become larger cluster of silica. Further, heterogeneous nucleation would occur on the wall of the crucible to grow to primary silica inclusion and, thus, some inclusions in the midst of flotation would be caught by the inclusion grown on the wall. The large cluster

and the inclusion grown on the wall could not passe the hole of the crucible. Therefore, the sample cooled ultra-rapidly did not include the large primary inclusions. Primary inclusion in the sample quenched into water should be eliminated because the upper and peripheral parts of the sample were cut off after deoxidation experiment.

The trunk thickness of the network-like inclusion observed in the sample quenched into water are 100-200 nm and that of the coral-like inclusion in the sample cooled ultra-rapidly are 20-40 nm. Therefore, the size of the network-like (coral-like) silica decreased with increasing of the cooling speed. This fact proves that the network-like (coral-like) inclusion should be secondary. On the other hand, the pinecone-like (Figs. 7.2-(a), 7.2-(b)) and gourd-shaped inclusions (Fig. 7.2-(b)) were not observed in the sample cooled ultra-rapidly, which indicates that there was no sufficient time in the sample to grow to the pinecone-like and gourd-shaped inclusions. This result also proves the inclusions to be secondary If they were primary, they should be observed in the sample cooled ultra-rapidly because the sizes were so small to be able to pass the hole of the crucible. Although primary inclusion was not investigated in the present study, the investigation for comparing the primary and secondary inclusions would be necessary in future in order to confirm the formation mechanism of amorphous silica.

C. Suspension of Fine Primary Silica

The observed inclusions except the amoeba-like inclusion were recognized as secondary inclusions. However, it has been reported that the suspension of fine primary alumina which could not float upward would be present in aluminum-deoxidized iron with excess oxygen beyond the equilibrium value.[21-23] Also in the silicon-deoxidized copper, there might have been such fine suspension of

silica. The fine suspension of silica , if any, might firstly form as liquid silica because of high supersaturation degree of the copper, and the primary liquid silica would immediately transform into amorphous silica. Thus, in the sample cooled ultra-rapidly, there might be the amorphous silica which had been suspended in the liquid copper. However, in the sample quenched into water, the liquid silica formed during cooling would have caught the suspended silica, and through repeated collision and coalescence, it would have grown to the pinecone-like or gourd-shaped inclusion. The proportion of the suspended silica in the pinecone-like or gourd-shaped inclusion could not be known. However, by TEM observation, the pinecone-like or gourd-shaped inclusions were seemed as homogeneous, which indicates that the inclusions were mainly consisted of liquid silica formed during cooling, and finally transformed into amorphous, although the fine suspension of amorphous silica might be buried in the inclusions. Therefore, in the present stage, it would be adequate to classify the inclusions as secondary.

D. Consideration based on Ostwald's Step Rule[8,12]

In Fig. 7.4, the two standard chemical potential differences between quarts and cristobalite ($\mu^{\circ}_{quar.}$-$\mu^{\circ}_{cri.}$), and between liquid silica and cristobalite ($\mu^{\circ}_{liq.}$-$\mu^{\circ}_{cri.}$), are shown. The standard chemical potential of cristobalite is shown by a horizontal line of zero in Fig. 7.4. Cristobalite is the stable silica crystal from 1079K to the melting temperature (1996K).[9] At the equilibrium state between liquid copper and cristobalite, the $\mu^{\circ}_{cri.}$ is expressed by Eq. [7.1].

$$\mu^{\circ}_{cri.} = \mu^{\circ}_{Si} + RT\ln a^{e}_{Si} + 2(\mu^{\circ}_{O} + RT\ln a^{e}_{O}) \qquad [7.1]$$

where, μ°_{Si} and μ°_{O} are the standard chemical potential of silicon and oxygen in liquid copper, respectively, and a^{e}_{Si} and a^{e}_{O} are the activity of the silicon and oxygen in the equilibrium state, respectively. The $\mu^{s.s.}$, which is the following

sum of the chemical potential values of silicon and oxygen in the supersaturated state ($\mu_{Si}^{s.s.}$ and $\mu_{O}^{s.s.}$), is expressed by both the degree of supersaturation (S) and the chemical potential of cristobalite ($\mu_{cri.}^{\circ}$).

$$\mu^{s.s.} = \mu_{Si}^{s.s.} + 2\mu_{O}^{s.s.} = \mu_{Si}^{\circ} + RT\ln a_{Si}^{s.s.} + 2(\mu_{O}^{\circ} + RT\ln a_{O}^{s.s.}). \quad [7.2]$$

$$\therefore \mu^{s.s.} = \mu_{cri}^{\circ} + RT\ln S, \quad [7.3]$$

$$S = \{a_{Si}^{s.s.} \cdot (a_{O}^{s.s.})^2\}/\{a_{Si}^{e} \cdot (a_{O}^{e})^2\}, \quad [7.4]$$

where $a_{Si}^{s.s.} \cdot (a_{O}^{s.s.})^2$ and $a_{Si}^{e} \cdot (a_{O}^{e})^2$ are the activity products of silicon and oxygen in the supersaturated state, and in the equilibrium state, respectively. Therefore, the difference of chemical potential, $\mu^{s.s.} - \mu_{cri}^{\circ}$, equals $RT\ln S$. According to Ostwald's Step Rule,[8,12] a supercooled liquid material, which shows polymorphism, solidifies first as an unstable (metastable) crystal and then gradually transforms into another polymorph with lower chemical potential in a step by step manner. Further, Ostwald pointed out that the supersaturated state creates unstable or metastable states. Therefore, the Step Rule could be applied for the supersaturated state. At 1873K, 1 kJ of $\mu^{s.s.} - \mu_{cri}^{\circ}$ corresponds to 1.07 in S value. Although the S value is small, the corresponding $\mu^{s.s.}$ value is higher than the chemical potential of liquid silica. Therefore, a little increase of supersaturation degree during cooling of iron would produce liquid silica which solidifies as amorphous. The amorphous silica observed in aluminum-deoxidized iron would be formed by this process. At 1423K, 3 kJ of $\mu^{s.s.} - \mu_{cri}^{\circ}$ corresponds to 1.29 in S. Thus, in the copper, amorphous silica could be formed from the supersaturated state at 1423K or from the supersaturated state achieved during cooling.

In the present experiment, the silicon-deoxidized liquid copper maintained at 1423K for 1 hour would have been in a supersaturated state. Hendry and Belov reported that the copper sample in the equilibrium state with silicon from 16 to

121 ppm, have shown a few mass ppm oxygen.[18] The oxygen content in copper quenched into water in the present study was 230 mass ppm Therefore, the silicon-deoxidized liquid copper maintained at 1423K for 1 hour should have been in a supersaturated state. The degree of supersaturation would increase during cooling furthermore than the level at 1423K. Therefore, liquid silica would be formed from the supersaturated state and solidified into amorphous silica. However the silicon content was not analyzed in the present study. Thus, evaluation of the degree of supersaturation for the copper of 230 mass ppm O for various silicon content might be helpful for deeper discussion.

E. Evaluation of Degree of Supersaturation

From JANAF Thermochemical Tables[9], the standard Gibbs free energy of formation of cristobalite can be obtained as follows.

$$\mathrm{Si\ (l) + O_2 \rightarrow SiO_2\ (cri.)}, \quad \Delta G^\circ = -909.0 + 0.175T \ \text{(kJ/mol)}. \qquad [7.5]$$

The standard Gibbs free energy of oxygen dissolution into liquid copper was calculated from the data by Otsuka et al,[13]

$$1/2\mathrm{O_2} \rightarrow \underline{\mathrm{O}}\ [\text{mass \%}], \quad \Delta G^\circ = -75.5 + 0.0113T \ \text{(kJ/mol)}. \qquad [7.6]$$

The silicon activity coefficient at infinite dilution (r°) was derived as 0.0014 (at 1423K) by the calculation based on an ideal associated solution model,[14,15] using the activity data by Bergman et al. at 1753K[16] and the heat of mixing data by Batalin at 1783K[17]. Thus,

$$\mathrm{Si\ (l)} \rightarrow \underline{\mathrm{Si}}\ [\text{mass \%}], \quad \Delta G^\circ = RT \ln r^\circ \frac{M_{\mathrm{Cu}}}{100 M_{\mathrm{Si}}} = -123 \ \text{(kJ/mol)}. \qquad [7.7]$$

From Eqs [7.5], [7.6], and [7.7],

$$\underline{\mathrm{Si}}\ [\text{mass \%}] + 2\underline{\mathrm{O}}\ [\text{mass \%}] \rightarrow \mathrm{SiO_2\ (cri.)}$$

$$\Delta G^\circ (\text{at } 1423\mathrm{K}) = -419 \ \text{(kJ/mol)}, \qquad [7.8]$$

$$a_{\mathrm{Si}}^e \cdot (a_{\mathrm{O}}^e)^2 = 4.3 \times 10^{-16}. \qquad [7.9]$$

For calculating the activity product ($a_{Si}^{s.s.} \cdot (a_O^{s.s.})^2$) in the supersaturated state, the interaction parameters (e_O^{Si}, e_{Si}^O) are required. Although no interaction parameter value at 1423K is found, a few data at higher temperatures are available,[18-20] which represent a good linear relationship between the reciprocal temperature (Fig. 7.5). Linear regression analysis represents e_O^{Si} as follows.

$$e_O^{Si} = -4.2 \cdot 10^5 / T + 218.5. \qquad [7.10]$$

From Eq. [7.10],

$$e_O^{Si} = -77, \quad e_{Si}^O = -135, \quad \text{at 1423K.} \qquad [7.11]$$

A roughly estimated silicon content in the sample quenched into water is around 260 mass ppm by the assumption that the amount of oxygen decrease from 500 to 230 mass ppm in the present study was consumed by the formation of primary deoxidation product of silica. Therefore, the estimated silicon content of 260 mass ppm, oxygen content of 230 mass ppm and interaction parameter values in Eq. [7.11] yield activity product ($a_{Si}^{s.s.} \cdot (a_O^{s.s.})^2$) as follows.

$$a_{Si}^{s.s.} \cdot (a_O^{s.s.})^2 = 1.1 \cdot 10^{-11}, \qquad [7.12]$$

where, e_{Si}^{Si} and e_O^O were neglected because of the limiting concentration region. From the value of Eq. [7.12], the degree of supersaturation of about 2500 was derived. In addition, the assumption for the silicon content of the sample to be 400, 300, 200, or 100 mass ppm, yields the activity product as $1.2 \cdot 10^{-13}$, $3.1 \cdot 10^{-12}$, $7.1 \cdot 10^{-11}$, or $1.2 \cdot 10^{-9}$, respectively. Therefore, even the smallest activity product at 400 mass ppm Si gives the supersaturation degree of 280, which proves that the chemical potential of the supersaturated state in the present experiment is considerably high.

The present author previously reported that the activities in low aluminum and high oxygen region of Fe-Al-O system could not be expressed by the

recommended values of interaction parameter which had been measured for the equilibrium state. The interaction parameters in Eq. [7.10] were derived based on the values in the equilibrium states. Thus, it is uncertain whether the interaction parameters in Eq. [7.11] is effective in the supersaturated state. However, there is no other method but to use the values in Eq. [7.11] for the estimation of activities in the present stage. Further investigation for the interaction parameters should be necessary for more precise evaluation of the degree of supersaturation.

IV. Conclusion

An experiment of silicon deoxidation of copper at 1423K was performed in order to investigate the mechanism of formation of amorphous silica inclusion in iron and copper.

(1) Preliminary experiments proved the formation of amoeba-like amorphous silica from a reaction between silicon and mixed acid (HCl: H_2O: HNO_3 = 10:10:2). The amoeba-like amorphous silica, which might be formed during the preparation process of TEM specimen, has to be counted out of silica inclusion in copper.

(2) In the copper deoxidized with silicon and quenched into water, three types of amorphous silica inclusions (pinecone-like inclusion, gourd-shaped inclusion and network-like inclusion) were observed.

(3) In the copper deoxidized with silicon and cooled ultra-rapidly, the fine spherical inclusion and coral-like inclusion were observed. The coral-like inclusion would be a fragment of network-like inclusion. The fine amoeba-like silica observed in the sample might have been formed by a reaction between very fine secondary inclusions of amorphous silica and the mixed acid.

(4) The pinecone-like, gourd-shaped and network-like inclusions observed in

the copper quenched into water, and the fine spherical and coral-like inclusions observed in the copper cooled ultra-rapidly, were classified as secondary inclusion.

(5) From the standpoint of Ostwald's Step Rule, possible liquid silica formation from copper even in a small degree of supersaturation was shown. The liquid silica inclusion formed from the supersaturated state during cooling should solidify into the inclusions of amorphous silica.

(6) Amorphous silica observed in iron should be formed in similar mechanism as that in the copper

(7) The evaluated degree of supersaturation for the copper quenched into water indicates the high degree of supersaturated state of the copper, although further investigation for interaction parameters used in the evaluation is necessary.

References

1. K.Wasai and K.Mukai: The Final Report of Ultra Clean Steel Research Group, Progress in Research on Ultra Clean Steel -Fundamental and Applied Aspects- (1999), 3, No.9511, ISIJ. Japan.
2. N.Iwamoto: Tetsu-to-Hagane, **58**(1972), 787.
3. F.Honda and K.Hirokawa: Tetsu-to-Hagane, **60**(1974), 2013.
4. S.Watanabe, K.Takano, K.Moriya, Y.Tu and Y.Shiroishi: Tetsu-to-Hagane, **65**(1979), 383.
5. A.Adachi, N.Iwamoto and Y.Ueda: Tetsu-to-Hagane, **51**(1965), 1617.
6. M.Okubo, Y.Miyashita and R.Imai: Tetsu-to-Hagane, **54**(1968), S59.
7. K.Wasai and K.Mukai : ISIJ International, **42**(2002), 459.

8). K.Wasai and K.Mukai : ISIJ International, **42**(2002), 467.

9. JANAF Thermochemical Tables, Second Edn, ed.by D.R.Stull and H.Prophet, Horikoshi Laboratory,Tokyo (1975), 1049.

10. A.Makisima : Kinzoku, **66**(1996), 196.

11. Iwanami's Dictionary of Physics and Chemistry, 5th Edn, CD-ROM,ed by S.Nagakura et al., Iwanami Shoten,Tokyo (1999).

12. W.Ostwald:Z.Phys.Chem., **22**(1897), 289.

13. S.Otsuka and Z.Kozuka : Metall. Trans., **12B**(1981), C32.

14. K.Wasai and K.Mukai : J.Japan Inst.Metals, **45**(1981), 593.

15. K.Wasai and K.Mukai : J.Japan Inst.Metals, **46**(1982), 266.

16. C.Bergman, R.Chastel and J.-C.Mathieu : J.Chem Thermodynamics, **18**(1986), 835.

17. G.I.Batalin and V.S. Sudavtsova : Izv. Akad. Nauk. SSSR. Neorg Mat., **18**(1982), 155.

18. Alan Hendry and H.B.Bell : Trans. Instn. Min. Metall., **83**(1974), C10.

19. I. M. Koval'skii, I.F.Khudyakov and E.I.Eliseev : Izvest. vyssh. Ucheb. Zaved.,Tsvetn Metall., (1985), No.4, 29.

20. V. S. Sudavtsova, G.I.Batalin and V. M. Ilyushhenko : Russian J. Phys. Chem., **59**(1985), No.6, 876.

21. K. Wasai and K.Mukai: Metall and Mater. Trans. B, **30B**(1999), 1065.

22. O.Repetylo, M.Olette and P.Kozakevitch: J Metals, **19**(1967), 45.

23. L.E.Rohde, A.Choudhury and M.Wahlster: Arch Eisenhüttenwes., **42**(1971), 165.

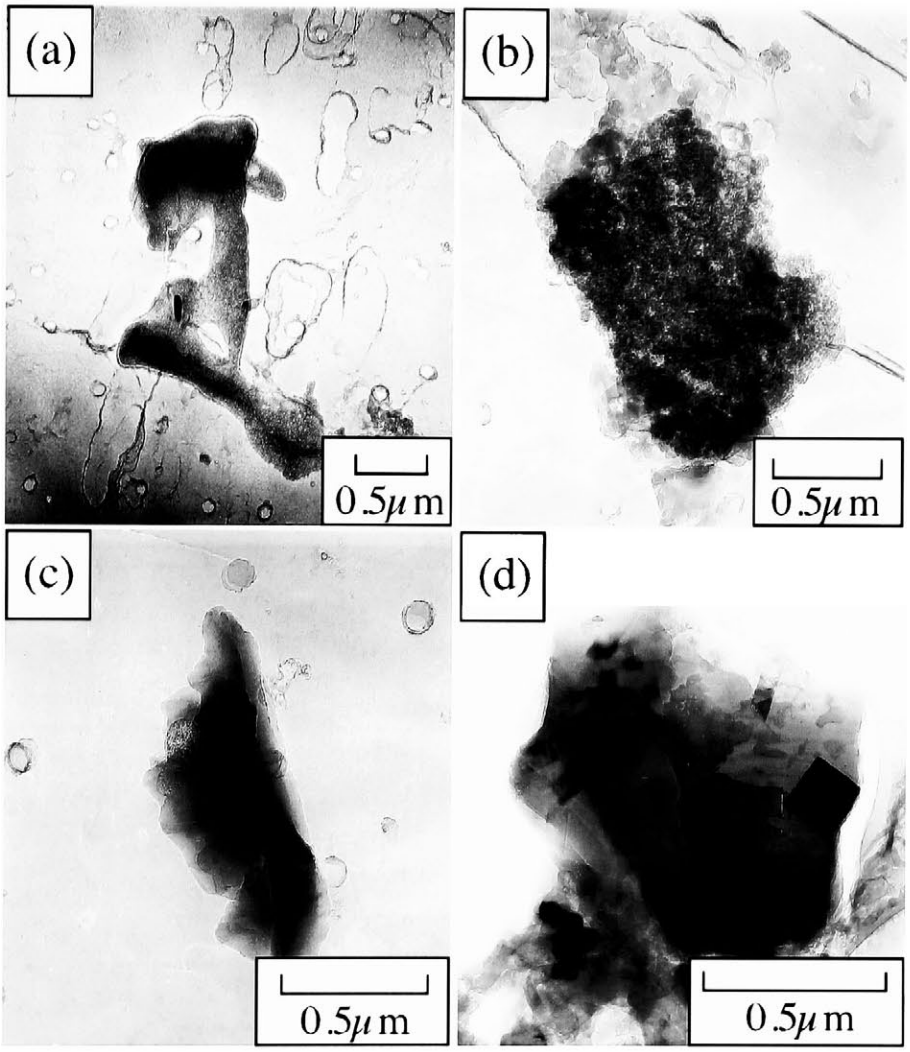

Fig. 7.1 Amorphous silicas observed in the samples of preliminary experiments from (1) to (4). (a),(b),(c) and (d); preliminary experiment (1), (2), (3) and (4), respectively.

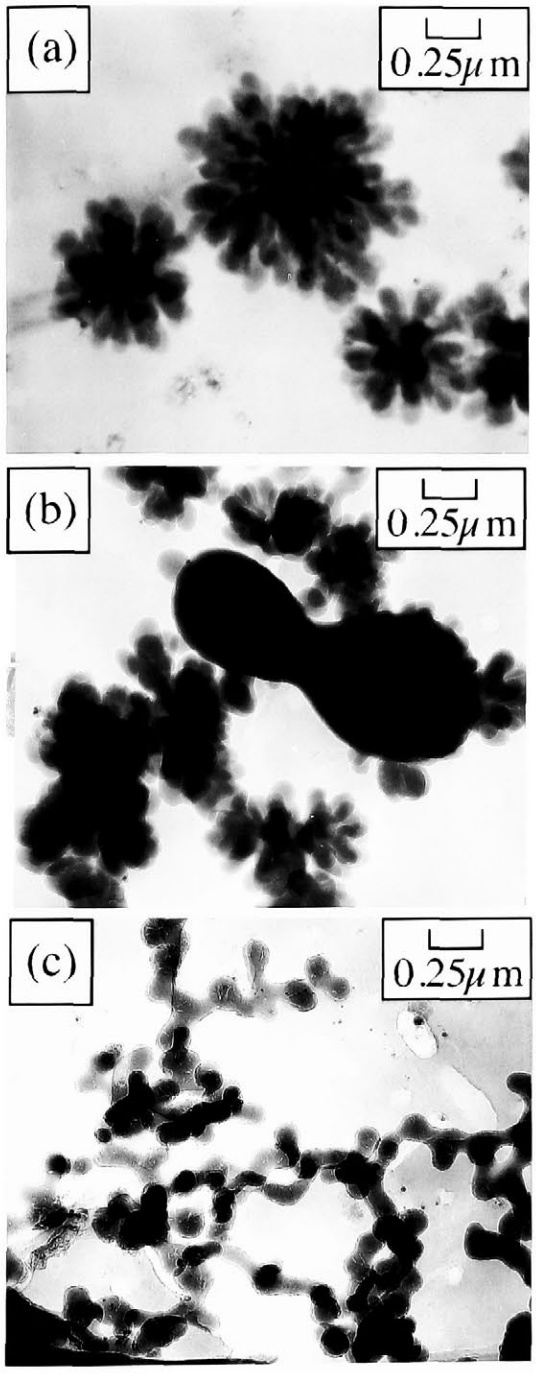

Fig. 7.2 Amorphous silica inclusions in copper deoxidized with silicon and quenched into water.
(a); Pinecone-like inclusions.
(b); Pinecone-like and gourd-shaped inclusions.
(c); Network-like inclusion.

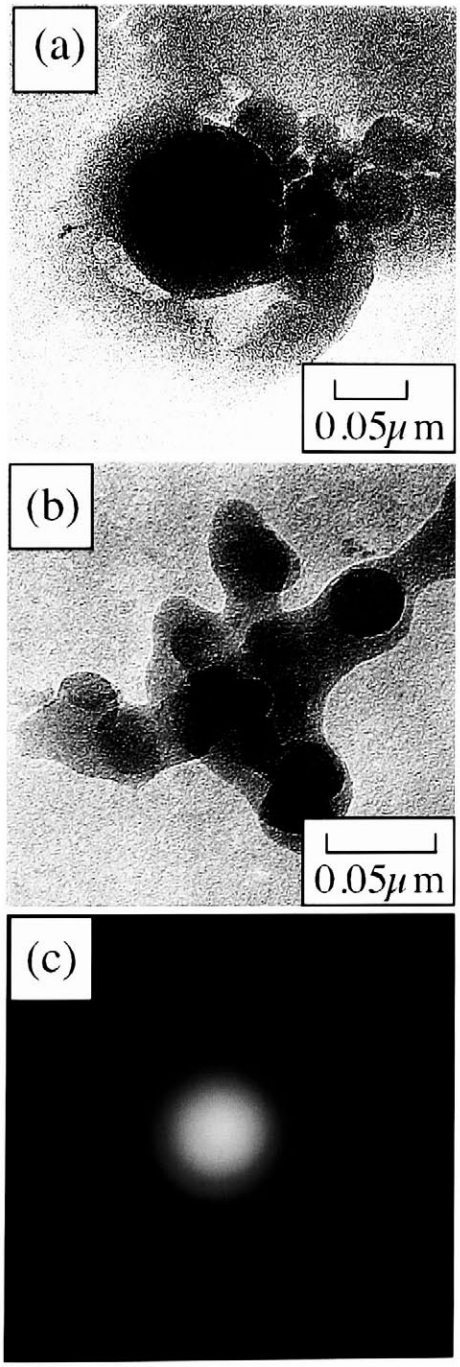

Fig. 7.3

(a), (b); Spherical and coral-like inclusions of amorphous silica in copper deoxidized with silicon and cooled ultra-rapidly, respectively.

(c); Electric diffraction pattern of an amorphous silica inclusion.

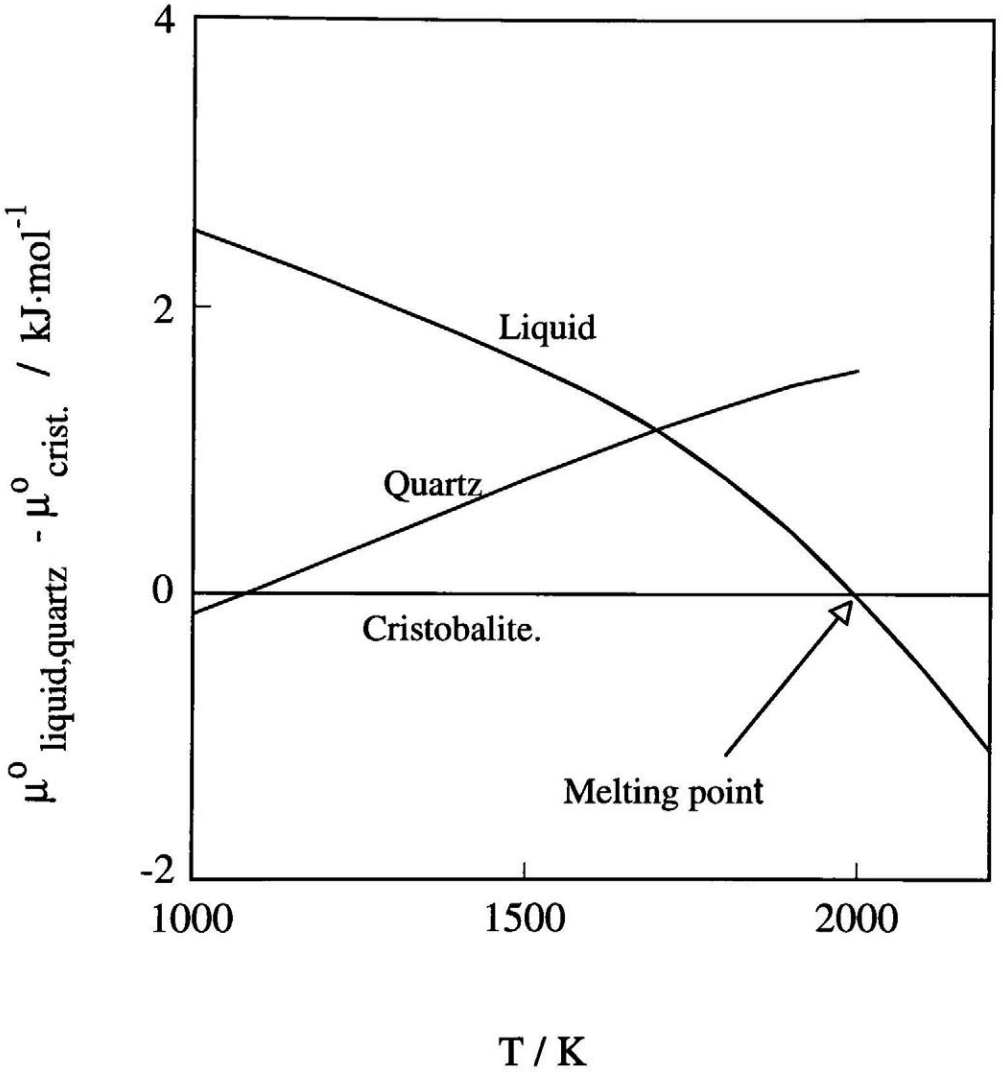

Fig. 7.4 Chemical potential differencies between unstable silicas (quarts and supercooled liquid silica) and cristobalite.

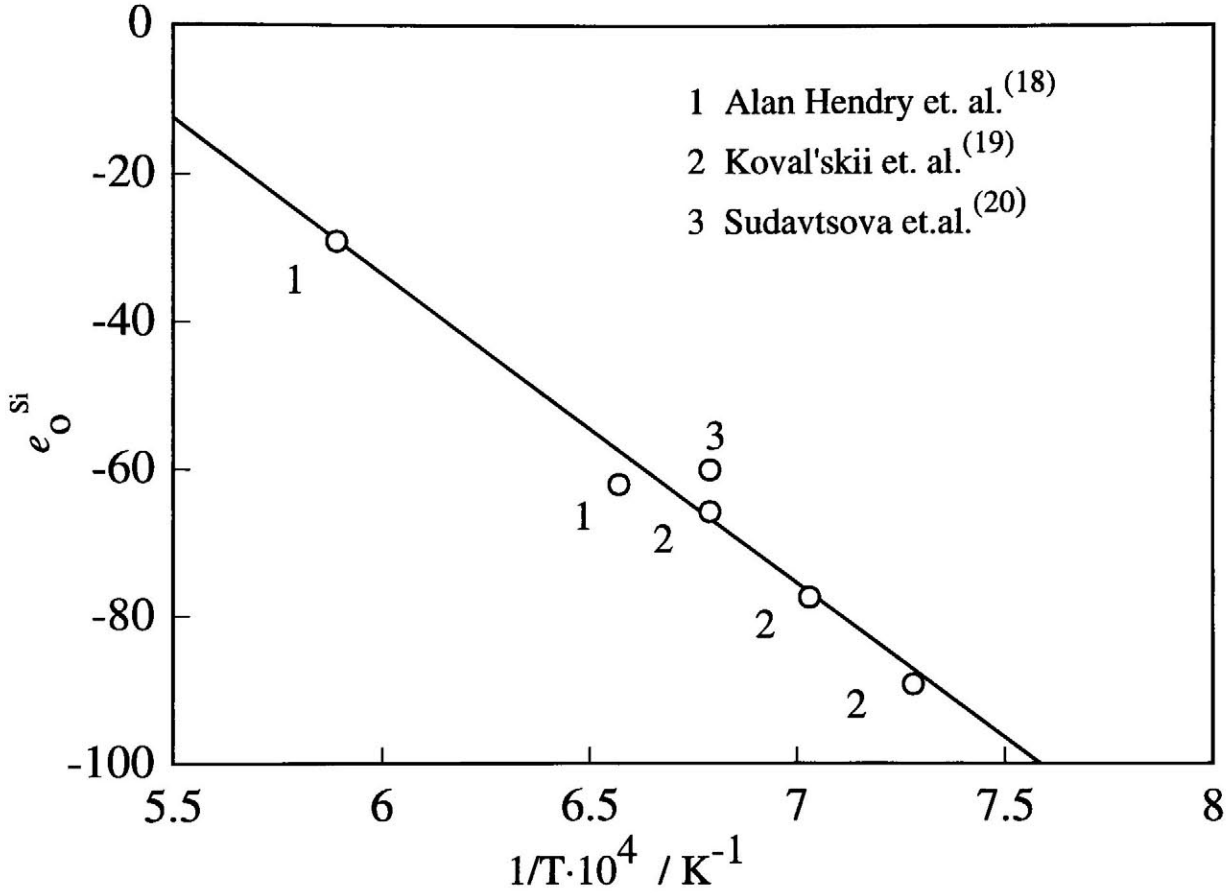

Fig. 7.5 Interaction parameter e_O^{Si} reported by Alan Hendry et. al. (18), Koval'skii et. al.(19) and Sudavtsova et.al.(20)

Chapter 8 Summary

I. Introduction

The study in previous chapters, the present author believe, should develop the better understanding for thermodynamics of Al-deoxidized liquid iron, although many problems remain in this system. In order to clarify the present situation and for the purpose of solving the remained problems, abbreviation for the characteristic feature of the thermodynamics of Al-deoxidized iron obtained in the present study should be shown.

The present study is divided into two parts, one is a part including Chapter 2 and 3 and dealing with liquid iron in equilibrium with α-alumina (the equilibrium state), and another part includes Chapter 4, 5, 6, and 7 dealing with the liquid iron containing excess oxygen beyond the equilibrium value. The characteristic points in each part are summarized in this chapter.

II Characteristic Points from the Present Investigation

A. Liquid Iron in the Equilibrium State

Various discrepancies of the thermodynamic measurements for liquid iron in the equilibrium state have been reported. The present investigation on the basis of an associated solution model revealed that the discrepancies in the system was caused by the misunderstanding of the liquid iron in the equilibrium state as a dilute solution in which the activities could be described fully by interaction parameters, although the misunderstanding was attributable not only to the insufficient knowledge for the dilute solution of the liquid iron system but also to the difficulty and insufficient accuracy of the measurement.

The equilibrium curve (E.C.), which shows a relation between aluminum and oxygen contents in the liquid iron in the equilibrium state, has been believed as a

linear line in low aluminum region because the interaction coefficients give an almost straight line. However, the present study proved it to be a curve which have a minimum in aluminum content in low aluminum region. The misunderstanding of the curve as a linear line is a main cause of the discrepancies of the deoxidation constant and the location of coexisting point, which is the equilibrium point of the three phases, liquid iron, α-alumina and hercynite. The curve also indicates that the interaction coefficients measured by various investigators are inappropriate to be applied to the low aluminum region of the liquid iron, furthermore, the interaction coefficients themselves have been derived from inappropriate methods due to the lack of information about the thermodynamics for such system that the interactions between constituent elements were very large.

There was another misunderstanding that the oxygen and aluminum in the liquid iron should transform into alumina during solidification. From the consideration on the basis of the associated solution model, it was shown that associated oxides should solidify into solid oxides which were not only alumina but also wüstite and so on.

The discrepancies caused by the misunderstanding and misinterpretation of the experimental data could be revised by using the associated solution model. Further, experimentally determined location of the coexisting point was agreed with that estimated by the model. These results revealed that the thermodynamic properties of the Fe-Al-O system in equilibrium state could be properly described by the model.

B. Liquid Iron Containing Excess Oxygen beyond the Equilibrium Value

Excess oxygen in liquid iron beyond the equilibrium value was mainly due to the supersaturated alumina associated compounds and suspended alumina particles, which was derived from computer simulations on the basis of

homogeneous nucleation theory. The homogeneous nucleation theory considered the Gibbs free-energy change of parent liquid iron and the dependence of the interfacial free energy between liquid iron and α-alumina. In the simulation, the associated solution model was also used. The simulation well explained the deoxidation process observed experimentally. A mechanism of formation of unstable and liquid alumina and liquid silica in the liquid iron as secondary inclusion were also proposed in the simulation. The formation of amorphous silica in copper during cooling from 1423K, which was observed experimentally, would be the supporting evidence of the formation of secondary liquid alumina and silica in iron.

III. Conclusion

In all the articles mentioned in this thesis, the mysterious feature of the Al-deoxidized steel was pared off and essential feature of the system was appeared. This system is characteristic for the strong interaction between aluminum and oxygen, thus, the interaction parameters measured by various investigators would not be appropriate for describing the thermodynamic properties of this system not only in the supersaturated state but also in the equilibrium state. Instead of the parameters, associated solution model is effective for such systems that the interactions between constituent elements are strong. Furthermore, this system often shows excess oxygen which transforms into various unstable alumina during solidification. The appearance of the excess oxygen are due to the Gibbs free-energy barrier occurred during nucleation before reaching the equilibrium state. The barrier comes from the Gibbs free-energy increase of parent liquid iron alloy during nucleation which is substantially caused by the strong interaction between aluminum and oxygen.

The excess oxygen might also transforms into liquid alumina inclusions

during solidification. The liquid alumina should act as a binder of fine aluminas to make a large cluster. Therefore, in order to avoid the formation of the cluster, the formation of liquid alumina should be inhibited.

Acknowledgment

I express appreciation to Professor K.Mukai for his enlightening discussions and suggestions throughout the course of my research.

I also express appreciation to Professor M.Hasebe, Professor H.Kage, Professor H.Nakamura, and Professor S. Seetharaman for their helpful advice and discussion.

I am grateful to Professor H. Era for his advice and instruction on the analysis of electron diffraction patterns, to Professor N. Shinozaki for his helpful advice and encouragement, and to Professor K.C.Mills who kindly amended my English expression . I am grateful also to Dr. W. Lin for his experimental assistance and discussion, to Mr. E. Ishida for his advice on computer usage, to Ms. R. Umegane for their assistance on chemical analysis, and to Mr. A.Miyanaga, Mr. A.Yoshida, Mr. H. Fuchiwaki, Mr. I. tougo and Mr. T. Shiraishi for their experimental assistance while undergraduate and graduated students at Kyushu Institute of Technology, to Mr. N. Wakayama, Mr. K. Shiraishi and Mr. K.Yamamoto for TEM, EPMA, SEM and X-ray analysis.